UNIVERSITÀ DEGLI STUDI DI PADOVA

Department of Physics and Astronomy Galileo Galilei

PH.D. COURSE IN ASTRONOMY
SERIES XXXVI

THE IMPACT OF PULSATION-DRIVEN MASS LOSS AND ROTATION ON THE EVOLUTION OF PRIMORDIAL VERY MASSIVE STARS

Ph.D. School Coordinator:	Prof. Giovanni Carraro
Supervisor:	Prof.ssa Paola Marigo
Co-supervisor:	Dr. Guglielmo Costa
Co-supervisor:	Dr. Léo Girardi
Co-supervisor:	Prof. Alessandro Bressan
External reviewer:	Prof. Norbert Langer
External reviewer:	Dr. Marco Limongi

Ph.D. student: Guglielmo Volpato

Abstract

My Thesis focuses on the evolution and final fates of primordial very massive stars. I begin with an introduction to the stellar structure equations and the methods used in the PAdova and tRieste Stellar Evolution Code (PARSEC). Then, I concentrate on pulsations in massive and very massive stars, and the resulting pulsation-driven mass loss. To achieve this, I implement the recipe for pulsation-driven mass loss developed by Nakauchi et al. (2020) in the PARSEC code. Using these models, I study the evolution and final fates of primordial very massive stars with initial masses from $100\,M_\odot$ to $1000\,M_\odot$ for two values of the initial metallicity $Z = 0$ and $Z = 0.0002$. These models form black holes within a very broad mass range: from $\sim 40\,M_\odot$ to $\sim 1000\,M_\odot$. On top of this, the $100\,M_\odot$ zero-metallicity models could form black holes consistent with the primary black hole of the GW190521 merger event.

Then, I investigate the effect of rotation on the evolution of very massive stars, particularly how it affects their final fates. To this end, I present the main implementation of stellar rotation in the PARSEC code and study the possible jet-driven events powered by an accretion disk within the collapsar scenario by Woosley (1993). This scenario demands a central black hole formed from the collapse of the star, enough angular momentum to sustain a disk, and the lack of an extended envelope for the jet propagation through the stellar progenitor. I recompute the models with initial masses $100 - 150 - 200\,M_\odot$ with 4 different initial rotational velocities (20%, 30%, 40%, and 50% of the critical value). The models that undergo pulsational-pair instability supernovæ produce successful gamma-ray bursts, while those that collapse directly to a black hole are progenitors of jet-driven supernova events. Due to these jet-driven supernovæ, several models are expected to produce black holes within the pair-instability black-hole mass gap. Furthermore, the predicted successful gamma-ray burst events could be observable with the Swift-BAT X-ray detector up to redshift ~ 20, while the corresponding afterglows are within the capabilities of the JWST.

To facilitate the computation of stellar isochrones from all these tracks, I developed a Python script that finds the so-called critical points along stellar evolution tracks. These critical points are then crucial for the computation of stellar isochrones. The critical points code, along with the algorithm for calculating stellar isochrones, is thoroughly described in the appendixes at the end of this Thesis.

List of Publications

In this Thesis, I present the results achieved during my PhD. What follows is a list of papers published in refereed journals.

- **G. Volpato**, P. Marigo, G. Costa, A. Bressan, M. Trabucchi, L. A. Girardi, F. Addari (2024), "A Study on Primordial Very Massive Star Evolution II: Stellar Rotation and Gamma-Ray Burst Progenitor", In ApJ 961 89. DOI: 10.3847/1538-4357/ad1185.
- **G. Volpato**, P. Marigo, G. Costa, A. Bressan, M. Trabucchi, L. A. Girardi, (2023), "A Study on Primordial Very Massive Star Evolution", In ApJ 944 40. DOI: 10.3847/1538-4357/acac91.

Here, instead, follows a list of work not included in this Thesis.

- F. Addari, P.Marigo, A. Bressan, G. Costa, K. G. Shepherd, **G. Volpato** (2023) "The Impact of the Third Dredge-up and Mass Loss in Shaping the Initial-Final Mass Relation of White Dwarfs". Accepted in ApJ. DOI: 10.48550/arXiv.2401.09812
- E. Zackrisson, A. Hultquist, A. Kordt, J. M. Diego, A. Nabizadeh, A. Vikaeus, A. K. Meena, A. Zitrin, **G. Volpato**, B. Welch, G. Costa, R. A. Windhorst (2024) "Detecting and characterizing highly magnified Population III stars with JWST". Submitted to MNRAS. DOI: 10.48550/arXiv.2312.09289
- C. T. Nguyen, G. Costa, L. Girardi, **G. Volpato**, A. Bressan, Y. Chen, P. Marigo, X. Fu, P. Goudfrooij (2022) "PARSEC V2.0: Stellar tracks and isochrones of low- and intermediate-mass stars with rotation", In A&A 665, A126. DOI: 10.1051/0004-6361/202244166

Acknowledgments

First of all, I thank my supervisor Prof. Paola Marigo, who helped and walked me in my journey from the bachelor course in stellar evolution, through the master thesis, to the PhD, and beyond.

I thank all my co-supervisors Dr. Guglielmo Costa, Dr. Léo Girardi, and Prof. Alessandro Bressan for all the help, guidance, and discussions during these years.

I thank the members of the Padova and Trieste stellar astrophysics research group Francesco, Michele, Alessandro, Giada, Thahn, and Kendall for the great moments we had together.

I thank my doctoral colleagues and friends Nina, Amelia, Emanuele, Edoardo, Francesco, and all the others. You helped a lot in these years.

Thank you to my teammates and the staff of all the teams I played for in these twenty-plus years of football. You made the sport I love even more great.

A big thanks to my historic friends Hs Zanna, Jn Alberto, Tc Ricky, and Lieber Paolo. There are no other words to say: just thank you guys for everything!

An astronomical thank you to my family: my mom Monica, my dad Paolo, and my sister Ludovica. You gave me everything I ever wanted, my journey and my successes would not have been possible without you!

And now, the most important person in my little, crazy universe. Thanks to my girlfriend Francesca: you are my emission nebula, my Sun, my Big Bang!

If there were any other thanks to give, if there were... All I have left to say is that it has been quite a run, and then about all the opportunities the future holds: "What do you do, you deprive yourself?"[1]

[1] This is a more international version of my sardinian friend Francesco's motto: "Che fai?! Te ne privi?!"

Contents

List of Figures

List of Tables

List of Abbreviations

BH	black hole
cCB	carbon-oxygen
CCSN	core collapse Supernova
cHeB	core helium burning
CNO	carbon-nitrogen-oxygen
CO	carbon-oxygen
DBH	direct collapse to a black hole
DUP	dredge up
env	envelope
es	electron scattering
fCCSN	failed core-collapse Supernova
GRB	Gamma-Ray Burst
H-R	Hertzsprung-Russel
HRD	Hertzsprung-Russel diagram
JWST	James Webb Space Telescope
LSO	Last Stable Orbit
mlt	mixing-length theory
MS	main sequence
ov	overshooting
p-p	proton-proton
pdw	pulsation-driven winds
PI	pair instability
PISN	pair instability Supernova
PPI	pulsational-pair instability
PPISN	pulsational-pair instability Supernova
rad	radiation
rdw	radiation-driven winds
RSG	red supergiant
SN	Supernova
super-AGB	super-Asymptotic Giant Branch
VMS	very massive stars
WR	Wolf-Rayet
WRm	Wolf-Rayet manqué
ZAMS	zero-age main-sequence

To My Family

§Chapter 1

Introduction

Нельзя понять все сразу,
нельзя сразу начать с совершенства!
Чтобы достичь совершенства,
нужно начать с невежества во многом.
И если мы понимаем вещи слишком
быстро, возможно, мы не поймем их полностью.
Ф.М. Достоевский[1]

1.1 Star classification

Historically, the evolution of stars is classified according to their initial mass. There are three main classes of stars: low-mass stars, intermediate-mass stars, and massive stars.

Low-mass stars are characterized by the formation of a degenerate helium core post-main sequence (MS), resulting in an extended red giant branch phase. The ignition of helium is marked by an unstable event known as a helium flash. This phenomenon occurs within a mass range of approximately $0.8\,M_\odot$ to around $2\,M_\odot$[2] (the upper limit is often denoted as M_{HeF}).

Intermediate-mass stars follow a distinct evolutionary path where their helium core, unlike low-mass stars, remains non-degenerate. Helium ignition in these stars occurs in a stable manner. Following the central helium-burning phase, they develop a carbon-oxygen core that eventually becomes degenerate. Intermediate-mass stars fall within

[1] Идиот, part IV chapter VII
[2] all mass limits here depend on metallicity

the mass range of approximately M_{HeF} to M_{up}, around $8\,M_\odot$. Towards the end of their evolution, both low-mass and intermediate-mass stars shed their envelopes through a robust stellar wind, and their remnants manifest as carbon-oxygen (CO) white dwarfs.

Massive stars, possessing masses greater than approximately $8\,M_\odot$ ($M_{up} \approx 8\,M_\odot$), undergo carbon ignition within a non-degenerate core. Except for a limited mass range, approximately 8 to 11 $M_\odot$, which undergo the transition into the super-Asymptotic Giant Branch (super-AGB) phase, these stars also initiate fusion reactions for heavier elements within the core. This process continues until a core of iron (Fe) is formed, potentially leading to a collapse and resulting in a supernova explosion.

The primary focus of the present investigation lies in very massive stars (VMS) with initial masses exceeding $100\,M_\odot$. When these stars manage to avoid significant mass loss, their life cycles culminate in pair-instability explosions. Similar to other massive stars, these very massive stars undergo successive stages of hydrostatic burning for hydrogen, helium, carbon, and neon. Following the depletion of carbon in the core and a brief phase of neon burning, these stars experience a thermonuclear explosion triggered by the dynamical instability induced by the generation of electron-positron pairs in their oxygen cores.

Due to their very high initial masses, VMS are thought to be preponderant in the early Universe, when the initial mass function could have been shifted towards higher initial masses compared to nowadays.

1.2 Primordial Very Massive Stars

For the first generations of stars (Population III), the efficiency of cooling processes that regulate star formation is considerably diminished due to the absence or severe deficit of metals. In the early universe, magnetic fields and turbulence might also be less significant (Abel et al. 2002). As a consequence, for primordial stars in their unique conditions, the minimum mass for fragmentation (the local Jeans mass) may have been as high as $\simeq 1000\,M_\odot$ (e.g., Larson 1998; Hosokawa et al. 2011; Hirano et al. 2014; Stacy et al. 2016). From numerical simulations of star formation I expect that such stars form at redshift $z \simeq 20$ and have initial mass functions that either peak at $\simeq 100\,M_\odot$ (Bromm et al. 1999; Abel et al. 2002), or present a bimodal distribution with a second peak at a few $M_\odot$ (Nakamura and Umemura 2001). Other studies, in contrast, claim that the characteristic mass of Population III initial mass function could be significantly lower than the canonical $100\,M_\odot$ (Clark et al. 2011). For instance, in Figure 1.1 we can see the Hertzsprung-Russell diagram (HRD) evolution of intermediate, massive, and very massive Population III stars. These models are characterized by a pristine composition of hydrogen and helium, as these were the two most common elements formed during Big Bang nucleosynthesis.

Extremely metal-poor or zero-metallicity VMS, with initial mass in the range $100 \lesssim M_i/M_\odot \lesssim 1000$, have a broad astrophysical impact. Understanding how these population III stars evolve and die has implications for several key questions, including the observable characteristics of integrated stellar populations in low-metallicity galaxies; the nature of energetic transients, such as pair-instability supernovæ, super-luminous supernovæ, kilonovæ and gamma-ray bursts (Kozyreva et al. 2017); the source of extreme ionizing UV-radiation fields at high redshift (Dijkstra and Wyithe 2007); the agents of the earliest

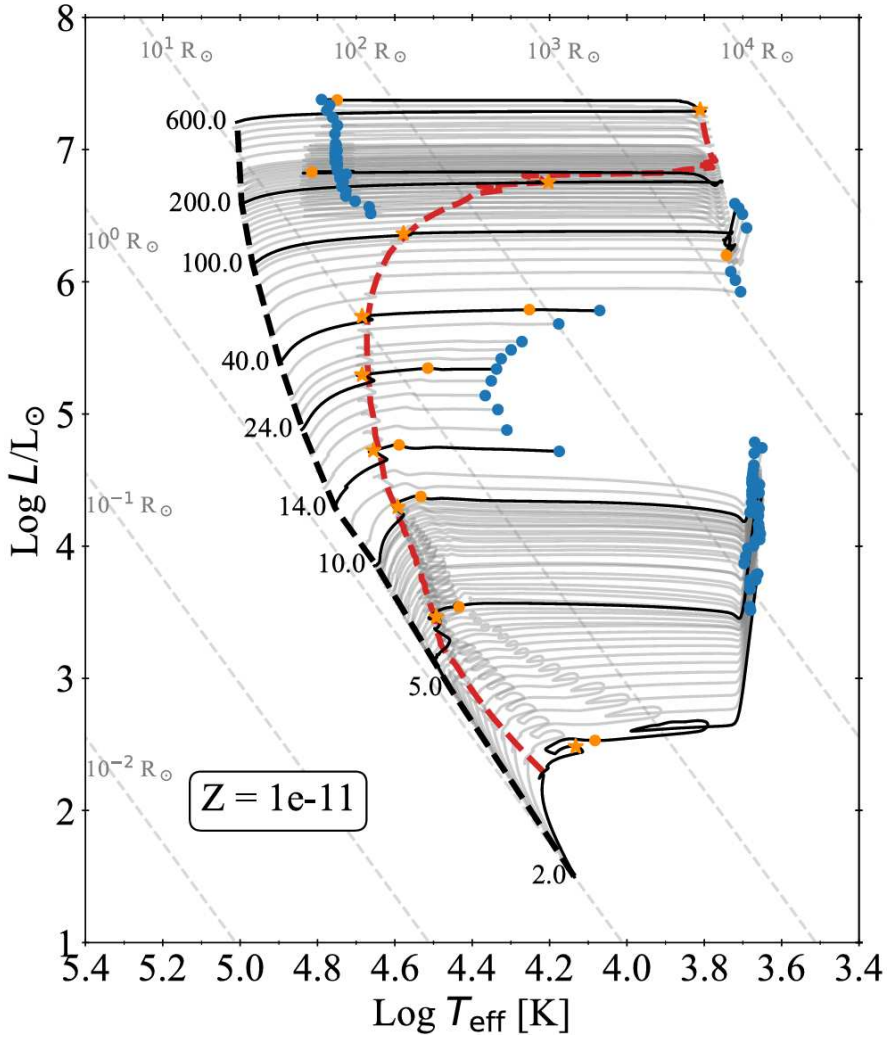

Figure 1.1: Hertzsprung-Russell diagram of Population III stars. All tracks are shown in solid gray lines, except those with initial mass M_i = 2, 5, 10, 14, 24, 40, 100, 200, and 600 $M_\odot$ in black. The black dashed line shows the zero-age MS, while the red dashed one indicates the end of the MS phase. Orange stars (circles) mark the ignition (end) of the central helium-burning phase. The blue circles show the final position of the models. Dashed lines of constant radii in units of $R_\odot$ are in grey. Figure from Costa et al. (2023b).

and fastest chemical enrichment of their host galaxies (Kozyreva et al. 2014; Goswami et al. 2021, 2022); the rates of gravitational-wave emission from merging black holes (BHs Abbott et al. 2016; Spera et al. 2019); the formation of primordial stellar BHs that could provide the seeds for the assembly of supermassive black holes of mass $\simeq 10^6 - 10^9\,M_\odot$ at redshift $z > 6$ via runaway stellar collisions in dense clusters (Belkus et al. 2007; Sakurai et al. 2017; Onoue et al. 2019; Nakauchi et al. 2020).

VMS ($100 \lesssim M_i/M_\odot \lesssim 300$) may undergo electron-positron pair creation instabilities (PI) before and during core oxygen burning, with a final outcome determined primarily by the mass of the helium core, M_{He}, eventually leading to a successful or failed core-collapse

supernova (fCCSN) or thermonuclear explosion (Heger and Woosley 2002; Kozyreva et al. 2017; Woosley 2017; Leung et al. 2019).

Stars with final helium core masses in the approximate range $34 - 45 \lesssim M_{He}/M_{\odot} \lesssim 64$ are predicted to join the domain of pulsational pair-instability supernovæ (PPISN). During these unstable stages, several strong pulses may eject a significant fraction of the star's residual envelope and possibly a small fraction of the core mass, before dying with a successful or failed core-collapse supernova (CCSN, Woosley et al. 2002; Chen et al. 2014; Yoshida et al. 2016; Woosley 2017; Farmer et al. 2019; Woosley and Heger 2021; Farag et al. 2022). Stars with larger helium core masses, $64 \lesssim M_{He}/M_{\odot} \lesssim 135$ are predicted to die as pair-instability supernovæ (PISN). Near the ignition of core oxygen burning such stars experience a single strong pulse followed by a thermonuclear explosion that unbinds the whole star, leaving no remnant (Fowler and Hoyle 1964; Barkat et al. 1967; Rakavy and Shaviv 1967; Fraley 1968; Heger and Woosley 2002; Heger et al. 2003; Takahashi et al. 2018; Takahashi 2018; Woosley and Heger 2021; Farag et al. 2022). In the past, PISNæ have been traditionally associated with the first, extremely metal-poor stellar populations (Ober et al. 1983; Bond et al. 1984; Glatzel et al. 1985; Heger and Woosley 2002), though recent stellar models suggest that PISNæ could happen for stars with initial metallicity up to $Z \simeq Z_{\odot}/3$ (Langer et al. 2007; Yusof et al. 2013; Kozyreva et al. 2014). The Tarantula Spectroscopic Survey (Crowther 2019; Schneider et al. 2018), which indicates that the current initial mass function is well populated up to $200\,M_{\odot}$ in the Large Magellanic Cloud, lends support to the existence of VMS at these metallicities.

Stars massive enough to form a helium core with $M_{He} \gtrsim 135\,M_{\odot}$ are predicted to undergo direct collapse to a BH (DBH). During the final stages, photodisintegration processes absorb the energy of the propagating shock, preventing the envelope from becoming unbound through mass ejection (Bond et al. 1984; Farmer et al. 2020). In these circumstances, only wind ejecta are produced (Fryer and Kalogera 2001; Heger and Woosley 2002; Nomoto et al. 2013). In this framework, I expect stars with $M_i \gtrsim 200 - 300\,M_{\odot}$ to avoid the thermonuclear explosion at very low metallicity (e.g., Goswami et al. 2021).

The details of this evolutionary picture, particularly the ranges of initial masses of stars that follow the same channel and achieve a similar final outcome, are affected by factors such as metallicity and the efficiency of stellar winds, among others (e.g., Vink et al. 2021). Indeed, mass loss is a critical process in the evolution of massive and VMS, though some aspects are still not completely understood. Mass loss contributes significantly to the chemical enrichment of the interstellar medium, can affect star formation by injecting momentum and kinetic energy into molecular clouds, and may have a decisive impact on the outcome of core collapse.

The winds of massive and very massive stars can be triggered and maintained by a variety of physical processes (Renzo et al. 2017). In hot and luminous stars, the radiation field transfers momentum to the out-flowing plasma via scattering in resonant spectral lines (e.g., Vink et al. 2001; Puls et al. 2008). Continuous absorption and scattering from dust grains act in the extended circumstellar envelopes of luminous red supergiants (RSGs), in which the interplay between pulsation and near-surface turbulent convection can also be important for mass loss (e.g., Bennett 2010; Höfner and Olofsson 2018; Kee et al. 2021). Luminous Blue Variables also involve pulsational mass loss, alongside eruptive phenomena (Baraffe et al. 2001; Puls et al. 2008; Smith and Arnett 2014; Nakauchi

et al. 2020), whereas mass loss is associated with Roche-lobe overflow and common-envelope evolutionary phases in interacting binary systems (e.g., Woosley et al. 1995; Wellstein and Langer 1999; Smith and Tombleson 2015; Shara et al. 2017).

The theory of line-driven winds applied to hot and luminous stars predicts a positive correlation between the mass-loss rate and the metal content (e.g., Vink et al. 2011), which implies that stellar winds in extremely metal-poor conditions should be quite weak (see, for instance, the Z = 0 models of Marigo et al. 2003). It is known that primordial main-sequence stars are pulsationally unstable above a critical mass of $\simeq 100\,M_{\odot}$ due to the destabilizing effect of nuclear reactions in their cores (Baraffe et al. 2001, ϵ-mechanism). The instability could reoccur during the core helium burning (cHeB) phase, excited by the κ-mechanism operating in the hydrogen ionization zone. Non-linear calculations show that such an instability causes mass loss rather than catastrophic disruption. Nakauchi et al. (2020) recently performed a new stability analysis of primordial VMS during the MS and cHeB stages, and provided analytic prescriptions for calculating the associated mass-loss rates.

Adopting the Nakauchi et al. (2020) results in combination with a well-tested scheme to account for radiation-driven winds, in this study I use the PARSEC code to follow the evolution of VMS at zero and extremely low metallicity, until the onset of dynamical instability caused by the creation of electron-positron pairs. I investigate the main evolutionary properties of these stars and predict their final outcome, which could be a massive BH or total incineration via a thermonuclear explosion.

1.3 Thesis outline

I organized this Thesis as follows.

In Chapter 2, I introduce the stellar structure equations, along with the methods adopted in the PAdova and tRieste Stellar Evolution Code (PARSEC). Chapter 3 focuses on massive star pulsations and the consequent pulsation-driven mass loss. Then, I present the implementation in the PARSEC code of the results by Nakauchi et al. (2020), which delves into the pulsations of VMS during both the MS and the red supergiant phases.

In Chapter 4, I use the PARSEC code to study the evolution of VMS. These stellar evolution models take into account not only radiation-driven winds and the Eddington factor effects but also mass loss due to stellar pulsations. In Chapter 5, I summarize the main aspects of stellar rotation and its implementation into the PARSEC code following Costa (2019); Costa et al. (2019a,b).

In Chapter 6, I present rotating stellar evolution models computed with the PARSEC code. Then, I mainly focus on the influence of stellar rotation on the final fates of VMS. In particular, the possible jet-driven events powered by an accretion disk formed around BHs originated from the collapse of these very massive progenitors. Finally, in Chapter 7, I conclude with the main results of this work and possible future perspectives.

§Chapter 2

Stellar Structure

In this Chapter, I present our stellar evolution code PARSEC (Bressan et al. 2012). In Section 2.1, I introduce the stellar structure equations. In Section 2.2, I explain how the equation of state and the opacity of the stellar matter are treated in PARSEC. In Section 2.3 there is an overview of the "standard" mass loss recipes adopted in our code. I describe the mixing-length theory and the corresponding overshooting, along with the schemes for chemical mixing and following the nuclear reactions during the evolution of stars in Section 2.4. Finally, in Section 2.5, I present the boundary conditions coupled with the structure equations.

2.1 Stellar structure equations

The first equation of stellar structure expresses the conservation of mass within a spherical shell of the star, given the assumption of spherical symmetry. The Lagrangian formulation is as follows:

$$\frac{\partial r}{\partial m} = \frac{1}{4\pi r^2 \rho}, \tag{2.1}$$

where the mass m is the spatial independent variable, r is the radius and ρ is the density of the shell.

Considering the conservation of momentum inside a star yields the second differential equation of stellar structure. We assume hydrostatic equilibrium, which means no net radial acceleration, and therefore the second equation reads:

$$\frac{\partial P}{\partial m} = -\frac{Gm}{4\pi r^4}, \tag{2.2}$$

with P the pressure.

The three major sources and sinks of energy within a stellar shell are the production of energy due to nuclear reactions, the removal of energy due to neutrino emission, and the heat flow expressed by the local luminosity l. This latter is related to the radial energy flux F according to $\mathrm{l} = 4\pi \mathrm{r}^2 \mathrm{F}$, where we assume spherical symmetry. Combining this with the first law of thermodynamics ($\partial \mathrm{u} = \partial \mathrm{q} + \frac{\mathrm{P}}{\rho^2}\partial\rho$) yields the third equation of stellar structure:

$$\frac{\partial l}{\partial m} = \epsilon_{nuc} - \epsilon_{\nu} + \epsilon_{gr}, \tag{2.3}$$

where the first term on the right-hand side is the nuclear energy generation rate, the second one is the neutrino energy rate, and the third is the gravitational energy rate. The latter is defined as $\epsilon_{\mathrm{gr}} = -\frac{\partial \mathrm{u}}{\partial \mathrm{t}} + \frac{\mathrm{P}}{\rho^2}\frac{\partial \rho}{\partial \mathrm{t}} = -\mathrm{T}\frac{\partial \mathrm{s}}{\partial \mathrm{t}}$, with s the specific entropy of the gas. Assuming thermal equilibrium (the energy generation in the star's center balances the radiative loss from the surface) implies that the star is in a stationary state and therefore $\epsilon_{\mathrm{gr}} = 0$.

The fourth equation of stellar structure concerns the transport of energy. It is given in terms of the temperature gradient required to transport energy in the two possible scenarios: radiative and convective. This equation reads:

$$\frac{\partial T}{\partial m} = -\frac{Gm}{4\pi r^4}\frac{T}{P}\nabla, \tag{2.4}$$

where ∇ can be either the radiative temperature gradient or the adiabatic temperature gradient plus the superadiabaticity $\Delta\nabla$. The former is defined as:

$$\nabla_{rad} = \frac{3\kappa}{16\pi acG}\frac{lP}{mT^4}, \tag{2.5}$$

with κ the Rosseland mean opacity (see Section 2.2), while the latter is:

$$\nabla_{ad} = \frac{P}{T\rho c_P}\Big(\frac{\partial ln\rho}{\partial lnT}\Big)_{P,\mu}. \tag{2.6}$$

The radiative gradient is adopted when $\nabla_{\mathrm{rad}} \leq \nabla_{\mathrm{ad}}$, while the adiabatic one when $\nabla_{\mathrm{rad}} > \nabla_{\mathrm{ad}}$. Then, the stability of the stellar layer against convection can be given by either the Ledoux criterion:

$$\nabla_{rad} \leq \nabla_{ad} - \frac{\chi_{\mu}}{\chi_T}\nabla_{\mu}, \tag{2.7}$$

where $\chi_{\mu} = \big(\frac{\partial \mathrm{logP}}{\partial \mathrm{log}\mu}\big)_{\rho,\mathrm{T}}$ and $\chi_{\mathrm{T}} = \big(\frac{\partial \mathrm{logP}}{\partial \mathrm{logT}}\big)_{\rho,\mu}$; or the Schwarzschild criterion:

$$\nabla_{rad} \leq \nabla_{ad}. \tag{2.8}$$

The nuclear reactions that provide energy to the star, also change its chemical composition throughout the different phases of stellar evolution. The change in mass fraction over time due to nuclear reactions reads:

$$\frac{dX_i}{dt} = \frac{A_i m_u}{\rho}\sum_k r_{ki} - \sum_j (1+\delta_{ij}) r_{ij}, \qquad i = 1 \ldots N, \tag{2.9}$$

where $\mathrm{X_i}$ is the mass fraction of the species i and in each shell holds $\sum_{\mathrm{i}} \mathrm{Xi} = 1$. $\mathrm{A_i}$ is the atomic mass, $\mathrm{m_u}$ is the atomic mass unit, $\mathrm{r_{ki}}$ is the rate of nuclear reactions that create the species i, while $\mathrm{r_{ij}}$ is the rate of those that destroy it. N is the number of species considered in the adopted nuclear network.

2.2 Equation of State and Opacity

The equation of state (EOS) relates thermodynamic quantities such as temperature T, density ρ, and pressure P with the chemical composition of stellar matter X_i; while stellar opacity, κ, is a function of ρ, T and X_i, which determines how much the radiation intensity is blocked by matter along its path from the core to the stellar surface.

These two ingredients are necessarily coupled (along with boundary conditions, Section 2.5) with the structure equations in Section 2.1, in order to close the system of partial differential equations and derive the stellar structure.

In PARSEC, the EOS is computed with the FREEEOS code by Irwin (2012)[1]. There are two different options: computing the EOS *on-the-fly* or using precomputed tables of the thermodynamic quantities. This latter is the standard option in PARSEC since the precomputed tables are sufficiently accurate for our purpose. Moreover, Bressan et al. (2012) compared the results obtained with the two options mentioned above, and demonstrated the negligible differences between the two. Elements from hydrogen to nickel are taken into account, along with several metallicity values for different heavy elements distributions. There are different EOS tables depending on the considered evolutionary phase. For hydrogen burning, the code adopts 10 "H-rich" tables, while for advanced burning phases, there are 31 "H-free" tables.

In principle, (radiative) opacity depends on the wavelength of the incoming radiation (along with the temperature and density of the stellar matter). For each process that contributes to stellar opacity, we can define a monochromatic opacity, κ_ν. The main processes to take into account are

- electron scattering: also known as Thomson scattering (in the non-relativistic limit). It is important at very high T, between $\sim 10^6$ K and $\sim 10^{8.7}$ K. In this process, radiation hits a free electron, which in turn re-emits radiation. The opacity does not depend on the frequency and is expressed as $\kappa_{\rm Th} = 0.2(1 + X)\,{\rm cm}^2/{\rm g}$ (assuming complete ionization);

- free-free absorption: it occurs when a free electron closely grazes an ion so that it can temporarily absorb radiation. The (classical Kramer) absorption coefficient is $\kappa_\nu \sim Z^2\rho T^{-1/2}\nu^{-3}$, with Z the ion charge. It is most important for ionized high-density matter, at $10^4\,{\rm K} \lesssim T \lesssim 10^6\,{\rm K}$;

- bound-free transition: also known as photoionization, it occurs when a photon has an energy higher than the ionization energy of a bound electron. The opacity in this case is given by $\kappa_\nu = a_\nu n_{\rm ion}/\rho$, where $n_{\rm ion}$ is the relative number of atoms in different ionization states and a_ν is the absorption coefficient of each ion. This process also includes the important absorption of the negative ion H^-, relevant for $10^{3.5}\,{\rm K} \lesssim T \lesssim 10^4\,{\rm K}$;

- bound-bound transition: in this process, the incoming radiation has enough energy only to promote a bound electron to a higher energy level inside the atom. The absorption coefficient reads $\kappa_\nu({\rm j}) = \sum_{\rm j} \sum_{\rm nn'} \kappa_{\nu,{\rm nn'}}({\rm j})$, where nn' indicates all possible transitions for each element j;

[1] available at http://freeeos.sourceforge.net

- molecular band transition: at $T \lesssim 10^4$, formation of molecules starts to occur. These latter impact the overall opacity of the stellar matter. In PARSEC, the opacity of molecular band transitions is taken into account adopting the results of the ÆSOPUS code (Marigo and Aringer 2009; Marigo et al. 2022).

Once all these physical processes are taken into account, usually a specific mean opacity is derived and then used in the structure equations. This mean is the Rosseland mean opacity, defined as

$$\frac{1}{\kappa} = \frac{\int_0^\infty \frac{1}{\kappa_\nu}\frac{\partial B_\nu}{\partial T} d\nu}{\int_0^\infty \frac{\partial B_\nu}{\partial T} d\nu}, \tag{2.10}$$

with B_ν the Planck function for radiation intensity. The Rosseland mean opacity is a harmonic average with the temperature derivative of B_ν as weighting. In this way, frequencies where the radiation flux is higher weight more in the Rosseland mean opacity.

The treatment of opacity in PARSEC is based on pre-computed tables of Rosseland mean opacities, $\kappa(\rho, T, X_i)$. Two different codes are used to compute these tables

- the Opacity Project At Livermore (OPAL) code (Iglesias and Rogers 1996), for $10^{4.2}\,K \leq T \leq 10^{8.7}\,K$;
- the ÆSOPUS code (Marigo and Aringer 2009; Marigo et al. 2022), for $10^{3.2}\,K \leq T \leq 10^{4.1}\,K$;
- a linear interpolation between the two codes is adopted in the region $10^4\,K \leq T \leq 10^{4.1}\,K$.

These opacity tables are loaded in PARSEC before the actual start of any stellar evolutionary calculation, and they are interpolated in temperature, density, and H-content. Different metallicity tables are used to bracket the possible variations in metal content during the evolution of the stellar model. Conductive opacities are also included according to Itoh et al. (2008).

2.3 Mass Loss

Here I briefly review the standard mass-loss prescription adopted in PARSEC to treat mass loss from single massive stars both in the hot and cool regions of the H-R diagram. Details can be found in Chen et al. (2015), and some recent revision is described in Costa et al. (2021). For simplicity, I refer to it as "radiation-driven winds" (rdw) recipe, though I acknowledge that in RSG, in addition to radiation on dust grains, other mechanisms may be at work, such as turbulence for example.

In short, I rely on four main formulations. For hot stars with $T_{\rm eff} > 10000$ K I adopt the formalism of Vink et al. (2000, 2001). I take into account the enhancement of the mass-loss rate when the Eddington factor, Γ_e, approaches unity (Gräfener and Hamann 2008; Vink et al. 2011). This parameter is commonly defined as

$$\Gamma_e = \frac{L\,\kappa_{es}}{4\pi\,G\,M}, \tag{2.11}$$

where M and L denote the current mass and luminosity, κ_{es} is the opacity due to electron scattering, and G is the gravitational constant. I use the same metallicity scaling relation as in Chen et al. (2015), which reads

$$\dot{M} \propto (Z/Z_{initial,\odot})^{\alpha}, \tag{2.12}$$

where $Z_{initial,\odot} = 0.01774$ is the initial solar metallicity (solar calibration in Bressan et al. 2012) and α is given by

$$\alpha = 2.45 - 2.4 \cdot \Gamma_e, \quad 0 \leq \alpha \leq 0.85\,. \tag{2.13}$$

For models having $X < 0.3$ at the surface and $\log(T_{eff}) > 4$, representative of Wolf-Rayet stars, I adopt the mass-loss prescription by Sander et al. (2019) with the metallicity dependence proposed by Costa et al. (2021), which is based on WN and WC star models at varying Fe, C, and O abundances computed by Vink (2015). Finally, for stars in the red supergiant phase ($T_{eff} < 10000$ K) I take the maximum between the mass-loss rates predicted by Vink et al. (2011, which accounts for the dependence on Γ_e) and de Jager et al. (1988).

2.4 Mixing, Overshooting, and Nuclear Reactions

In PARSEC is adopted the mixing-length theory (MLT Böhm-Vitense 1958), to describe convection. The average distance over which the convective eddies move is the mixing length, $l_{mlt} = \alpha_{mlt} H_P$, with H_P the pressure scale height and α_{mlt} the MLT parameter. This latter is set to $\alpha_{mlt} = 1.74$ throughout this Thesis, which is the value from the solar calibration performed in Bressan et al. (2012).

The code adopts the Schwarzschild criterion (Section 2.1) for the definition of convective regions (Schwarzschild 1958), but the convective eddies are able to overcome the border of these regions, requiring the adoption of an overshooting prescription (Bressan et al. 1981). For core overshooting, the ballistic implementation is followed (Maeder 1975; Bressan et al. 1981). The overshooting parameter ($\lambda_{ov} = 0.4$) times the pressure scale height is the mean free path of convective eddies *across* the border. For comparison with other prescriptions, the distance a bubble can travel into the stable region is $\sim 0.5\lambda_{ov} H_P$. On the other hand, for envelope overshooting, the prescription in Alongi et al. (1991); Bressan et al. (2012); Nguyen et al. (2022) is followed, with an average overshooting distance below the convective envelope of $\Lambda_{env} H_P = 0.7 H_P$.

In the current version of PARSEC, a diffusive scheme is adopted, where mixing and nuclear reactions are solved together. The mass fraction (X_i) variation of the element i due to both mixing and nuclear reactions is given by

$$\frac{\partial Y_i}{\partial t} = \frac{1}{\rho r}\frac{\partial}{\partial r}(r^2 \rho D \frac{\partial Y_i}{\partial r}) \pm \sum_j Y_j \lambda_k(j) \pm \sum_{j \geq k} Y_j Y_k [jk], \tag{2.14}$$

with $Y_i = X_i/A_i$, D the diffusion coefficient calculated within the MLT $D = 1/3 v l_{mlt}$. The second and third terms on the right-hand side show the single-body decay and the two-body reactions, respectively.

The nuclear reaction network consists of 33 isotopes, from hydrogen to zinc, and 72 reactions. The JINA REACLIB data (Cyburt et al. 2010a) is adopted for reaction rates and Q values.

2.5 Boundary Conditions

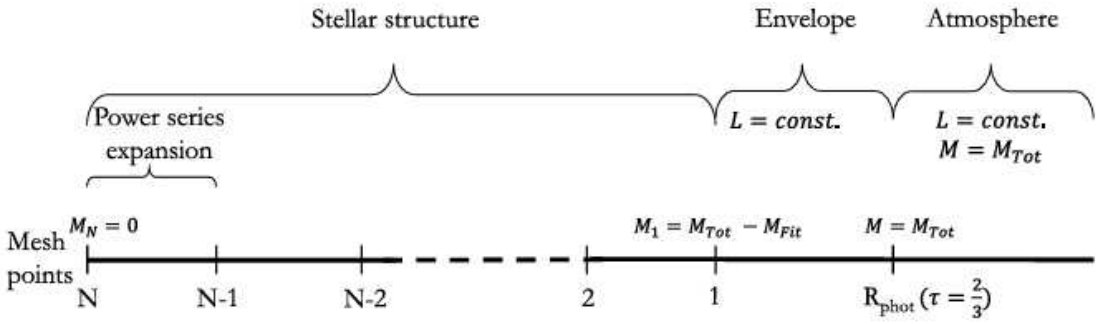

Figure 2.1: Three different regions in PARSEC model: internal structure, envelope, and atmosphere. Figure from Costa (2019).

Here, I describe the boundary conditions coupled to the structure and chemical composition equations that give the structure and evolution of the stellar model. There are two kinds of boundary conditions: at the stellar center and at the stellar surface.

Regarding the former, the code has to compute pressure and density at the center given that the radius and mass at that coordinate are zero. To this end, an approximation of the stellar structure equations (Section 2.1) for m $\rightarrow$ 0 is adopted. This reads as

$$r = \left(\frac{3m}{4\pi\rho_c}\right)^{\frac{1}{3}}, \tag{2.15}$$

$$P - P_c = -\frac{G}{2}\left(\frac{4\pi}{3}\right)^{\frac{1}{3}} \rho_c^{\frac{4}{3}} m^{\frac{2}{3}}, \tag{2.16}$$

$$L_c = \epsilon_c m, \tag{2.17}$$

$$T^4 - T_c^4 = -\frac{k\epsilon_c}{2ac}\left(\frac{3}{4\pi}\right)^{\frac{1}{3}} \rho_c^{\frac{4}{3}} m^{\frac{2}{3}} \qquad \text{(radiative)} \tag{2.18}$$

$$lnT - lnT_c = -\left(\frac{\pi}{6}\right)^{\frac{1}{3}} \frac{G}{P_c} \rho_c^{\frac{4}{3}} m^{\frac{2}{3}} \nabla_{ad} \quad \text{(convective)}, \tag{2.19}$$

with ϵ_c the energy rate at the center.

The outer region of the model is divided into two parts: the envelope and the atmosphere; whereas the internal structure extends from the center to the so-called fitting point (See Figure 2.1).

The atmosphere extends from the photosphere, where the optical depth is $\tau = 2/3$, to infinity. In this region, mass, radius, and luminosity are constant. Combining the definition of the optical depth and the hydrostatic equilibrium equation, the code obtains the following equation

$$\frac{d\tau}{dlogP} = \frac{\kappa P}{g} ln10. \tag{2.20}$$

On top of this, the modified Eddington approximation for the radiative transport is adopted as a temperature-optical depth relation

$$T^4(\tau) = \frac{3}{4} T_{\rm eff}^4 (\tau + q(\tau)), \tag{2.21}$$

where q(τ) the Hopf function. Equations 2.20 and 2.21 are integrated from infinity to the photosphere, yielding temperature and pressure a the stellar radius.

On the other hand, the envelope of the model stretches from the fitting point to the photosphere. The former is set at a very small fraction of the total mass of the star, i.e. ≤ 0.001. In this region, the luminosity of the model is kept constant, thus the three remaining physical quantities are derived as follows

$$\frac{\partial lnm}{\partial lnP} = -\frac{4\pi r^4 P}{Gm^2}, \tag{2.22}$$

$$\frac{\partial lnr}{\partial lnP} = -\frac{Pr}{G\rho m}, \tag{2.23}$$

$$\frac{\partial lnT}{\partial lnP} = min[\nabla_{rad}, \nabla_{ad}]. \tag{2.24}$$

§Chapter 3

Stellar pulsations and pulsation-driven mass loss

In this Chapter, I present stellar pulsations for massive and very massive stars, along with the subsequent pulsation-driven mass loss. In Section 3.1, I briefly introduce the study of stellar pulsations in this particular mass range, starting with some historical notes. In Section 3.2, I focus on the pulsation-driven mass loss for very massive stars with the implementation in the PARSEC code of the pulsation-driven mass loss recipe from Nakauchi et al. (2020).

3.1 Stellar Pulsations

Astronomers have been attracted by variable stars since the XVI century. The first periodic variable star to arouse attention was o Ceti, i.e. Mira; while δ Cephei, the foretype of Cepheid variables, was discovered in 1784 by Goodricke.

The first attempts to explain stellar variability from physical principles date back to the turn of the XIX century (Ritter 1879; Emden 1907). However, for many years, astronomers attributed the variability to binarity (Brunt 1913). On the other hand, the following year, Plummer (1914) proposed a not-better specified, radial pulsation mechanism as a possibility for explaining variable stars; while Shapley (1914) deeply criticized the binary explanation, but without mentioning the period-luminosity relation

recently formulated by Leavitt and Pickering (1912).

It was Eddington who realized that pulsating stars are thermodynamical engines. He also discussed the dissipation of pulsational energy, the phase lag problem (later tackled also by Rosseland 1950), and the modulation of heat to be a suitable explanation for pulsating stars (Eddington 1918, 1919, 1926, 1941). However, in his 1941 work, Eddington was still convinced that stellar pulsations were powered by the energy of nuclear reactions. He tried to solve the problem of the dissipation in the outer layers of the envelope, by suggesting that partial hydrogen ionization would diminish this effect and therefore nuclear reaction energy could overcome the envelope dissipation.

Before 1950, the *nuclear* driving mechanism was overestimated. The reason for this was that the central displacement amplitude was believed to be too large, compared to that at the surface. In turn, the central mass concentration of these giant stars (Cepheids) was not recognized. Epstein (1950), through recent stellar structure integrations, showed that the central density was between five to seven orders of magnitude higher than the average one. In this way, he perceived that the displacement in the central region due to pulsations was a factor $\sim 10^6$ lower than that at the surface. Within his work, he proved that the periods of pulsations were related to the envelope and that the central regions played a rather marginal role.

In the following years, Cox (1955, 1958) and Cox and Whitney (1958) narrowed down to the outer 15% of the stellar radius, the possible location of the driving mechanism of Cepheids. They found that the partial ionization of an element could be a source for the energy flux perturbations as the engine for pulsations in that kind of stars. Then, they recognized as the only possible driving source the He^+ partial ionization zone. However, in their studies, the work of Zhevakin was never mentioned. Adopting discrete models and non-adiabatic calculations, Zhevakin (1954) concluded that the He^+ ionization region plays a crucial role in driving pulsations in Cepheid stars.

Therefore, the driving mechanism for Cepheid-like stars is what is now called the $\kappa-\gamma$ mechanism (Catelan and Smith 2015). A star needs an energy reservoir to maintain pulsations. This energy is provided by reactions occurring during nuclear burning phases. The issue is then to find a suitable mechanism that converts this energy into mechanical work, which sets the stellar pulsations in motion. Crucially, this mechanism must provide heat to the stellar gas at high temperatures and subtract it at low temperatures, like a thermodynamic engine. We have to consider those layers inside a star, where there is a partial ionization of H or He. In those layers, the opacity (κ, thus the name of the mechanism) of the stellar matter increases during compression and decreases during expansion. Hence, these are driving layers for the instability of the stellar pulsations, which can thus grow and be maintained during a compression-expansion cycle. On top of this, partial ionization prevents part of the absorbed energy from increasing the local temperature of the gas, therefore enhancing the ability of those stellar layers to accumulate energy, which later will be used in the pulsating motion (see Catelan and Smith 2015, for a comprehensive and mathematical description of the $\kappa-\gamma$ mechanism).

On the other hand, the *nuclear* mechanism conceived by Eddington (1941) operates in different stars than Cepheids. Cowling (1935) assessed that the instability of the central burning regions to convection did not affect the stability of the star to pulsations. In his work, the role of radiation pressure was not recognized, but six years later Ledoux (1941) accounted for radiation pressure in both the stellar structure and the analysis of

pulsations. Ledoux derived an upper limit for the stellar mass, above which the star becomes pulsationally unstable (see also Schwarzschild 1958; Schwarzschild and Härm 1959). In his work, this limit corresponds to $100\,M_\odot$. This is due to the destabilizing effect of nuclear reactions in the central regions. These layers absorb energy during compression and release it during expansion, fulfilling the condition for instability (see Catelan and Smith 2015, for further details). This mechanism is now called $\epsilon-$mechanism. It is efficient only for very massive stars, because of the very high temperatures needed to overcome the damping of the envelope (Catelan and Smith 2015). For instance, more classical stellar pulsators like RR Lyrae stars can not provide large enough temperatures to maintain pulsations within this driving mechanism.

The upper limit mentioned above concerns stars of Population I composition (Schwarzschild and Härm 1959). In the following years, nonlinear calculations demonstrated that this pulsational instability could produce mass loss rather than the breakdown of the star (Appenzeller 1970; Talbot 1971a,b; Papaloizou 1973a,b). However, all these studies considered solar-like and slightly metal-poor stars (Schwarzschild and Härm 1959; Stothers and Simon 1968; Aizenman et al. 1975; Stothers 1992; Glatzel and Kiriakidis 1993; Kiriakidis et al. 1993), or Wolf-Rayet stars (Maeder 1985; Cox and Cahn 1988).

Since the temperature and structural differences between metal-rich and metal-poor stars, it was fundamental to tackle the pulsational stability problem also for stars devoid of metals. Different authors (Baraffe et al. 2001; Sonoi and Umeda 2012; Shiode et al. 2012; Inayoshi et al. 2013) performed linear stability analyses for zero-metallicity stars with initial masses between $100\,M_\odot$ and $3000\,M_\odot$ during the MS phase. They found that the mass loss rates were not high enough to affect the evolution of these stars ($\sim 10^{-6} < \dot{M}/M_\odot\,yr^{-1} < 10^{-4}$). Moreover, Baraffe et al. (2001) and Shiode et al. (2012) broadened their analysis to higher metallicities ($10^{-4} < Z/Z_\odot < 10^{-1}$) for stars of $\sim 100\,M_\odot$, discovering a positive correlation between mass loss and metallicity. On the other hand, Heger et al. (1997) and Moriya and Langer (2015) extended the previous analysis to red supergiants at solar and zero metallicity. They found an increment in the instability at increasing mass.

Finally, in a recent work, Nakauchi et al. (2020) studied the pulsational instability in very massive stars during both the MS and post-MS phases, deriving analytical expressions for the computation of pulsation-driven mass loss for very massive stars.

3.2 Pulsation-driven mass loss for VMS in PARSEC

I implemented this new pulsation-driven mass loss in the PARSEC code using the results of Nakauchi et al. (2020). I denote the corresponding rate as $\dot{M}_{pdw}$, where pdw stands for "pulsation-driven winds". The authors performed a pulsational analysis of very massive stars with initial mass $300 \leq M/M_\odot \leq 3000$ and metallicity between $Z = 0$ and $Z = 0.002$. They found their models to be unstable to radial pulsations during the early phases of the MS (ϵ-mechanism), as well as, when they move to the cooler part of the Hertzsprung-Russell (H-R) diagram, during cHeB (κ-mechanism). Assuming that all pulsational energy is transferred to the mass outflow, they derived an analytic prescription for pulsation-driven mass loss. Their recipe is a function of the initial metallicity of the star, its current mass, and its effective temperature. To compute the mass-loss rate

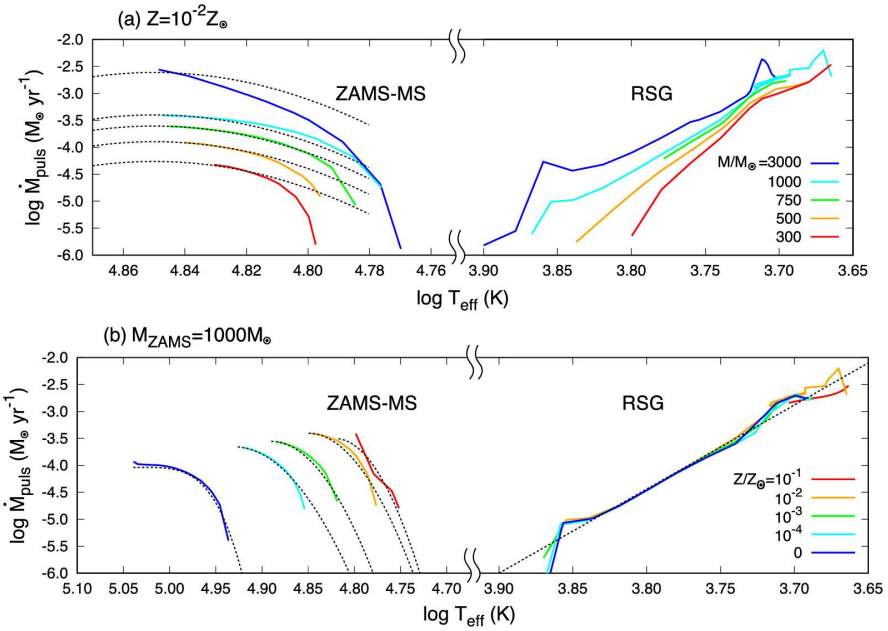

Figure 3.1: Pulsation-driven mass loss rates as a function of the effective temperature. *Panel a*: models with initial metallicity $Z_\odot = 0.0002$ and different initial masses. *Panel b*: models with initial mass $1000\,M_\odot$ and different initial metallicities. The dotted lines show the mass-loss rate fit from Equations 3.1 and 3.2. Figures adapted from Nakauchi et al. (2020).

they propose two different formulations, depending on whether the star is in the MS or RSG phase during cHeB. The two equations read as follows (Equations (17) and (18) in Nakauchi et al. 2020):

$$\log\left(\frac{\dot{M}_{\rm pdw}}{M_\odot\,{\rm yr}^{-1}}\right) = \alpha_1\,\log\left(\frac{M}{10^3\,M_\odot}\right) - \alpha_2 - \beta_1\,[\log(T_{\rm eff}) - \beta_2]^\gamma\,, \quad \text{MS} \qquad (3.1)$$

$$\log\left(\frac{\dot{M}_{\rm pdw}}{M_\odot\,{\rm yr}^{-1}}\right) = -2.88 + \log\left(\frac{M}{10^3\,M_\odot}\right) - 15.6\,[\log(T_{\rm eff}) - 3.7]\,, \quad \text{RSG} \qquad (3.2)$$

where α_1, α_2, β_1, β_2 and γ are coefficients that depend on the initial metallicity. Equation (3.1) is valid for $T_{\rm eff} > T_{\rm eff,min}$, a threshold also defined by the initial metallicity. Equation (3.2) applies for $\log(T_{\rm eff}) \leq 3.85$ (3.7) when $Z \lesssim 0.0002$ (0.002). All details can be found in Table 1 of Nakauchi et al. (2020).

In Figure 3.1, we can see the mass loss trend as a function of the effective temperature for Nakauchi's models with different initial masses and metallicities. We can also see the trend of the fit formulae from Equations (3.1) and (3.2). During the MS phase, mass loss increases as we move at higher stellar masses and metallicities. Instead, in the RSG phase it converges towards high values.

While Equation (3.2) refers, strictly speaking, only to the cHeB phase, it is reasonable to assume that it can also be used to describe later phases. In fact, it is well established that cool stars tend to become increasingly unstable to pulsation as their temperature decreases (Catelan and Smith 2015). Therefore, for simplicity, I adopt Equation (3.2)

for all post-MS stages during which the $T_{\rm eff}$ drops below the aforementioned threshold. Because of the short duration of such phases, this assumption is expected to have a negligible impact on my results.

The results of Nakauchi et al. (2020) imply that, during the MS, the mass-loss rate increases with metallicity at a given mass. I account for this by interpolating Equation (3.1) in log(Z).

The stability analysis of Nakauchi et al. (2020) is strictly valid for $300 \leq M_i/M_\odot \leq 3000$, whereas I applied their mass-loss prescriptions down to $M_i = 100\,M_\odot$. To validate my extrapolation I examined the results of a few studies on pulsational mass loss in the $100 \lesssim M_i/M_\odot \lesssim 500$ range.

To describe the transfer of energy from pulsation to mass loss, Nakauchi et al. (2020) used the same approach of Baraffe et al. (2001), who investigated the stability of metal-free zero-age main-sequence (ZAMS) models with $120 \leq M/M_\odot \leq 500$. I find that the mass-loss rates predicted by the former author are well compatible with the results presented in Table 3 of the latter authors for $M \geq 300 M_\odot$. At smaller masses, Equation (17) of Nakauchi et al. (2020) tends to overestimate the mass-loss rate when compared with Baraffe et al. (2001), but predictions from both studies are of the same order of magnitude. This is not expected to change the fate of the lower-mass tracks in my sets, but my $M_i = 100\,M_\odot$ model may result in a slightly larger final mass.

For the post-MS regime, I compared it with the work by Moriya and Langer (2015), who explored the $150 \leq M_i/M_\odot \leq 250$ mass interval. Their work is also inspired by the method of Baraffe et al. (2001), but focuses on pulsation-induced mass-loss after the MS. They provide analytic expressions for the mass-loss rates as a function of effective temperature and of the efficiency ε with which pulsational energy is converted into kinetic energy of the out-flowing matter. I considered the results for their largest conversion efficiency ($\varepsilon = 0.8$), as Nakauchi et al. (2020) effectively assume $\varepsilon = 1$, and compared the two studies in the regime explored by Moriya and Langer (2015), that is for $T_{\rm eff}$ approximately between 4600 and 5000 K. Over that interval of temperature Nakauchi et al. (2020) find pulsational instability as well, and mass-loss rates predicted by both works are comparable. In particular, the mass-loss rates of Nakauchi et al. (2020) are a factor 3-5 larger than the predictions of Moriya and Langer (2015) at $T_{\rm eff} \simeq 5000$ K, but they are smaller by nearly the same factor at $T_{\rm eff} \simeq 4600$ K, suggesting that the cumulative mass-loss is of the same order of magnitude.

Yadav et al. (2018) confirm the instability found by Moriya and Langer (2015), but identify an additional regime of pulsational mass loss at higher temperatures ($\log(T_{\rm eff}) \simeq 4.2 - 4.4$), that they attribute to strange mode instability. The latter leads to mass-loss rates of order $10^{-7} - 10^{-4}\,M_\odot {\rm yr}^{-1}$, increasing with mass, that are not predicted by Equation (18) of Nakauchi et al. (2020). It is therefore possible that my smaller-mass evolutionary tracks neglect the occurrence of mass loss during early cHeB stages, while little can be said concerning the higher masses as the study of Yadav et al. (2018) is limited to $M \leq 250\,M_\odot$. However, it is reasonable to expect that strange mode instability would not cause a cumulative mass loss so large to impact my results, as it would affect relatively rapid evolutionary stages.

§Chapter 4

Very Massive Star Evolution

This chapter is based on:
G. Volpato, P. Marigo, G. Costa, A. Bressan, M. Trabucchi, and L. Girardi;
"A Study of Primordial Very Massive Star Evolution";
ApJ, 944(1):40; Feb. 2023; doi: 10.3847/1538-4357/acac91.

In this Chapter, I present new evolutionary models of primordial very massive stars, with initial masses ranging from 100 $M_\odot$ to 1000 $M_\odot$. These models extend from the MS until the onset of dynamical instability caused by the creation of electron-positron pairs during core C, Ne, or O burning, depending on the star's mass and metallicity. Mass loss accounts for radiation-driven winds as well as pulsation-driven mass loss on the MS and during the red supergiant phase. After examining the evolutionary properties, I focus on the final outcome of the models and associated compact remnants.

This Chapter is organized as follows. In Section 4.1 I briefly describe the PARSEC code and its major ingredients. In Section 4.2 I present the stellar evolution models computed with mass-loss recipes that account for both radiation-driven and pulsation-driven mass loss. I provide an overview of evolutionary properties, with emphasis on core evolution, dredge-up episodes, internal structure, surface elemental abundances, chemical ejecta, final evolution outcomes, and associated compact remnants. Finally, Section 4.3 closes the paper with some concluding remarks and future perspectives.

4.1 Stellar evolutionary calculations

Stellar evolutionary models are computed with the PARSEC (PAdova and tRieste Stellar Evolution Code) code version 2.0, as described in Bressan et al. (2012); Costa et al. (2019b, 2021) and references therein. The main input physics and other ingredients used in the evolutionary calculations are summarized below.

The FREEEOS code developed by A.W. Irwin[1] is used to calculate the equation of state. Using the procedure described in Timmes and Arnett (1999), I include the effect of pair creation in the equation of state. Radiative opacities are taken from the OPAL project (Iglesias and Rogers 1996) for high temperatures, and the ÆSOPUS code (Marigo and Aringer 2009) is used for low temperatures. Conductive opacities are included according to Itoh et al. (2008). Nuclear reaction rates – p-p chains, CNO tri-cycle, Ne-Na and Mg-Al chains, and the most important α-capture reactions, including (α, n) processes – together with the corresponding Q-values are taken from the JINA reaclib database (Cyburt et al. 2010b). I use the fitting formulae by Haft et al. (1994) for plasma neutrinos, and I follow Munakata et al. (1985) and Itoh and Kohyama (1983) to account for energy losses by electron neutrinos. To describe mixing, I use the mixing length theory (Böhm-Vitense 1958) with a fixed mixing-length parameter, $\alpha_{\rm mlt} = 1.74$, calibrated on present-day Sun's properties (Bressan et al. 2012). To test stability against convection I use the Schwarzschild criterion. I apply core overshooting[2] described by the parameter $\lambda_{\rm ov} = 0.4$. For convective envelopes, I use an undershooting distance of $\Lambda_{\rm env} = 0.7\,{\rm H_P}$ below the deepest unstable layer.

I consider two choices of the initial chemical composition defined by ($\mathrm{Z} = 0$, $\mathrm{Y} = 0.24850$) and ($\mathrm{Z} = 0.0002, \mathrm{Y} = 0.24885$) – where Z and Y denote the initial abundances of metals and helium in mass fraction, respectively –, and seven values of the initial mass, $\mathrm{M_i} = 100, 150, 200, 300, 500, 750, 1000\,\mathrm{M_\odot}$. The Y values are obtained using a primordial helium abundance of $\mathrm{Y_p} = 0.2485$ (Komatsu et al. 2011), and a helium-to-metals enrichment ratio $\Delta\mathrm{Y}/\Delta\mathrm{Z} = 1.78$ based on the current PARSEC solar calibration (Bressan et al. 2012). For $\mathrm{Z} = 0.0002$ the initial metal abundance distribution scales with the solar composition of Caffau et al. (2011).

For each combination $(\mathrm{M_i}, \mathrm{Z})$ I apply three recipes to describe the mass loss rate, $\dot{\mathrm{M}}$, by stellar winds, namely:

- $\dot{\mathrm{M}} = \dot{\mathrm{M}}_{\rm rdw}$: radiation-driven winds as implemented in PARSEC (Section 2.3);
- $\dot{\mathrm{M}} = \dot{\mathrm{M}}_{\rm pdw}$: pulsation-driven winds according to the formulation of (Nakauchi et al. 2020, Section 3.2);
- $\dot{\mathrm{M}} = \dot{\mathrm{M}}_{\rm max}$: the highest rate between the above two cases, $\dot{\mathrm{M}}_{\rm max} = \max(\dot{\mathrm{M}}_{\rm rdw}, \dot{\mathrm{M}}_{\rm pdw})$.

In total, I produced 6 sets of stellar models, each defined by the initial metallicity, Z, and mass loss prescription, $\dot{\mathrm{M}}$. Since models with $\dot{\mathrm{M}}_{\rm pdw}$ were intended mainly to explore the sensitivity of pulsation-driven mass loss to stellar mass and effective temperature, in the analysis that follows, I will focus on the 4 sets computed with $\dot{\mathrm{M}}_{\rm rdw}$ and $\dot{\mathrm{M}}_{\rm max}$.

[1] http://freeeos.sourceforge.net

[2] $\lambda_{\rm ov}$ is the mean free path of the convective element across the border of the unstable core, in units of pressure scale height, $\mathrm{H_P}$.

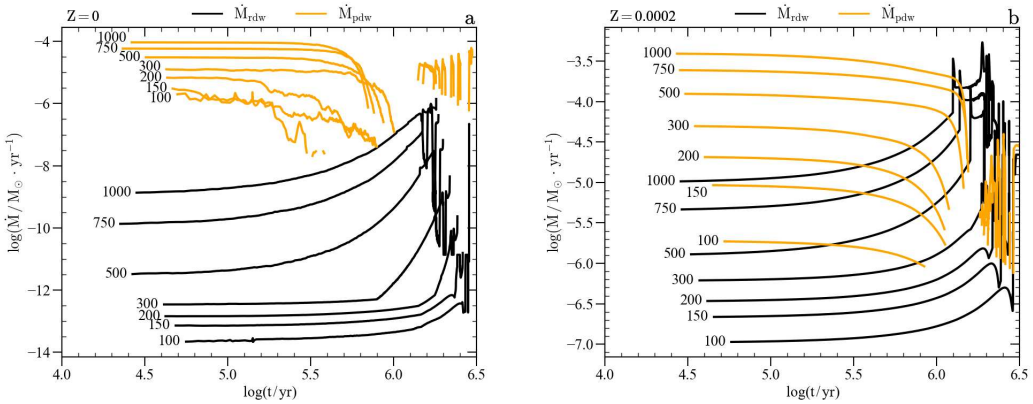

Figure 4.1: Mass-loss rate as a function of time, from the ZAMS phase, for tracks computed with only radiation-driven winds ($\dot{M}_{rdw}$, black) and only pulsation-driven winds ($\dot{M}_{pdw}$, orange). Close to each track the value of the initial mass (in $M_\odot$) is indicated. Note that the vertical axis range is not the same in the two panels.

4.1.1 Combined winds

Figure 4.1 compares the mass-loss rates associated with radiation-driven winds ($\dot{M}_{rdw}$; black lines) and pulsation-driven winds ($\dot{M}_{pdw}$; orange lines). The pulsation-driven mass loss dominates during the first phases of core hydrogen burning (cHB), while the radiation-driven mass loss is higher during cHeB for those tracks computed with initial metallicity Z = 0.0002. Given that the two types of mass loss generally dominate at different stages of evolution, I computed a set of evolutionary tracks based on the maximum mass-loss rate between $\dot{M}_{rdw}$ and $\dot{M}_{pdw}$, i.e. $\dot{M}_{max}$.

In both panels of Figure 4.1, $\dot{M}_{pdw}$ (orange lines) presents a gap at $\log(t/yr) \sim 6$. This is because the models are evolving to lower effective temperatures during the MS phase and at $\log(t/yr) \sim 6$ they have $T_{eff} < T_{eff,min}$. As a result, Equation (3.1) cannot be used further, and the models temporarily stop losing mass via the pulsation-driven mechanism. When the stellar tracks cool enough and their effective temperature attains $\log(T_{eff}) \leq 3.85$, pulsation-driven winds resume (see Equation 3.2). The models computed with Z = 0 exhibit an irregular behavior compared to those with Z = 0.0002. The cause should be linked to the scatter in the effective temperature trend, which most likely reflects some numerical noise in the convergence of the atmosphere

Comparing Figure 4.1 with Figure 3.1, I note that the mass-loss rate for tracks computed with Z = 0.0002 is very similar during the MS phase, while in the RSG phase $\log\left(\dot{M}_{pdw}\right)$ of my stellar models is ~ 1 dex lower. This could be explained by the difference in effective temperature between stellar tracks in the two studies (see Section 4.2.1). In fact, when compared to my PARSEC tracks, the Nakauchi et al. (2020) models stretch to lower effective temperatures in the RSG phases, resulting in higher mass-loss rates (Equation 3.2).

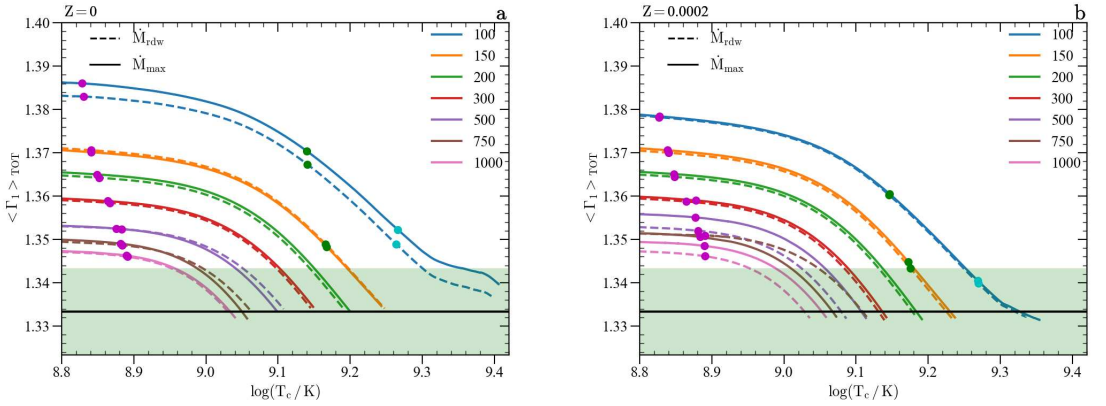

Figure 4.2: Mass-averaged first adiabatic exponent, $\langle\Gamma_1\rangle$, as a function of central temperature, and metallicity (*Panel a*: Z = 0, *Panel b*: Z = 0.0002). Results are shown for two mass loss cases, as indicated. The magenta, green, and cyan circles mark the beginning of core C, Ne, and O burnings, respectively. The thick black horizontal line denotes the threshold value of $\langle\Gamma_1\rangle = 4/3$. The green area shows where the star can be considered dynamically unstable due to pair creation, below $\langle\Gamma_1\rangle = 4/3 + 0.01$.

4.1.2 End of Evolutionary Calculations due to Pair-Creation Instability

During the most advanced stages of massive star evolution, the electron-positron creation process absorbs some of the plasma's thermal energy, lowering thermal pressure. As a consequence, non-ideal effects enter the equation of state, preventing temperature changes from causing pressure changes. The star's layers where this process occurs become dynamically unstable. For this purpose, I use the criterion first introduced by Stothers (1999), who demonstrated that the mass-weighted average of the first adiabatic exponent, $\Gamma_1 = (\partial \log \mathrm{P}/\partial \log \rho)_{\mathrm{ad}}$, integrated over the entire star, is a useful parameter for determining a star's dynamical stability. Specifically, at each time step, I evaluate

$$\langle\Gamma_1\rangle = \frac{\int_0^{\mathrm{M}} \frac{\Gamma_1 \mathrm{P}}{\rho} \mathrm{dm}}{\int_0^{\mathrm{M}} \frac{\mathrm{P}}{\rho} \mathrm{dm}}, \tag{4.1}$$

where M is the current star's mass, P is the pressure, ρ is the gas mass density, and dm is the mass element. The star is stable if $\langle\Gamma_1\rangle > \frac{4}{3}$; otherwise, dynamical instability occurs. Because the PARSEC code, by construction, assumes hydrostatic equilibrium, the dynamical collapse cannot be followed. Similarly to Costa et al. (2021), I interrupt the evolution as $\langle\Gamma_1\rangle$ falls below $4/3 + 0.01$, as first suggested by Marchant et al. (2019) and Farmer et al. (2019). All stellar models start from the ZAMS phase, progress to the end of the cHeB phase, and then ignite carbon in the core. Figure 4.2 shows the mass-averaged first adiabatic exponent, $\langle\Gamma_1\rangle$, as a function of central temperature. In panels a and b most models become dynamically unstable close to the end of core carbon burning (cCB), while those with $\mathrm{M_i} = 150\,\mathrm{M_\odot}$ and $\mathrm{M_i} = 100\,\mathrm{M_\odot}$ do so after the ignition of neon or oxygen burning in the core, respectively. This happens when pair creation makes $\langle\Gamma_1\rangle$ enter the critical regime and reach or bypass the 4/3 threshold.

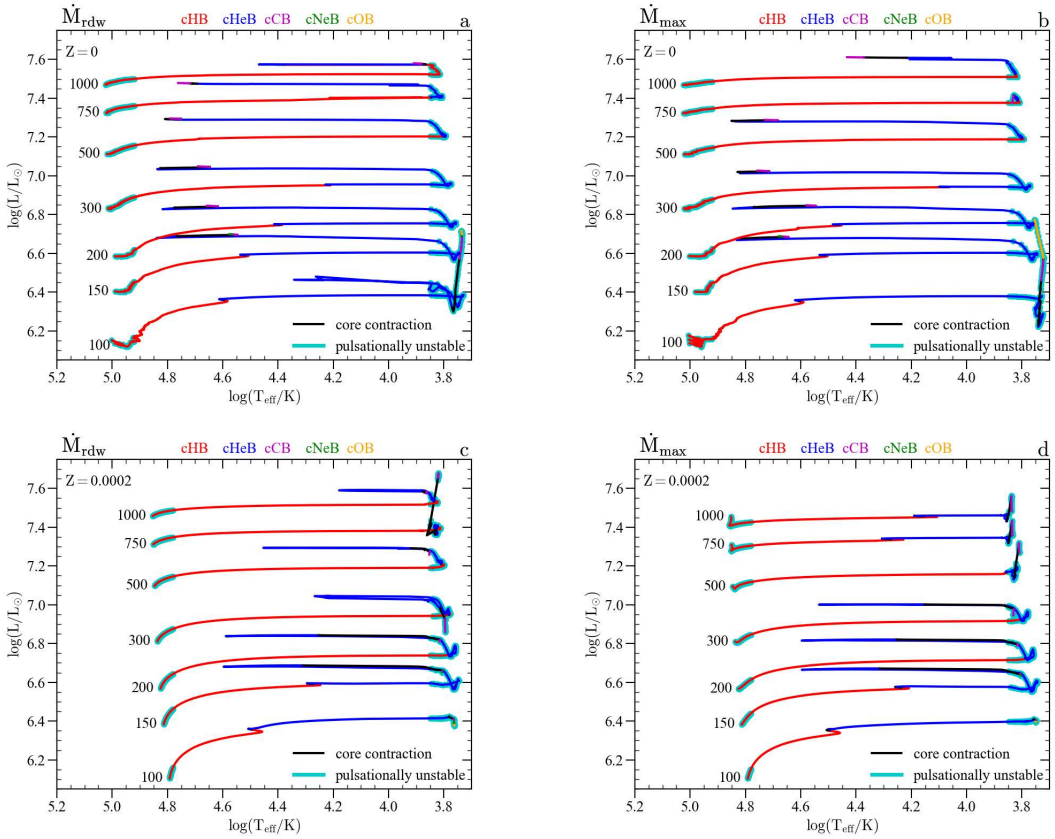

Figure 4.3: H-R diagrams of the four sets of tracks computed in this work. Different evolutionary phases are color-coded, as written in the legend. Panels *a,b* and *c,d* refer to Z = 0 and Z = 0.0002, respectively. *Panels a,c*: Tracks computed with the standard PARSEC mass-loss prescription for radiation-driven winds. *Panels b,d*: Tracks computed taking into account also the pulsation-driven winds. Close to each track the value of initial mass (in $M_\odot$) is indicated. The cyan band superimposed on the tracks indicates where stars should be unstable against radial pulsation following Nakauchi et al. (2020).

4.2 Results

4.2.1 General Properties of the Stellar Evolutionary Tracks

Table 4.1 presents several quantities of the models that are key for discussing their evolution and final outcome.

Figure 4.3 shows all evolutionary tracks in the HRD, computed with $\dot{M}_{rdw}$ and $\dot{M}_{max}$. The initial metallicity influences the position of the tracks. Models with Z = 0 start their evolution at higher temperatures and luminosities than those with Z = 0.0002. The absence of metals reduces opacity and mean molecular weight, while the structures become more compact. In massive stars at Z = 0, before the MS, due to the lack of CNO nuclei, gravitational contraction cannot be stopped until the central temperature and density are high enough for the synthesis of primary carbon via the triple-α process when the star is still in the MS (e.g., Marigo et al. 2001).

Table 4.1: Relevant Properties of Models Computed with $\dot{M}_{rdw}$ and $\dot{M}_{max}$

M_i [$M_\odot$]	τ_{MS} [Myr]	τ_{cHeB} [Myr]	$f_{H\,puls}$	$f_{He\,puls}$	Blue Loop	DUP	M_{He} [$M_\odot$]	M_{CO} [$M_\odot$]	M_f [$M_\odot$]	X_{core} onset PI	L_ν/L_{rad} [$\log_{10}$]	Fate	remnant	M_{BH} [$M_\odot$]
(1)	(2)	(3)	(4)	(5)	(6)	(7)	(8)	(9)	(10)	(11)	(12)	(13)	(14)	(15)
$Z = 0\ \dot{M}_{rdw}$														
100	2.54	0.25	0.07	0.51	✓	✓	41.8	38.4	99.9	0.511 O	2.7	fCCSN[a]	BH	89.9
												PPISN[b]	BH	34.2
150	2.33	0.23	0.30	0.36	✓	✓	74.4	67.7	149.9	0.011 Ne	3.1	PISN	×	-
200	2.16	0.22	0.27	0.35	✓	✓	110.4	103.8	199.9	0.001 C	3.2	PISN	×	-
300	1.92	0.21	0.53	0.41	✓	✓	162.5	158.6	299.9	0.013 C	3.2	DBH	BH	299.9
500	1.76	0.20	0.51	0.61	×	✓	279.2	270.2	499.9	0.029 C	3.3	DBH	BH	499.9
750	1.64	0.19	0.49	0.64	×	✓	424.1	410.6	749.8	0.034 C	3.5	DBH	BH	749.8
1000	1.59	0.19	0.54	0.00	✓	✓	565.5	547.0	999.7	0.028 C	3.6	DBH	BH	999.7
$Z = 0\ \dot{M}_{max}$														
100	2.59	0.26	0.17	0.51	×	✓	37.1	34.3	95.0	0.412 O	2.8	fCCSN[a]	BH	85.5
												PPISN[b]	BH	30.9
150	2.33	0.23	0.32	0.36	✓	✓	77.5	72.6	147.7	0.019 Ne	3.1	PISN	×	-
200	2.15	0.22	0.30	0.35	✓	✓	102.9	95.1	197.6	0.001 C	3.2	PISN	×	-
300	1.92	0.22	0.52	0.41	✓	✓	159.9	157.4	290.6	0.011 C	3.3	DBH	BH	290.6
500	1.76	0.20	0.52	0.51	✓	✓	270.6	269.0	480.9	0.028 C	3.4	DBH	BH	480.9
750	1.66	0.20	0.55	0.99	×	✓	407.6	380.0	714.5	0.035 C	3.6	DBH	BH	714.5
1000	1.60	0.19	0.56	0.89	✓	✓	548.3	527.1	950.9	0.031 C	3.6	DBH	BH	950.9
$Z = 0.0002\ \dot{M}_{rdw}$														
100	2.83	0.25	0.29	0.57	×	✓	53.8	47.6	94.3	0.865 O	3.1	PPISN	BH	40.9
150	2.45	0.24	0.45	0.32	✓	✓	79.5	71.8	146.4	0.080 Ne	3.2	PISN	×	-
200	2.25	0.23	0.50	0.33	✓	✓	110.3	100.7	193.9	0.003 C	3.2	PISN	×	-
300	2.05	0.22	0.56	0.77	✓	✓	165.8	150.4	274.2	0.027 C	3.4	DBH	BH	274.2
500	1.88	0.20	0.61	0.44	✓	✓	289.1	265.8	448.9	0.041 C	3.4	DBH	BH	448.9
750	1.77	0.21	0.62	0.99	×	✓	330.1	330.0	662.6	0.020 C	2.8	DBH	BH	662.6
1000	1.71	0.19	0.60	0.54	✓	✓	575.6	534.6	831.7	0.029 C	3.6	DBH	BH	831.7
$Z = 0.0002\ \dot{M}_{max}$														
100	2.84	0.26	0.28	0.95	×	✓	53.1	46.9	92.7	0.859 O	3.1	PPISN	BH	40.4
150	2.47	0.24	0.44	0.38	✓	✓	77.0	69.3	139.7	0.055 Ne	3.2	PISN	×	-
200	2.29	0.23	0.49	0.36	✓	✓	105.7	96.2	180.2	0.002 C	3.2	PISN	×	-
300	2.09	0.22	0.59	0.53	✓	✓	157.1	142.2	249.3	0.023 C	3.3	DBH	BH	249.3
500	1.92	0.22	0.74	0.98	×	✓	220.6	207.8	355.8	0.035 C	3.2	DBH	BH	355.8
750	1.83	0.21	0.83	0.39	×	✓	342.8	318.5	472.9	0.036 C	3.4	DBH	BH	472.8
1000	1.77	0.20	0.85	0.11	×	✓	428.6	404.9	610.1	0.032 C	3.4	DBH	BH	610.1

NOTE—The table entries are as follows: (1) star's initial mass; (2) MS lifetime; (3) cHeB lifetime; (4) and (5) fractions of MS and cHeB lifetimes in which the star is unstable to radial pulsation; (6) and (7) occurrence of blue loop and dredge-up episode; (8) final He core mass; (9) final C-O core mass; (10) final mass of the star at the onset of dynamical instability; (11) central fuel abundance of ongoing nuclear burning at the onset of dynamical instability; (12) neutrino luminosity to radiative luminosity ratio when $T_c = 10^9$ K; (13) and (14) final fate and associated outcome (BH or complete disruption), and (15) BH mass.

[a] failed CCSN. Following Farmer et al. (2019) I set the lower limit of M_{He} for PPISN at $45\,M_\odot$.

[b] Following Woosley (2017) I set the lower limit of M_{He} for PPISN at $34\,M_\odot$.

Looking at the diagrams of Figure 4.3, during their MS, most massive tracks at $Z = 0.0002$, computed with $\dot{M}_{max}$ are less luminous than those computed with $\dot{M}_{rdw}$. This is most evident in the bottom panels of Figure 4.3. At the start of the MS phase the most massive $Z = 0.0002$ models with pulsation-driven mass loss (panel d) evolve almost vertically downward due to mass-loss rates as high as $10^{-4.4} - 10^{-3.4}\,M_{\odot}\cdot yr^{-1}$ (see Figure 4.1). Conversely, models with radiation-driven winds (panel c) suffer from very small mass-loss rates, resulting in no luminosity decrease on the MS. At $Z = 0.0002$ the luminosity difference on the MS, $\Delta \log(L) = \log(L)_{\dot{M}_{rdw}} - \log(L)_{\dot{M}_{max}}$, is not dramatic. It increases with M_i and does not exceed 0.1 dex.

This behavior is well explained by the positive correlation between mass and luminosity on the MS, with $L \propto M^{\eta}$ where $\eta > 0$. Compared to the standard value $\eta \simeq 3.5 - 4.0$ for MS stars in the range $1 \lesssim M_i/M_{\odot} \lesssim 10$, the mass-luminosity relation flattens out at higher masses, due to the increasing contribution of radiation pressure in the central core. Following the similarity theory of stellar structure adopted by Nadyozhin and Razinkova (2005) to study the properties of very massive stars on the MS, I find that $\eta \approx 1.0$ for stars in the range $100 \lesssim M_i/M_{\odot} \lesssim 1000$. According to my models, the relation is a bit steeper with $1.2 \lesssim \eta \lesssim 1.6$.

After the MS the luminosity difference, $\Delta \log(L)$, between models computed with $\dot{M}_{rdw}$ and $\dot{M}_{max}$ persists for tracks with $Z = 0.0002$, not exceeding $\simeq 0.15$ dex. Despite being much less pronounced, an analog luminosity difference (few 0.01 dex) affects models with $Z = 0$ as well. In general, $\Delta \log(L)$ between each pair of tracks increases with increasing initial mass for both $Z = 0$ and $Z = 0.0002$. This reflects the dependence of the pulsation-driven mass-loss rate on the current stellar mass in Equations (3.1) and (3.2).

The decrease in luminosity is also present in the stellar models of Nakauchi et al. (2020), especially in the HRD in their Figure 6c, which shows a set of tracks computed with $Z = 0.0002$. The location of the ZAMS is similar in the two studies, while during the RSG phases Nakauchi et al. (2020)'s tracks achieve lower effective temperatures than my PARSEC models.

As stars exhaust hydrogen in their cores, they evolve towards lower effective temperatures, moving to the right in the HRD. Then, during the helium burning phase, 18 tracks out of 28 experience a blue loop, 2 stars evolve towards higher effective temperatures becoming blue supergiants, while the remaining 8 tracks stay at $\log(T_{eff}) \sim 3.8$ as red supergiants until the end of their evolution. After central He exhaustion, the stellar core contracts until it reaches the temperature required to ignite carbon. Regardless of whether the stars become dynamically unstable, the evolution after cHeB is greatly accelerated by neutrino emission (see L_{ν}/L_{rad} in Table 4.1), so that the position of the tracks in the HRD does not change significantly at later stages.

When a very massive star evolves towards decreasing T_{eff} and approaches its Hayashi line becoming a red supergiant, a dredge-up episode is likely to occur. While the convective envelope inflates and cools, the opacity, which is regulated by a Kramers-like law, increases so that the radiative temperature gradient exceeds the adiabatic one in the progressively deeper layers of the envelope. As a result, the bottom of the convective envelope stretches inward, passing over the H-He discontinuity and penetrating the He core. As a consequence, helium and nitrogen, newly synthesized by the CNO cycle, are dredged up to the surface, leading to a net increase in the effective metallicity. The

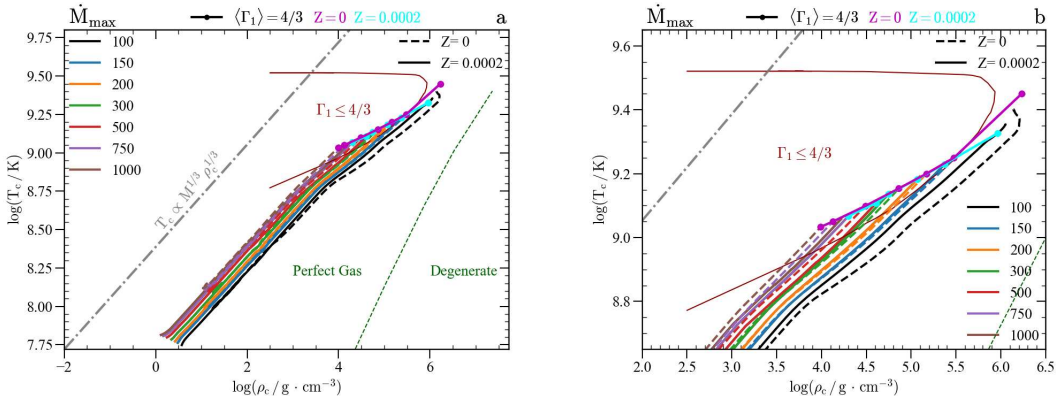

Figure 4.4: *Panel a*: Evolutionary tracks in the central temperature vs central density diagram, from the ZAMS to the onset of dynamical pair-creation instability. *Panel b*: Zoom in the unstable region. The red curve, taken from Kozyreva et al. 2014, approximates the locus of points where $\Gamma_1 = 4/3$. The cyan (magenta) dots correspond to the points in the PARSEC Z = 0.0002 (Z = 0) models where $\langle\Gamma_1\rangle = 4/3$. The point-dashed line, with slope 1/3, shows the evolution during a homologous contraction.

dredge-up may also occur during cHeB; in this case, the envelope may extend deeper into the developing C-O core, enriching the surface with He, C, and O. Section 4.2.3 examines the impact of dredge-up on surface abundances and chemical ejecta.

4.2.2 Physical Overview

Here I will discuss some relevant properties of the models, with a particular focus on the physical structure.

Evolution of the Stellar Centre Figure 4.4 shows the central density vs central temperature diagram of all models computed with $\dot{M}_{max}$. The general behavior of the tracks can be explained by considering the simple scaling relation

$$T_c \propto M^k \rho_c^{1/3} , \tag{4.2}$$

which describes the evolution of the center during a homologous contraction. The strict validity of the relation requires the fulfillment of various conditions (e.g., constant polytropic index, constant ideal-gas pressure fraction, negligible thermal neutrino losses), which are usually not met by massive stars in advanced evolutionary stages. Nonetheless, the same relation may be useful to capture some fundamental dependence of the star's center evolution, as a first approximation.

The exponent k depends on the equation of state. If the classical ideal gas contribution dominates the total pressure, k = 2/3; if instead the radiation pressure dominates the total pressure, k = 1/3 (Eddington 1926). For a polytropic star, the ratio of the gas pressure to the total pressure, $\beta = P_{gas}/P_{tot}$ depends on the mass of the star

$$\beta^{1/3}(1+\beta) \propto M^{2/3} . \tag{4.3}$$

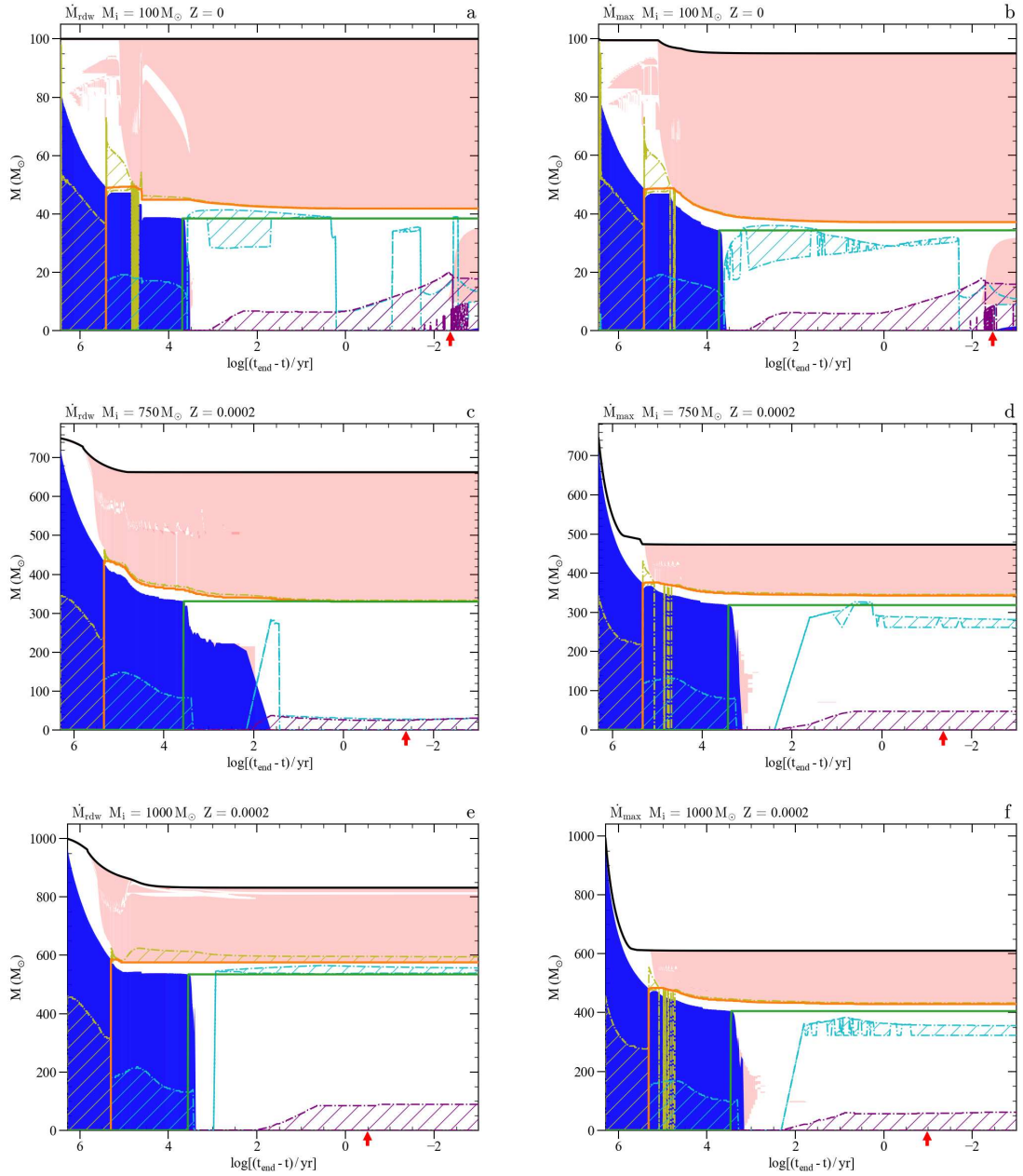

Figure 4.5: Kippenhahn diagrams of selected models. The horizontal axis represents the logarithm of time (in yr) until the onset of pair-creation dynamical instability. The blue regions in each diagram represent the star's convective core, the pink area corresponds to the convective envelope, semi-convective zones at the boundary of the helium convective core, and convective shells. The yellow, cyan, and purple hatch regions represent the hydrogen, helium, and carbon-burning core/shells, respectively. The black continuous line shows the total mass of the star, the orange one corresponds to the helium core, and the green one indicates the carbon-oxygen core. The red arrow marks the time when the star enters the unstable region with $\langle \Gamma_1 \rangle = 4/3 + 0.01$. *Panels a,c,e*: Models computed with the standard PARSEC mass-loss prescription for radiation-driven winds. *Panels b,d,f*: Models that include also pulsation-driven winds.

Following Zel'dovich et al. (1981) and Eddington (1926) the stellar mass at which $\beta \simeq 1/2$ roughly corresponds to $M \simeq 50\,M_\odot$. The role of radiation pressure increases with mass, so I can reasonably take $k = 1/3$ for my very massive stars. Looking at Figure 4.4, the tracks run almost parallel to the homologous contraction sequence (with slope 1/3), except for the last advanced stage, where some bending towards lower T_c occurs, primarily driven by neutrino cooling. The factor $M^{1/3}$ in Equation (4.2) well explains why less massive stars reach lower T_c for given ρ_c.

As previously discussed in Section 4.1.2, most models undergo dynamical instability as a result of pair creation during carbon burning, except the $M_i = 100, 150\,M_\odot$ models, which experience this condition later, after the onset of oxygen and neon burning, respectively. This is evident in the $\rho_c - T_c$ diagram, as almost all of the tracks enter the $\Gamma_1 < 4/3$ region (red curve, taken from Kozyreva et al. 2014). The models with $M_i = 100\,M_\odot$ do not appear to cross the critical boundary, whereas the integration of Equation (4.1) yields the opposite result (cyan and magenta circles). The apparent discrepancy is misleading. In fact, the red curve in Figure 4.4 defines the locus where $\Gamma_1 = 4/3$ in the center, whereas my $M_i = 100\,M_\odot$ models experience off-center pair creation and do enter the unstable region, as illustrated in Figure 4.2.

Figure 4.5 shows the Kippenhahn diagrams of a few selected models computed with $\dot{M}_{rdw}$ (left panels) and $\dot{M}_{max}$ (right panels). One distinguishing feature of very massive stars is that, even in the absence of rotation or other mixing processes, they evolve nearly homogeneously during the MS phase because they develop very large convective cores, initially covering up to ≈ 80 percent of the total mass. As hydrogen is burned, convective cores gradually recede due to the significant contribution of the radiation pressure P_{rad} ($P/T^4 \propto P/P_{rad} \propto (1-\beta)^{-1}$), and decreasing electron scattering opacity ($\kappa_{es} \simeq 0.2\,(1+X)\,cm^2\,g^{-1}$). Both factors concur to lower the radiative temperature gradient. The MS lifetime ranges from $\simeq 2.8$ Myr to 1.6 Myr passing from $M_i = 100\,M_\odot$ to $M_i = 1000\,M_\odot$.

The fraction of the MS lifetime where pulsation instability occurs is significant, as shown in Table 4.1, and it increases with stellar mass and metallicity. For example, the ($M_i = 1000\,M_\odot$, $Z = 0.0002$, $\dot{M}_{max}$) model experiences radial pulsation and associated mass loss for ≈ 85 percent of its MS phase. As a result, the reduction in stellar mass ($\dot{M}_{max}$ case) is much greater than in the case of weak radiative winds ($\dot{M}_{rdw}$ case). For the former model, the stellar mass at the end of the MS phase is $M = 611\,M_\odot$, while the latter has $M = 885\,M_\odot$. During the subsequent cHeB phase, all tracks develop convective cores. The cHeB lifetimes are roughly 0.1 the MS duration, as expected.

In Section 4.2 I mentioned the possibility of a star experiencing dredge-up episodes as it approaches its Hayashi line. This is most common during the cHeB phase (see the H-R tracks of Figure 4.3) when the envelope extends deeper into the He or C-O core. This occurs, for example, in the $M_i = 100\,M_\odot$ models at $Z = 0$ (panels a,b). Using $\dot{M}_{rdw}$, the star experiences a first dredge-up (DUP) that enters the He core, followed by a second DUP that extends into the forming C-O core. As we will see in Section 4.2.3, the first mixing episode causes a dramatic increase in N at the surface, whereas the second episode enriches the envelope primarily with C and O. The same phenomenon occurs in the $M_i = 100\,M_\odot$ with $\dot{M}_{max}$, but in this case the envelope deepens more gradually. Similar considerations apply when comparing the ($M_i = 750, 1000\,M_\odot$; $Z = 0.0002$) models, computed with $\dot{M}_{rdw}$ and $\dot{M}_{max}$.

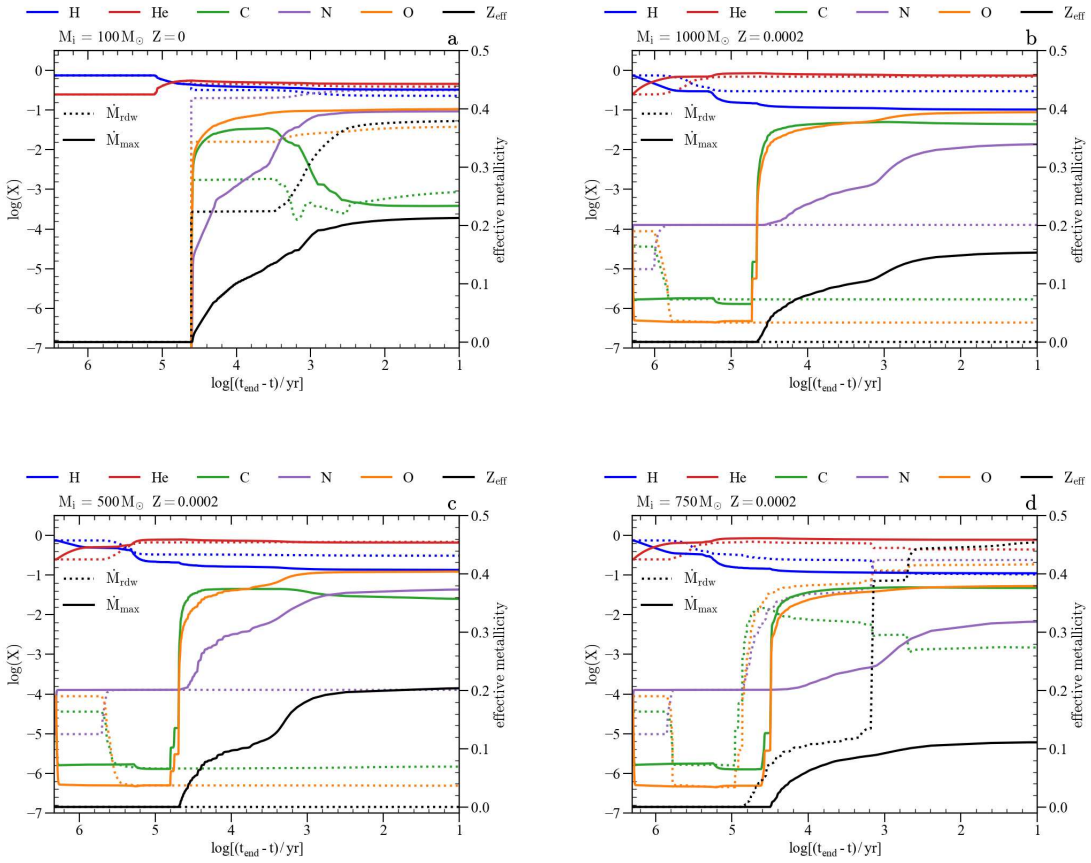

Figure 4.6: Evolution of surface chemical abundances of four selected models, from the ZAMS to the onset of dynamical instability. In each panel, the abundances of five elements, namely hydrogen, helium, carbon, nitrogen, and oxygen, are depicted in different colors. The effective metallicity, $Z_{\rm eff}$, is shown in black. The results are presented for two different mass-loss prescriptions. The horizontal axis is the logarithm of time (in yr) until the onset of dynamical instability.

All structures displayed in Figure 4.5 become dynamically unstable due to the pair creation in different stages of evolution (see Section 4.1.2 and Table 4.1).

4.2.3 Surface Chemical Abundances

Here I discuss the evolution of the surface abundances which can be modified by dredge-up episodes, as well as the composition of the chemical ejecta which is also affected by stellar wind efficiency.

Figure 4.6 shows the surface abundance evolution of a few relevant nuclides in some selected models. Each panel compares the results for a model with the same initial mass, obtained with two mass loss prescriptions, namely $\dot{M}_{\rm rdw}$ (dotted lines) and $\dot{M}_{\rm max}$ (solid lines).

In Section 4.2.1 I have already discussed the main characteristics of these mixing

events, especially concerning the Kippenhahn diagrams (Figure 4.5), to which the reader should refer for better comprehension. All models depicted in Figure 4.6 experience a DUP episode but with varying degrees of envelope penetration. Very deep DUPs occur in the ($M_i = 100\,M_\odot$, $Z = 0$) and ($M_i = 750\,M_\odot$, $Z = 0.0002$, $\dot{M}_{rdw}$) models, as discussed below.

In general, the models with DUP display a surface depletion of H and an increase in ^{4}He, ^{14}N, ^{12}C, and ^{16}O. When the envelope crosses the H-He discontinuity and enters the He core, which contains the products of complete H-burning through the CNO cycle, ^{4}He and ^{14}N are enriched at the surface. This situation is best illustrated (panel a) by the ($M_i = 100\,M_\odot$, $Z = 0$, $\dot{M}_{rdw}$) model, where there is a sudden and significant increase in ^{14}N, just as the bottom of the convective envelope stretches into the He core. At the same time, even though the CNO cycle depletes ^{12}C and ^{16}O in the He core in favor of ^{14}N, their surface abundances increase because the material extracted from the He core is diluted in the envelope, which initially contains no metals ($Z = 0$).

As the envelope deepens, its base may even reach and enter the forming carbon-oxygen core, e.g. ($M_i = 750\,M_\odot$, $Z = 0.0002$, $\dot{M}_{rdw}$) model in Figure 4.5 panel c, where ^{4}He is burned into ^{12}C and ^{16}O, while ^{14}N is gradually converted into ^{22}Ne via the chain $^{14}N(\alpha,\gamma)^{18}F(\beta^+\nu)^{18}O(\alpha,\gamma)^{22}Ne$. The chemical enrichment in the ($M_i = 100\,M_\odot$, $Z = 0$, $\dot{M}_{max}$) model is more gradual than the analog for $\dot{M}_{rdw}$, and it misses the abrupt initial jump in ^{14}N abundance. Overall, differences in surface abundance evolution between models with the same initial mass but different mass-loss rates reflect differences in chemical profiles, opacity, and convective border details. DUP results in a net increase in surface effective metallicity ($Z_{eff} = 1 - X - Y$; dotted/solid black lines). The case of the ($M_i = 100\,M_\odot$, $Z = 0$, $\dot{M}_{rdw}$) model is particularly noteworthy, with Z_{eff} increasing as high as 0.38, owing the large ^{14}N abundance. For both mass-loss prescriptions, the occurrence of the DUP significantly reduces the He core mass, which passes from $M_{He} \simeq 48\,M_\odot$ at the end of MS to $M_{He} \simeq 37\,M_\odot$ with $\dot{M}_{max}$, and $M_{He} \simeq 42\,M_\odot$ with $\dot{M}_{rdw}$. Such reduction is especially important for the final outcome of these models (see Section 4.2.4).

Figure 4.7 presents the chemical ejecta of He, C, N, O, Ne, and Mg, for a few models. Each panel contains the results of two mass-loss prescriptions, as indicated in the legend. Tables of wind ejecta can be found at this link[3]. Chemical ejecta computed with $\dot{M}_{rdw}$ are, as expected, lower than those computed with $\dot{M}_{max}$, since this latter takes the maximum of ($\dot{M}_{rdw}, \dot{M}_{pdw}$), by construction. I verified that the main difference in the ejected mass of all the considered elements is caused by mass loss for each pair of tracks in Figure 4.7. The only exception is nitrogen, whose ejecta is higher in the ($M_i = 100\,M_\odot$, $Z = 0$) model with $\dot{M}_{rdw}$ due to a deeper dredge-up episode. Furthermore, while wind ejecta masses are greater for $Z = 0.0002$ than for $Z = 0$, we can see that, regardless of metallicity, large amounts of helium, up to several tens or few hundreds of solar masses, are expelled from the most massive models.

4.2.4 Final fate

Figure 4.8 (left panel) shows the helium core mass, M_{He}, at the onset of pair-creation dynamical instability for all tracks. Overall, there is a positive correlation between M_i and M_{He}. A deep DUP causes a sudden change in slope at $M_i = 750\,M_\odot$ in the ($Z =$

[3] https://zenodo.org/record/7528650

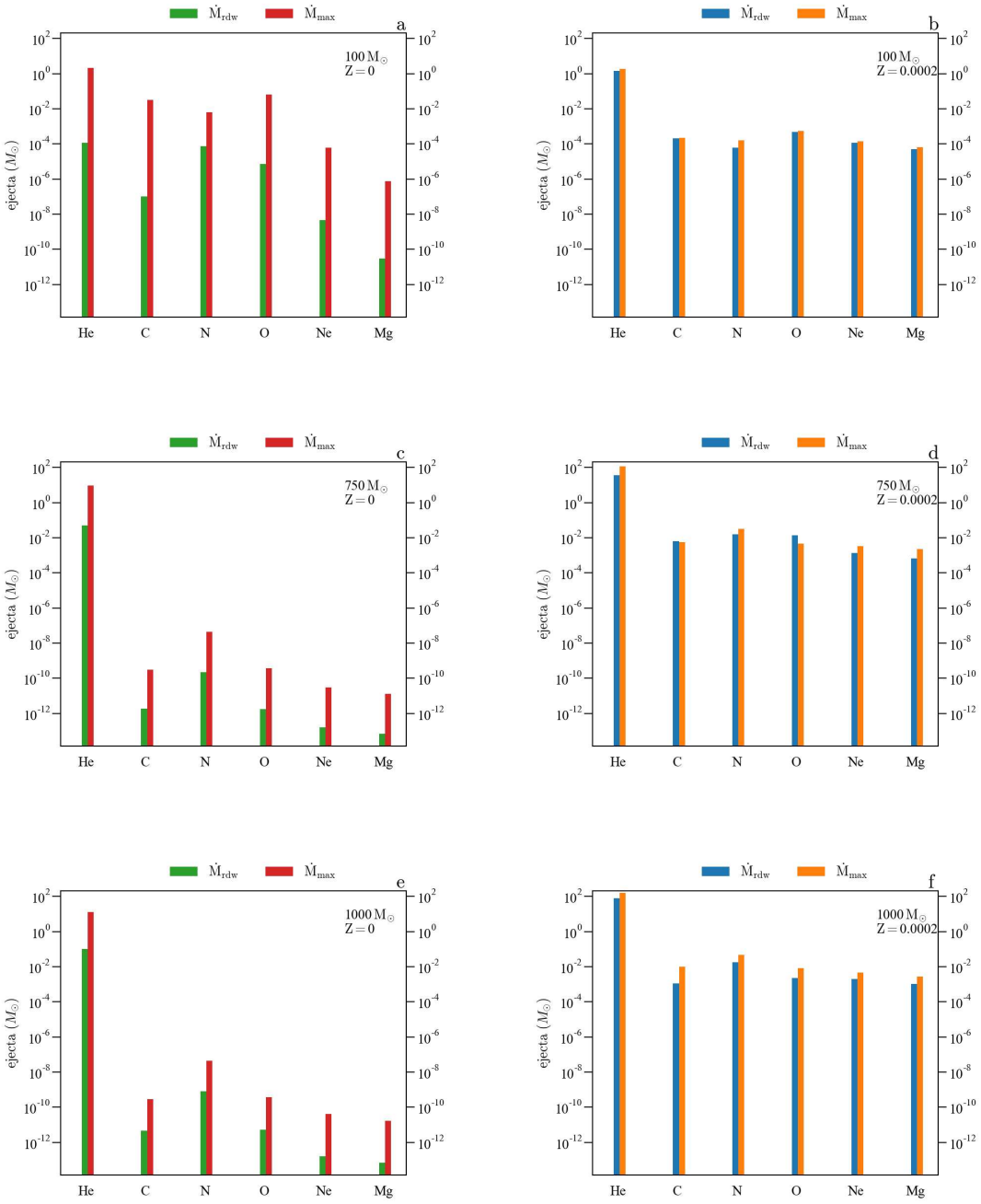

Figure 4.7: Ejecta mass of models with three selected initial masses, namely $M_i/M_\odot$ = 100, 750, 1000. Each panel shows the ejecta mass of helium, carbon, nitrogen, oxygen, neon, and magnesium for two mass-loss recipes, $\dot{M}_{rdw}$ and $\dot{M}_{max}$. *Panels a,c,e*: Models computed with Z = 0. *Panels b,d,f*: Models computed with Z = 0.0002.

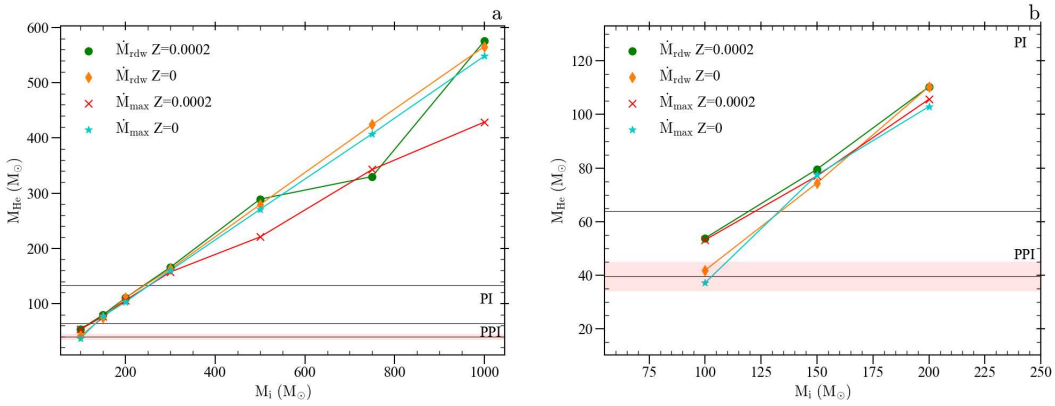

Figure 4.8: *Panel a*: Helium core mass, M_{He}, as a function of the initial mass for all models of four different sets as stated in the legend. Helium core mass is evaluated at the onset of dynamical instability. Horizontal lines delimit the regimes in which pulsation-pair instability, pair-instability explosion, and direct collapse to black holes are expected (Woosley 2017; Farmer et al. 2019, 2020). *Panel b*: Zoom in the $100 \leq M_i/M_\odot \leq 200$ range. The red strip indicates the uncertainty range of the lower limit for pulsation-pair instability. Lower and upper boundaries are $34\,M_\odot$ (Woosley 2017), and $45\,M_\odot$ (Farmer et al. 2019), respectively. The black line is the average.

0.0002, $\dot{M}_{rdw}$) sequence. When I consider tracks of the same metallicity, I can see that models computed with $\dot{M}_{max}$ end up with smaller M_{He}. The effect is more pronounced at $Z = 0.0002$, because the mass reduction on the MS through $\dot{M}_{max}$ is much stronger than with $\dot{M}_{rdw}$.

I can see that, regardless of metallicity or mass-loss prescription, stars with $M_i \geq 300\,M_\odot$ should avoid the pair-instability supernova channel and collapse directly to a black hole. In fact, their He cores have masses that exceed the limit of $130 \lesssim M_{He}/M_\odot \lesssim 133 - 139$ (Woosley and Heger 2021; Farmer et al. 2020; Woosley 2017; Woosley et al. 2007). Instead, stars with $M_i = 150, 200\,M_\odot$ have He cores that are just massive enough to cause the pair-instability explosion, leading to total disruption. Finally, stars with $M_i = 100\,M_\odot$ should experience pulsational-pair instability (PPI) or end as failed CCSN, resulting in the formation of a black hole as a compact remnant.

To a first approximation, the final mass, M_f, at the end of the hydrostatic evolution provides a rough estimate of the remnant BH mass for stars that undergo DBH. While the BH mass for a PISN is simply zero, for PPISN I use the formula proposed by (Spera and Mapelli 2017, with the corrections of Mapelli et al. 2020), which fits the results of Woosley (2017)'s hydrodynamic calculations. I also account for the mass loss due to the neutrino emission, which I set equal to $0.1\,M_{bar}$, where M_{bar} is the baryonic mass of the proto-compact object (Fryer et al. 2012; Rahman et al. 2022, and references therein). The PPISN configuration applies to the ($M_i = 100\,M_\odot$, $Z = 0.0002$) models, whereas for the ($M_i = 100\,M_\odot$, $Z = 0$) models the fate is somewhat uncertain. The star with $\dot{M}_{max}$ has a helium core mass of $\simeq 37\,M_\odot$. I can assess its outcome by comparing M_{He} to the lower limit for the development of PPI. According to Woosley (2017) the threshold is around $34\,M_\odot$, while Farmer et al. (2019) indicate it is about $45\,M_\odot$.

On the one hand, if I follow Woosley (2017) the ($M_i = 100\,M_\odot$, Z = 0, $\dot{M}_{max}$) star should be able to enter the PPISN regime, producing a BH of mass $\simeq 30.9\,M_\odot$. On the other hand, if I follow Farmer et al. (2019) the same star should avoid the PPISN path and complete the entire sequence of nuclear burnings up to the formation of an iron core, which eventually collapses, resulting in a failed CCSN, assuming efficient fall-back (Fryer et al. 2012, delayed model). The estimated BH mass would be $\simeq 85.5\,M_\odot$, under the hypothesis that $\simeq 0.1\,M_f$ is lost due to neutrino emission.

I observe that the analysis of Farmer et al. (2019) relies on pure He-models, while my calculations follow the evolution of complete models. In this respect the stability analysis based on $\langle\Gamma_1\rangle$ is primarily controlled by the core mass and its chemical composition, with a small influence from the residual envelope (e.g., Costa et al. 2021, Tables A1 and A2). As a result, taking the lower threshold limit of Farmer et al. (2019) is still a reasonable assumption for my exploratory study. In general, differences in the mass limits of the pair-creation instability window reflect differences in the input physics among various sets of models.

Based on the dense grid of PARSEC models computed by Costa et al. (2021), the lower limit for entering the PPISN regime is $M_{He} \simeq 36 - 39\,M_\odot$, if I take the threshold for the onset of PI at $\langle\Gamma_1\rangle = 4/3 + 0.01$. This value is roughly halfway between the boundaries indicated by Woosley (2017) and Farmer et al. (2019). If I take the threshold for the onset of PI strictly at $\langle\Gamma_1\rangle = 4/3$ the lower boundary for PPISN in the Costa et al. (2021) models shifts at $M_{He} \simeq 48\,M_\odot$.

my structure calculations of the ($M_i = 100\,M_\odot$, Z = 0, $\dot{M}_{max}$) track suggest that during the onset of O-burning, the mass-averaged $\langle\Gamma_1\rangle$ is approaching the critical value of 4/3 due to pair creation. If this threshold was exceeded at some later stage ($\langle\Gamma_1\rangle < 4/3$), then the star would enter the PPISN regime. Similar considerations apply to the ($M_i = 100\,M_\odot$, Z = 0, $\dot{M}_{rdw}$) model.

Table 4.1 and Figure 4.9 compare the results obtained with different mass-loss prescriptions. my calculations show that low-metallicity very massive stars can produce BH with masses exceeding $\sim 100\,M_\odot$. The most massive BH are produced by very massive stars with Z = 0, as mass loss is modest. The final mass of my models with $300 \leq M_i/M_\odot \leq 1000$ is higher with respect to those of Nakauchi et al. (2020, Figure 8). At Z = 0 the difference is at most $\sim 7\%$, while for models computed with Z = 0.0002 the difference is at most $\sim 24\%$. This reflects the difference in mass-loss rates between the two sets of models, which is mostly caused by the different evolution of the effective temperature (see Sections 4.1.1 and 4.2.1).

4.3 Concluding Remarks

In this study, I investigate the evolution of zero-metallicity (Z = 0) and extremely metal-poor (Z = 0.0002) very massive stars, with initial masses ranging from $100\,M_\odot$ to $1000\,M_\odot$. These calculations extend the PARSEC evolutionary models in the very high mass regime. One novel element is the inclusion of pulsation-driven winds, following the findings of a recent study (Nakauchi et al. 2020), in which a stability analysis against radial pulsation is performed. In addition to pulsation-driven mass loss, I consider also the occurrence of radiation-driven winds in both the hot and cool regions of the HRD. I find that the two mechanisms prevail at different stages. In particular, the

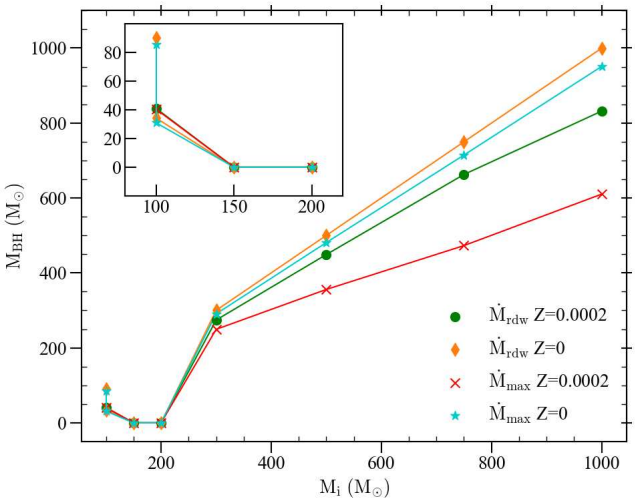

Figure 4.9: Black hole mass as a function of the initial mass for all tracks presented in this work. The inset plot zooms in the $100 \leq M_i/M_\odot \leq 200$ range. The two cyan starred and orange diamond symbols correspond to the ($M_i = 100\,M_\odot$, Z = 0, $\dot{M}_{max}$) and ($M_i = 100\,M_\odot$, Z = 0, $\dot{M}_{rdw}$) models, respectively. They indicate the predicted BH masses, depending on whether the star results in a failed CCSN or PPISN. See also Table 4.1.

amount of mass ejected by the most massive models through radial pulsations during the MS can be substantial, in contrast to the modest outflows expected via momentum absorption from radiation.

All models are followed until the onset of dynamical instability caused by the creation of electron-positron pairs, which occurs near the end of cCB or shortly after the start of neon or oxygen burning, depending on the initial mass. I extract the criterion to assess the final outcome of the models and the type of compact remnant, based on full computations (Kozyreva et al. 2014; Woosley 2017; Farmer et al. 2019).

I find that stars with $M_i \geq 300\,M_\odot$ should end their lives without exploding, instead directly collapsing to BHs. My models with $M_i = 150\,M_\odot$ and $M_i = 200\,M_\odot$ should produce PISN, leaving no remnant and thus contributing to the primordial black-hole mass gap.

Depending on metallicity and mass loss, models with $M_i = 100\,M_\odot$ may have a different fate. At Z = 0.0002 they should enter the PPISN window, ejecting some mass before collapsing to BH. At Z = 0 the outcome is somewhat uncertain. The $M_i = 100\,M_\odot$ model could die as either a failed CCSN or a PPISN, depending on the predicted width of the PPISN strip (see the discussion in Section 4.2.4).

In the event of a failed CCSN, the remnant BH mass of $\simeq 85.5\,M_\odot$ is very close to the estimated primary BH mass of $85^{+21}_{-14}\,M_\odot$ for the binary black hole merger GW190521 (Abbott et al. 2020). I may speculate that primordial very massive stars with $M_i \simeq 100\,M_\odot$ could help us alleviate the black-hole mass gap conundrum (for an overview see Costa et al. 2021). The failed CCSN associated with my ($M_i = 100\,M_\odot$, Z = 0) models provide another possible pathway for the formation of BHs with masses between

$40 - 65\,M_\odot$ and $120\,M_\odot$ (see also Farmer et al. 2020; Sakstein et al. 2020; Croon et al. 2020; Farrell et al. 2021; Costa et al. 2021; Vink et al. 2021; Tanikawa et al. 2021; Farag et al. 2022, for similar conclusions).

Another key process of very massive star evolution is rotation (Yusof et al. 2013; Goswami et al. 2022; Higgins et al. 2022), which will be investigated in a follow-up work. If enough angular momentum was retained in their cores, these very massive stars could produce gamma-ray bursts, known as super-collapsars (Woosley 1993; Yoon et al. 2012).

On the observational side, the James Webb Space Telescope (JWST) will open a new window on Population III stars. Since isolated primordial stars are likely not accessible to JWST, small Population III galaxies and their integrated colors may provide the best opportunities for directly probing the properties of metal-free stars (Zackrisson et al. 2011). Furthermore, thanks to their enhanced sensitivity, future ground-based (Einstein Telescope, Cosmic Explorer) and space-based (LISA, DECIGO) detectors are expected to collect GW events from binary BH mergers in the range of $\approx 10^2 - 10^4\,M_\odot$ up to a redshift ≈ 20 (Saini et al. 2022; Fragione et al. 2022), a regime so far unexplored. In this perspective, theoretical studies on the evolution of primordial very massive stars are critical for contextualizing the upcoming data within an astrophysical picture.

§Chapter 5

Stellar Rotation

This Chapter focuses on stellar rotation, its implementation in the PARSEC code, and on rotating primordial very massive stars. I briefly introduce stellar rotation in Section 5.1. Then, in Section 5.2, I present the key assumptions along with the main aspects of the implementation of stellar rotation in the PARSEC code, following Maeder (2009) and Costa (2019); Costa et al. (2019a,b, which are the works at the base of the implementation of stellar rotation in PARSEC). Finally, in Section 5.3, I introduce rotating primordial very massive stars, which are the subject of the following Chapter.

5.1 Introduction on stellar rotation

The fact that stars rotate is known for more than a hundred years, while the acknowledgment of the Sun's rotation dates back to the XVII century.

Stellar rotation comes from the rotation of molecular clouds and angular momentum conservation. This intrinsic property of the stars plays a decisive role in their evolution, differentiating them from those that do not rotate. Stellar rotation influences the surface physical properties of stars, such as luminosity and effective temperature; moreover, it affects their shape, which departs from the classical spherical symmetry. On top of these, also the internal structure, the chemical composition throughout the star, and the final fate change as a function of rotation.

The root of this deep differentiation between rotating and non-rotating stars resides in various effects (von Zeipel 1924a,b; Kippenhahn and Thomas 1970; Endal and Sofia 1976; Zahn 1992; Meynet and Maeder 1997). Namely, the reduction of effective gravity due to centrifugal effects off of the rotational axis; the equipotential surfaces are not spheres, because gravity and centrifugal forces are not parallel; the radiative flux changes on equipotential surfaces since the dependence of the former on effective gravity; and all the

mixing processes induced by rotation.

5.2 Implementation in the **PARSEC** code

This Section is based on Costa (2019), and the curious reader should refer to that work for further details on the implementation of stellar rotation in PARSEC.

5.2.1 Fundamental assumptions

Rotation is intrinsically a 3D phenomenon; however, there are some methods to implement stellar rotation treatment in 1D stellar evolution codes. There are four main assumptions proposed by Kippenhahn and Thomas (1970): stellar shells are equipotential surfaces, but no longer follow spherical symmetry; the angular velocity Ω has a cylindrical symmetry in each shell; Ω is constant with the colatitude θ (shellular rotation); and the shape of the equipotential shells is computed with the Roche approximation.

Following the four assumptions above, you are forced to adopt a solid body rotation throughout the star. Zahn (1992) proposed to adopt isobars (surfaces with constant pressure) as stellar shells, instead of equipotential surfaces. This followed the fact that the tangential turbulence in a shell is much stronger than the radial one, thus Ω is homogenized within a shell, but not between two different shells (Zahn 1992). Finally, were Meynet and Maeder (1997) to complete the scheme for stellar differential rotation. They did not follow the assumption of cylindrical symmetry given in Kippenhahn and Thomas (1970); therefore, each shell is an isobar with a specific Ω constant with θ.

This scheme keeps the stellar structure equations from Section 2.1, adding two form factors f_P and f_T to account for the effects of rotation. The physical quantities in the new set of stellar structure equations are averages along with isobars, except for the pressure and the angular velocity, which are already constant within a shell.

5.2.2 New equations of stellar structure

The new four structure equations read (for a complete derivation see Chapter 3 in Costa 2019)

$$\frac{\partial r_P}{\partial m_P} = \frac{1}{4\pi r_P^2 \bar{\rho}}, \tag{5.1}$$

$$\frac{\partial P}{\partial m_P} = -\frac{G m_P}{4\pi r_P^4} f_P, \tag{5.2}$$

$$\frac{\partial L_P}{\partial m_P} = \epsilon_{nuc} - \epsilon_\nu + \epsilon_{gr}, \tag{5.3}$$

$$\frac{\partial ln \bar{T}}{\partial m_P} = \frac{G m_P}{4\pi r_P^4} \frac{1}{P} f_P \min\left[\frac{f_T}{f_P}\nabla_{rad}, \nabla_{ad}\right]; \tag{5.4}$$

where

$$\nabla_{rad} = \frac{3}{16\pi acG}\frac{\kappa L_P P}{m_P}, \tag{5.5}$$

$$\nabla_{ad} = \frac{P\delta}{\bar{T}\bar{\rho}c_P}, \tag{5.6}$$

$$f_{\rm P} = \frac{4\pi r_{\rm P}^4}{GmS_{\rm P}} \frac{1}{\langle g_{\rm eff}^{-1}\rangle}, \tag{5.7}$$

$$f_{\rm T} = \left(\frac{4\pi r_{\rm P}^2}{S_{\rm P}}\right)^2 \frac{1}{\langle g_{\rm eff}^{-1}\rangle\langle g_{\rm eff}\rangle}, \tag{5.8}$$

with $\delta = \left(\frac{\partial \ln\rho}{\partial \ln T}\right)_{P,\mu}$ a thermodynamical derivative. Brackets indicate the average over the isobar surface, while bars refer to the average over the volume between two consecutive isobars. The index P indicates the pressure of the considered isobar.

5.2.3 New boundary conditions

As the equations of stellar structure, also the boundary conditions are modified according to the effects of rotation with the form factors f_P and f_T.

The new equations for the envelope (c.f. with Section 2.5) are

$$\frac{\partial ln r_{\rm P}}{\partial ln P} = -\frac{P r_{\rm P}}{\bar{\rho} G m_{\rm P}} \frac{1}{f_{\rm P}}, \tag{5.9}$$

$$\frac{\partial ln m_{\rm P}}{\partial ln P} = -\frac{4\pi r_{\rm P}^4 P}{G m_{\rm P}^2 f_{\rm P}}, \tag{5.10}$$

$$\frac{\partial ln \bar{T}}{\partial ln P} = \min\left[\frac{f_{\rm T}}{f_{\rm P}}\nabla_{\rm rad}, \nabla_{\rm ad}\right]. \tag{5.11}$$

Instead, the boundary conditions for the atmosphere are

$$\frac{d\tau}{dlogP} = \frac{S_{\rm P}\langle g_{\rm eff}^{-1}\rangle}{4\pi r_{\rm P}^2}\kappa P ln10, \tag{5.12}$$

$$T^4(\tau) = \frac{3}{4}T_{\rm eff}^4\left(\frac{S_{\rm P}}{4\pi r_{\rm P}^2} f_{\rm P}\tau + q(\tau)\frac{g}{\langle g_{\rm eff}\rangle}\right), \tag{5.13}$$

with the average gravity $g = \frac{Gm_P}{r_P^2}$.

Regarding the central boundary conditions, they remain as in Section 2.5, since at the center the radius and the angular momentum are zero, while $\left(\frac{d\Omega}{dr}\right)_c = 0$.

5.2.4 Angular momentum transport and chemical mixing

Rotation affects the geometry of the stars but also causes instabilities that redistribute angular momentum and chemical elements throughout their entire structure. This extra mixing is produced by two main instabilities: the meridional circulation (Eddington-Sweet circulation) and the shear instability.

In the former, the thermal differences within a rotating star (von Zeipel 1924b) set in a motion of material from the poles to the equator (or the other way around, Eddington 1929, see also Figure 5.1). On the other hand, the different rotations of two adjacent stellar shells cause shear instability, which in turn mixes the different chemical elements between the stellar layers. This redistribution of angular momentum and chemical elements affects the evolution of rotating stars, for example by bringing new fuel to the burning regions and mixing the nuclear products to the stellar surface.

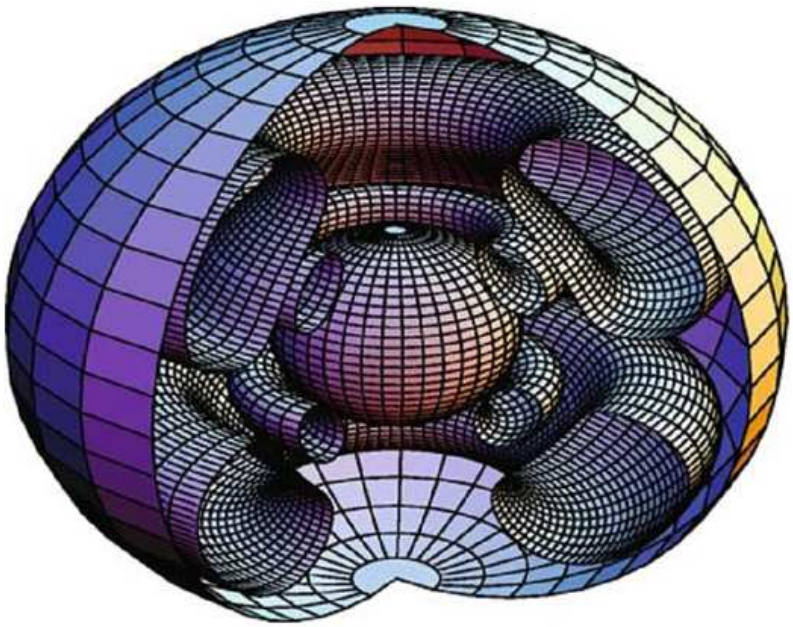

Figure 5.1: Meridional-circulation induced motions in a $20\,M_\odot$ differentially rotating model at the beginning of the MS, $v_{ini} = 300\,km \cdot s^{-1}$. The whirl in the upper-right part near the surface (core) is counterclockwise (clockwise). The convective core is the innermost sphere at the center. Figure from Meynet and Maeder (2002).

In PARSEC, the angular momentum transport is implemented with a pure diffusive scheme and follows the diffusive equation

$$\rho r^2 \frac{dr^2\Omega}{dt} = \frac{\partial}{\partial r}\left(\rho r^4 D \frac{\partial \Omega}{\partial r}\right), \tag{5.14}$$

with D the total diffusion coefficient (see also Figure 5.2), which reads

$$D = D_{\mathrm{Mmlt}} + D_{\mathrm{s.i.}} + D_{\mathrm{m.c.}}, \tag{5.15}$$

where D_{mlt} is the diffusion coefficient in the stellar convective regions. As stated in Section 2.4, in PARSEC is adopted the mixing-length theory (Böhm-Vitense 1958); therefore $D_{mlt} = \frac{1}{3} v l_{mlt}$, where v is the average velocity of the eddies in the convective regions. Then, $D_{s.i.}$ is the diffusion coefficient due to the shear instability (formulation by Talon and Zahn 1997, see Costa (2019) for further details); while $D_{m.c.}$ is the diffusion coefficient due to the meridional circulation (following the approximation by Zahn 1992, see Costa (2019) for further details).

Regarding the extra mixing due to stellar rotation, the total diffusion coefficient is as follows

$$D_{\mathrm{tot}} = D_{mlt} + f_c \cdot (D_{\mathrm{s.i}} + D_{\mathrm{m.c}}), \tag{5.16}$$

where f_c is a parameter expressing the efficiency of the rotational extra mixing. A second parameter f_μ is adopted in PARSEC to control the chemical mixing inhibition due to the molecular weight gradient, which follows the expression

$$\nabla_\mu^{eff} = f_\mu \cdot \nabla_\mu. \tag{5.17}$$

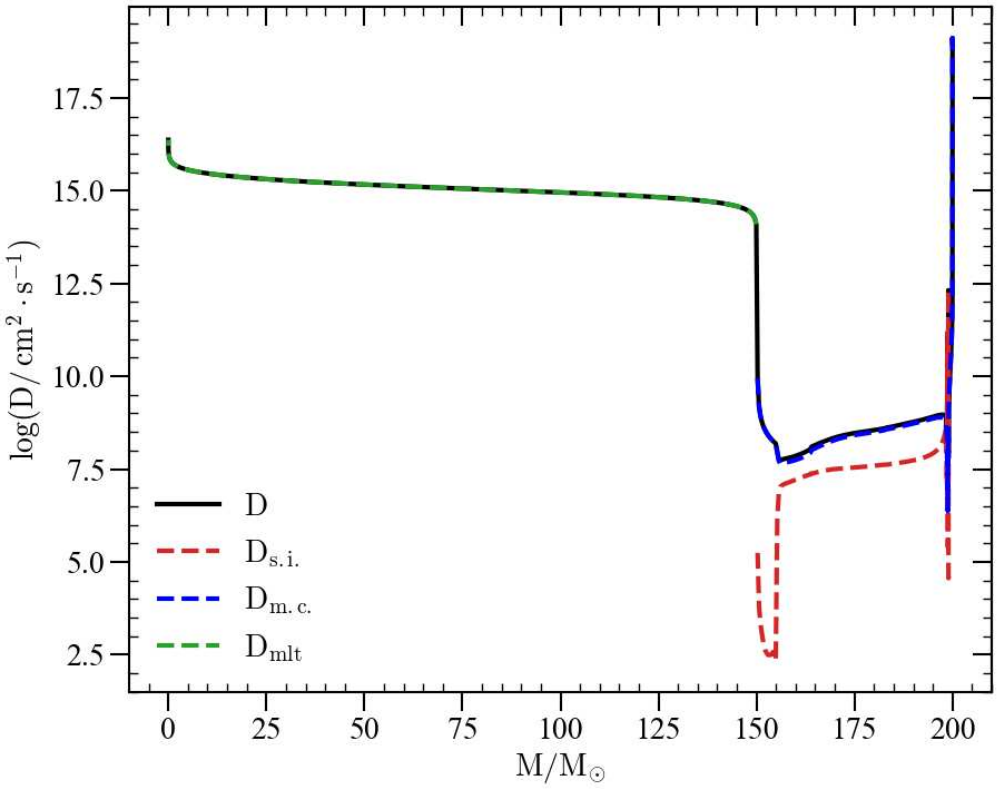

Figure 5.2: Three diffusion coefficients along with the total one within a 200 $M_\odot$, Z = 0 model at the moment of X = 0.5. The black continuous line is the total diffusion coefficient D; the red, blue, and green lines are $D_{s.i.}$, $D_{m.c.}$, and D_{mlt}, respectively.

Both of these parameters have to be calibrated. This is still an open problem and different values for these parameters are adopted in literature (e.g., Table 2 in Costa 2019). Within PARSEC, Costa (2019) calibrated these parameters based on the surface N enrichment ratio in massive stars found by Brott et al. (2011). In this Thesis, I adopt the calibrated values $f_c = 0.17$ and $f_\mu = 0.45$, although some degeneracy is present (see Costa 2019, for further details).

5.2.5 Mass loss with rotation

Rotation and mass loss interplay is particularly important given the focus of the present work. Due to the lower effective gravity, mass loss is enhanced in rotating stars and it plays also a crucial role in removing angular momentum during the different evolutionary phases.

In PARSEC is adopted the prescription by Heger et al. (2000), which accounts for mass loss enchantment as follows

$$\dot{M}(\omega_S) = \dot{M}(\omega_S = 0)\Big(\frac{1}{1 - v_S/v_{S,crit}}\Big)^{\xi}, \qquad \xi = 0.43, \tag{5.18}$$

with ω_S the surface rotation rate and $\dot{M}(\omega_S = 0)$ the mass loss rate for the not-rotating case. The surface tangential velocity is v_S, while the surface breakup velocity is

$$v^2_{S,crit} = \frac{GM}{r_{phot}}(1 - \Gamma_e), \tag{5.19}$$

where M is the total mass of the star, r_phot the photospheric radius, and Γ_e the Eddington factor. Following Georgy et al. (2013), also mechanical mass loss is implemented in the code. This occurs when the star reaches the critical rotation and therefore the external layers of the star are lost due to the equatorial gravity being balanced by centrifugal forces. Mechanical mass loss is treated by computing the angular momentum excess in super-critical shells, which is the difference between their angular momentum and the critical one. Then, from this excess, the code calculates the mass to remove so that the star does not rotate at the critical velocity. At each timestep, the maximum between the mechanical and the rotationally enhanced wind mass loss is applied.

5.3 Rotating Primordial Very Massive Stars

The first stars (Population III) that lit up in our Universe might have been far more massive than those forming nowadays, with an initial mass function peaking at $\simeq 100\,M_\odot$ (Bromm et al. 1999; Abel et al. 2002). The reason is the absence of metals, which are the most efficient coolants within molecular clouds during star formation. In Chapter 4, I investigated the effect of pulsation-driven mass loss (see the prescription in Nakauchi et al. 2020) on the evolution and final fate of primordial VMSs. I found that pulsation-driven and radiation-driven mass loss dominates during different evolutionary phases. In Chapter 4 , the most massive stars can eject several solar masses of material already during the MS due to radial pulsations. This is in contrast with the modest mass loss expected from radiation-driven winds at these metallicities. I find that almost all models experience pair-creation instability during the last phases of the evolution after the ignition of carbon, neon, or oxygen depending on the mass of the star. Models with $M_i = 100\,M_\odot$ and $Z = 0$ are somewhat uncertain and may avoid pair instability. Our stars with $300 \leq M_i/M_\odot \leq 1000$ should directly collapse to a BH (Bond et al. 1984; Farmer et al. 2020), while models with $M_i = 150, 200\,M_\odot$ should produce PISNæ , leaving no remnant (Fowler and Hoyle 1964; Barkat et al. 1967; Rakavy and Shaviv 1967; Fraley 1968; Heger and Woosley 2002; Heger et al. 2003; Takahashi et al. 2018; Takahashi 2018; Woosley and Heger 2021; Farag et al. 2022; Costa et al. 2023b). Models with $M_i = 100\,M_\odot$ and $Z = 0.0002$ should enter into the PPISN regime (Woosley et al. 2002; Chen et al. 2014; Yoshida et al. 2016; Woosley 2017; Farmer et al. 2019; Woosley and Heger 2021; Farag et al. 2022). Instead, those with the same mass and $Z = 0$ could end their evolution either with a fCCSN or a PPISN. In the former case, these models could provide a new formation pathway for BHs, potentially helping to alleviate the black-hole mass gap puzzle (see also Farmer et al. 2020; Sakstein et al. 2020; Croon et al. 2020; Farrell et al. 2021; Costa et al. 2021; Vink et al. 2021; Tanikawa et al. 2021; Farag et al. 2022, for different formation scenarios).

In Chapter 4 , I did not consider stellar rotation, which is one of the most influential phenomena in the evolution of massive and very massive stars (Heger et al. 2000; Meynet and Maeder 2000; Brott et al. 2011; Ekström et al. 2012; Paxton et al. 2013; Yusof et al.

2013; Limongi and Chieffi 2018; Goswami et al. 2021, 2022; Higgins et al. 2022; Martinet et al. 2023). Rotation changes the gravity of the star and thus modifies the stellar geometry from the usual spherical symmetry also affecting the surface temperature (e.g. Costa et al. 2019a,b, and references therein). The fact that the star is rotating implies different kinds of turbulent mixing, e.g. meridional circulation and shear instability. These processes increase the mixing of chemical elements within the star, affecting the lifetimes of the main nuclear burning phases as well as the chemical composition at the star's surface (Maeder 2009, and references therein). Turbulence caused by rotation transports angular momentum from the stellar core to the envelope (Heger et al. 2000), where it is removed by stellar winds. Mass loss is also enhanced by rotation due to lower effective gravity, which is caused by centrifugal forces (Heger et al. 2000; Georgy et al. 2011; Costa et al. 2019a, and references therein).

While the effect of rotation on mass loss in VMSs has been the subject of several studies (e.g. Meynet and Maeder 2000; Ekström et al. 2012; Yoon et al. 2012, 2015; Murphy et al. 2021; Martinet et al. 2023), its impact in combination with pulsation-induced mass loss has never been examined. In light of the results of Chapter 4, this topic clearly deserves to be investigated. I do so using the PARSEC code (Bressan et al. 2012; Costa et al. 2019a,b; Nguyen et al. 2022) to follow the evolution of a set of VMSs until the occurrence of pair instability, in line with our previous work.

Rotation can also heavily affect the final fate of massive and very massive stars and it is a necessary condition to produce successful GRB events (Woosley 1993; Woosley and Heger 2006, 2012; Yoon et al. 2006, 2012, 2015). The collapsar model (Woosley 1993) is the most widely accepted theory for the formation of long GRBs, in which an accretion disk forms during the collapse of a massive star, powering the jets that produce the GRB event. The accretion disk can form only if the infalling material has enough angular momentum to avoid direct accretion onto the BH (Woosley 1993). The propagation of the jet through the progenitor is a major issue for massive stars with extended envelopes, preventing the production of a successful gamma-ray burst (GRB) event. The reason is that the crossing timescale for the jet to reach the surface of the star can be longer than the accretion timescale by more than 3 orders of magnitude. In this case, the jet is not powerful enough to break out from the star and produce a successful GRB (Yoon et al. 2006, 2012; Woosley and Heger 2012; Yoon et al. 2015). This is why when considering Pop III stars, Yoon et al. (2012) proposed the chemically-homogeneous evolution as the main channel for the star to retain enough angular momentum within its core and at the same time to avoid the redward evolution in the HR diagram. In this way, the star does not retain a very extended envelope and this facilitates the jet propagation. In this work, I investigate models of VMS that should experience PI but with lower masses compared to Yoon et al. (2015) to have less extended envelopes. I find another possible pathway for the evolution of successful GRB progenitors. The absence of the stellar envelope due to pulsational-pair instability mass loss eases the jet propagation through the star. This decreases enormously the crossing timescale for the jet to reach the stellar surface, thus producing successful GRB events.

§Chapter 6

Rotating Very Massive Star Evolution

This chapter is based on:
G. Volpato, P. Marigo, G. Costa, A. Bressan, M. Trabucchi, L. Girardi, and Francesco Addari;
"A Study of Primordial Very Massive Star Evolution II: Stellar Rotation and Gamma-Ray Burst Progenitors";
ApJ, 961(1):89; Jan. 2024; doi: 10.3847/1538-4357/ad1185.

In this Chapter, I present new evolutionary models of rotating primordial very massive stars, with initial mass from $100\,M_\odot$ to $200\,M_\odot$, for two values of the initial metallicity $Z = 0$ and $Z = 0.0002$. For the first time in this mass range, I consider stellar rotation and pulsation-driven mass loss, along with radiative winds. The models evolve from the ZAMS, until the onset of pair instability. I discuss the main properties of the models during their evolution and then focus on the final fate and the possible progenitors of jet-driven events.

This Chapter is organized as follows. In Section 6.1 I briefly describe the PARSEC code and its major ingredients. In Section 6.2 I present the rotating stellar evolution models computed with mass-loss recipes that account for both radiation-driven and pulsation-driven mass loss. I provide an overview of evolutionary properties, with emphasis on core evolution, dredge-up episodes, internal structure, surface elemental abundances, chemical ejecta, final evolution outcomes, and associated compact remnants. In the last part of Section 6.2, I focus on the possible Gamma-Ray Burst and jet-driven supernova (SN) progenitors. Finally, Section 6.3 closes the paper with some concluding remarks and

future perspectives.

6.1 Stellar evolution calculations

I compute stellar evolution calculations with the PARSEC code (Bressan et al. 2012) in its version 2.0 (Costa et al. 2019a,b, 2021; Nguyen et al. 2022, and reference therein). The input physics and the code parameters are as described in Chapter 2, whereas the details of the implementation of rotation in the PARSEC code can be found in Costa et al. (2019a,b). I use scaled-solar abundances (Caffau et al. 2011), where the initial solar metallicity follows the calibration in Bressan et al. (2012), $Z_{\rm initial,\odot} = 0.01774$. Here, I briefly summarize the main aspects of the PARSEC code that concern the evolution of massive stars, and, in particular, the mass loss prescriptions adopted in this work. For the standard mass loss prescription ($\dot{M}_{\rm rdw}$, for further details see Section 2.3), I adopt the formulation by Vink et al. (2000, 2001) and the mass loss rates predicted by de Jager et al. (1988) for stars with effective temperature higher and lower than 10000 K, respectively. The metallicity dependence is $\dot{M} \propto (Z/Z_{\rm initial,\odot})^{0.85}$, where I use the initial metallicity as a proxy for the iron content[1] (which remains constant along the evolution). I also consider the enhancement of mass loss due to the proximity of the Eddington factor to one (Gräfener and Hamann 2008; Vink et al. 2011). In this case, I use the same scheme as in Chen et al. (2015), with the following details $\dot{M} \propto (Z/Z_{\rm initial,\odot})^{\alpha}$, where $\alpha = 2.45 - 2.4\Gamma_{\rm e}$, with $\Gamma_{\rm e}$ the Eddington factor and α between 0 and 0.85. In each evolutionary stage, I take the maximum mass loss rate between Vink et al. (2000, 2001) or de Jager et al. (1988) and Vink et al. (2011), which accounts for the Eddington factor dependence. For Wolf-Rayet stars with $X < 0.3$ and $\log(T_{\rm eff}) > 4$, I use the mass loss recipe from Sander et al. (2019) with the metallicity dependence proposed by Costa et al. (2021).

For pulsation-driven mass loss ($\dot{M}_{\rm pdw}$, see Section 3.2), I use the analytical expressions provided by Nakauchi et al. (2020)

$$\log\left(\frac{\dot{M}_{\rm pdw}}{M_\odot\,{\rm yr}^{-1}}\right) = \alpha_1 \log\left(\frac{M}{10^3\,M_\odot}\right) - \alpha_2 - \beta_1\,[\log(T_{\rm eff}) - \beta_2]^{\gamma} \tag{6.1}$$

$$\log\left(\frac{\dot{M}_{\rm pdw}}{M_\odot\,{\rm yr}^{-1}}\right) = -2.88 + \log\left(\frac{M}{10^3\,M_\odot}\right) - 15.6\,[\log(T_{\rm eff}) - 3.7]\ , \tag{6.2}$$

where α_1, α_2, β_1, β_2, and γ are coefficients that depend on the initial metallicity of the model (see Nakauchi et al. 2020, for more details). Finally, the last mass loss prescription is $\dot{M}_{\rm max}$ (see Section 4.1), which takes the maximum between $\dot{M}_{\rm rdw}$ and $\dot{M}_{\rm pdw}$ at each timestep during the evolution of the models.

Concerning the interplay between mass loss and stellar rotation (see also Section 5.2.5), I use the prescription by Heger et al. (2000), which reads

$$\dot{M}(\omega) = \dot{M}(\omega = 0)\left(\frac{1}{1 - v/v_{\rm crit}}\right)^{\xi},\ \text{with}\ \xi = 0.43, \tag{6.3}$$

[1] when using Vink et al. (2000, 2001) prescription, the initial stellar iron content has to be rescaled to the initial solar value according to our calibration

where $\dot{M}(\omega = 0)$ is the mass loss rate in the non-rotating case. Then, v is the surface tangential stellar velocity, while v_{crit} is the break-up velocity defined as

$$v_{crit}^2 = \frac{Gm}{r}(1 - \Gamma_e). \tag{6.4}$$

I take into account also the mechanical mass loss when the star reaches the critical rotation (Georgy et al. 2013). It is worth noticing that there are different prescriptions for the treatment of stellar rotation (e.g. Maeder and Meynet 2000), and this subject is still under investigation. Major uncertainties in stellar rotation are tied to different aspects. For instance, stellar rotation is inextricably linked to magnetic field generation (e.g. Braithwaite and Spruit 2017; Brun and Browning 2017). The interaction between rotation and magnetic fields is not completely understood, despite it influences stellar activity, which affects processes such as star spots, flares, and the stellar wind. Furthermore, rotation influences mass and angular momentum loss from stars, thus affecting their evolution. Predicting the rate and pattern of mass loss due to rotation-induced instabilities is still a source of uncertainties in evolutionary models.

I adopt the mixing-length theory by Böhm-Vitense (1958), with a mixing-length parameter $\alpha_{mlt} = 1.74$. I use the Schwarzschild criterion to define the border of the convective regions, while for core overshooting I adopt the ballistic approximation (Bressan et al. 1981). In this latter, the core overshooting parameter ($\lambda_{ov} = 0.4$) times the pressure scale height corresponds to the mean free path of the eddies *across* the border of the convective region. I also account for overshooting at the base of the convective envelope below the formal Schwarzschild border (Alongi et al. 1991; Bressan et al. 2012; Nguyen et al. 2022). Recent calibration of the red giant branch bump luminosity in a large sample of Globular Clusters with metallicity $-2 < [M/H] < 0$ using updated α-enhanced PARSEC models (Fu et al. 2018) suggests using an envelope overshooting parameter Λ_{env} between 0.5 and 0.7, with the latter value being more appropriate in more metal-poor systems. Similar, if not greater, values are required to reproduce blue loops in star clusters and low metallicity dwarf irregular galaxies (Alongi et al. 1991; Bressan et al. 2012; Tang et al. 2014). In the present calculations, I use $\Lambda_{env} = 0.7$.

To inhibit density inversion in the inefficient convective regions of the stellar envelope, I follow the temperature gradient limitation described in Chen et al. (2015). By imposing $\nabla_T \leq \nabla_{T_{max}} = \frac{1-\chi_\mu \nabla_\mu}{\chi_T}$, convection becomes more efficient preventing the numerical instabilities caused by density inversion.

As in Chapter 4, I consider two different initial chemical compositions (Z = 0, Y = 0.2485) and (Z = 0.0002, Y = 0.24885), with Z and Y the initial abundances in mass fraction of metals and helium, respectively. I compute stellar evolution models with initial mass $M_i = 100, 150, 200\,M_\odot$ and *initial* rotation rate $\omega = 0.0, 0.2, 0.3, 0.4, 0.5$; where $\omega = \Omega_i/\Omega_{crit}$ with Ω_i the initial angular velocity and Ω_{crit} the critical angular velocity. For each combination of (M_i, Z, ω) I compute two stellar models adopting two different mass loss recipes, namely $\dot{M}_{rdw}$ and $\dot{M}_{max}$. I found models to encounter progressively higher numerical difficulties in the computation towards the highest values of mass, rotation velocity, and metallicity in the explored range. In particular, two models out of 60 could not be brought to convergence (the models with $M_i = 150\,M_\odot$ and $M_i = 200\,M_\odot$, having Z = 0.0002, $\omega_i = 0.5$ and computed with the $\dot{M}_{rdw}$ prescription) so I exclude them from the following discussion.

I note that the calculations of Nakauchi et al. (2020) are based on non-rotating models, while in the present study, the interplay between rotation and stellar pulsation should be taken into account. However, I found the time scale of pulsation to be always much shorter than the rotation period in all my models, indicating that the interaction between the two processes can be safely neglected (see Appendix 6.C for further details).

I follow the evolution of my models from the ZAMS until the onset of pair-creation instability (see Section 4.1.2). This occurs after the ignition of carbon, neon, and oxygen in the stellar core depending on the initial mass, metallicity, rotation, and mass-loss prescription adopted for the models (see Tables 6.1 and 6.2).

6.2 Results

6.2.1 General Properties of the Stellar Evolutionary Tracks

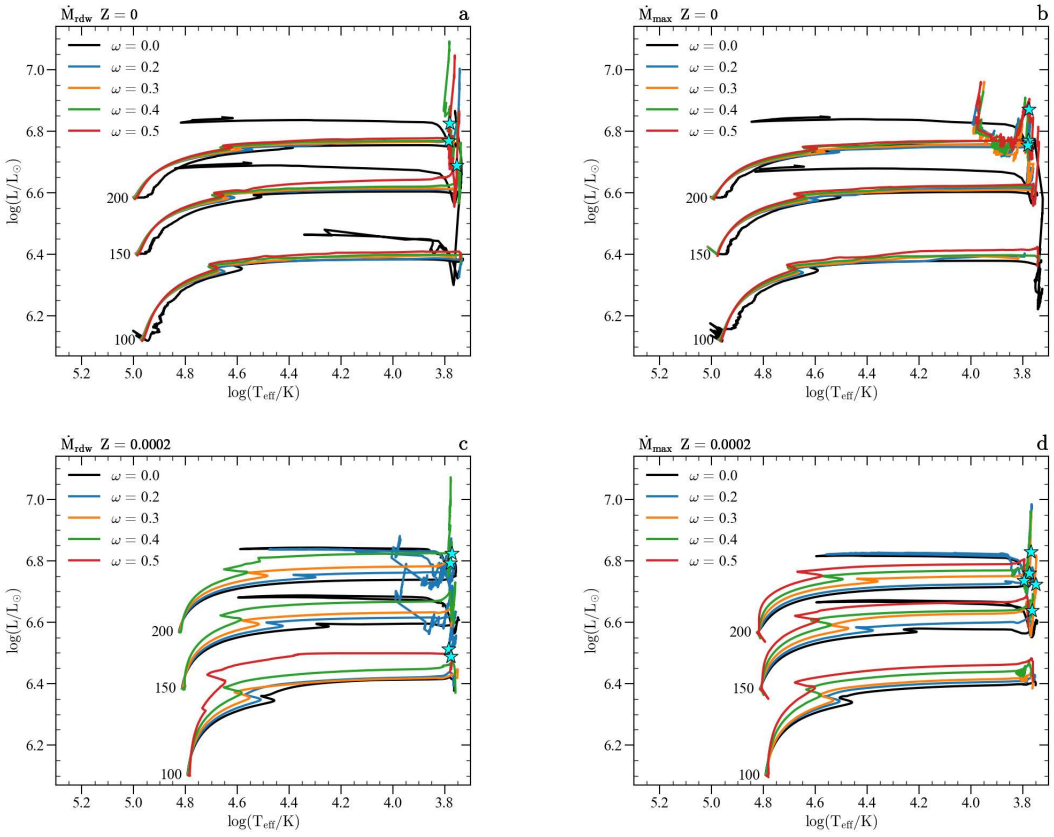

Figure 6.1: H-R diagrams of the twenty sets of tracks computed in this work. Different initial rotation rates are color-coded as labeled. Panels *a,b* and *c,d* refer to Z = 0 and Z = 0.0002, respectively. *Panels a,c*: tracks calculated with the standard PARSEC mass-loss prescription for radiation-driven winds. *Panels b,d*: tracks computed considering also the pulsation-driven mass loss. Cyan starred symbols indicate where the stellar models become Wolf-Rayet manqué stars (X < 0.3). I plot the value of initial mass (in $M_\odot$) for all tracks.

Table 6.1: Most Relevant Properties of Models Computed with Z = 0.0002, $\dot{M}_{rdw}$ and $\dot{M}_{max}$

M_i [$M_\odot$]	τ_{MS} [Myr]	τ_{cHeB} [Myr]	$f_{H\,puls}$	$f_{He\,puls}$	Blue Loop	DUP	M_{He} [$M_\odot$]	M_{CO} [$M_\odot$]	M_f [$M_\odot$]	X_{core} Onset PI	L_ν/L_{rad} [$\log_{10}$]	Fate	remnant	M_{BH} [$M_\odot$]
(1)	(2)	(3)	(4)	(5)	(6)	(7)	(8)	(9)	(10)	(11)	(12)	(13)	(14)	(15)
						$\dot{M}_{rdw}$ ω = 0.0								
100	2.83	0.25	0.29	0.57	×	✓	53.8	47.6	94.3	0.865 O	3.1	PPISN	BH	40.9
150	2.45	0.24	0.45	0.32	✓	✓	79.5	71.8	146.4	0.080 Ne	3.2	PISN	×	-
200	2.25	0.23	0.50	0.33	✓	✓	110.3	100.7	193.9	0.003 C	3.2	PISN	×	-
						ω = 0.2								
100	2.87	0.26	0.28	0.96	×	×	52.0	46.0	93.4	0.853 O	3.1	PPISN	BH	39.8
150	2.48	0.25	0.45	0.97	×	✓	45.1	38.8	143.0	0.131 O	2.4	PPISN	BH	40.09
												DBH[e]	BH	128.7
200	2.28	0.24	0.49	0.76	✓	✓	51.9	46.0	191.5	0.090 O	2.4	PPISN	BH	48.5
												DBH[e]	BH	172.4
						ω = 0.3								
100	2.92	0.27	0.27	0.97	×	×	51.7	45.3	93.1	0.848 O	3.1	PPISN	BH	39.5
150	2.51	0.25	0.46	0.97	×	×	80.9	71.8	142.8	0.061 Ne	3.2	PISN	×	-
200	2.30	0.23	0.51	0.98	×	×	108.9	98.1	191.1	0.001 C	3.2	PISN	×	-
						ω = 0.4								
100	2.98	0.27	0.26	0.95	×	✓	51.5	44.5	92.9	0.877 O	3.1	PPISN	BH	39.4
150	2.56	0.24	0.50	0.98	×	✓	77.6	69.6	142.3	0.020 Ne	3.1	PISN	×	-
200	2.33	0.23	0.53	0.90	×	✓	95.2	95.0	189.4	0.022 Ne	2.7	PISN	×	-
												DBH[e]	BH	170.5
						ω = 0.5								
100	3.09	0.27	0.22	0.53	×	✓	53.2	45.8	95.0	0.879 O	3.1	PPISN	BH	40.7
												PISN[e]	×	-
						$\dot{M}_{max}$ ω = 0.0								
100	2.84	0.26	0.28	0.95	×	✓	53.1	46.9	92.7	0.859 O	3.1	PPISN	BH	40.4
150	2.47	0.24	0.44	0.38	✓	✓	77.0	69.3	139.7	0.055 Ne	3.2	PISN	×	-
200	2.29	0.23	0.49	0.36	✓	✓	105.7	96.2	180.2	0.002 C	3.2	PISN	×	-
						ω = 0.2								
100	2.88	0.27	0.28	0.97	×	×	52.0	46.0	92.2	0.857 O	3.1	PPISN	BH	39.6
150	2.50	0.24	0.46	0.98	×	×	81.0	74.1	136.7	0.086 Ne	3.3	PISN	×	-
200	2.31	0.23	0.52	0.49	✓	✓	91.2	91.2	176.6	0.021 Ne	2.8	PISN	×	-
												DBH[e]	BH	158.9
						ω = 0.3								
100	2.91	0.27	0.25	0.97	×	×	49.6	43.6	92.1	0.768 O	3.1	PPISN	BH	38.2
150	2.53	0.24	0.50	0.99	×	✓	71.4	67.6	135.7	0.883 O	2.8	PISN	×	-
												DBH[e]	BH	122.1
200	2.34	0.23	0.58	0.98	×	✓	101.1	99.1	174.3	0.117 Ne	2.9	PISN	×	-
												DBH[e]	BH	156.9
						ω = 0.4								
100	2.99	0.27	0.28	0.97	×	×	51.1	44.4	91.8	0.880 O	3.1	PPISN	BH	39.1
150	2.58	0.25	0.55	0.98	×	✓	77.1	69.0	134.6	0.009 Ne	3.1	PISN	×	-
												DBH[e]**	BH	121.1
200	2.37	0.24	0.65	0.98	×	✓	93.8	89.5	171.3	0.101 Ne	2.9	PISN	×	-
												DBH[e]	BH	154.2
						ω = 0.5								
100	3.06	0.27	0.06	0.94	×	×	54.0	46.5	91.7	0.878 O	3.1	PPISN	BH	40.8
150	2.62	0.25	0.63	0.96	×	✓	81.7	71.5	132.2	0.029 Ne	3.2	PISN	×	-
200	2.41	0.24	0.75	0.95	×	×	114.6	101.7	163.1	0.001 C	3.3	PISN	×	-

Note—The table entries are as follows: (1) star's initial mass; (2) MS lifetime; (3) cHeB lifetime; (4) and (5) fractions of MS and cHeB lifetimes in which the star is unstable to radial pulsation; (6) and (7) occurrence of blue loop and dredge-up episode; (8) final He core mass; (9) final C-O core mass; (10) final mass of the star at the onset of dynamical instability; (11) central fuel abundance of ongoing nuclear burning at the onset of dynamical instability; (12) neutrino luminosity to radiative luminosity ratio when $T_c = 10^9$ K; (13) and (14) final fate and associated outcome (BH or complete disruption), and (15) BH mass.

** assuming an error of 1% on upper limit for PISN in fit formula by Mapelli et al. (2020);
(e) considering $M_{He} = M_f$, so $M_{BH} = 0.9 \cdot M_f$

Table 6.2: Most Relevant Properties of Models Computed with Z = 0, $\dot{M}_{rdw}$ and $\dot{M}_{max}$

M_i [$M_\odot$]	τ_{MS} [Myr]	τ_{cHeB} [Myr]	$f_{H\,puls}$	$f_{He\,puls}$	Blue Loop	DUP	M_{He} [$M_\odot$]	M_{CO} [$M_\odot$]	M_f [$M_\odot$]	X_{core} Onset PI	L_ν/L_{rad} [$\log_{10}$]	Fate	remnant	M_{BH} [$M_\odot$]
(1)	(2)	(3)	(4)	(5)	(6)	(7)	(8)	(9)	(10)	(11)	(12)	(13)	(14)	(15)
$\dot{M}_{rdw}$ ω = 0.0														
100	2.54	0.25	0.07	0.51	✓	✓	41.8	38.4	99.9	0.511 O	2.7	fCCSN[a]	BH	89.9
												PPISN[b]	BH	34.2
150	2.33	0.23	0.30	0.36	✓	✓	74.4	67.7	149.9	0.011 Ne	3.1	PISN	×	-
200	2.16	0.22	0.27	0.35	✓	✓	110.4	103.8	199.9	0.001 C	3.2	PISN	×	-
ω = 0.2														
100	2.65	0.25	0.46	0.11	×	✓	50.6	45.4	99.9	0.858 O	3.2	PPISN	BH	39.5
150	2.30	0.23	0.51	0.11	×	×	78.7	70.6	149.9	0.049 Ne	3.2	PISN	×	-
200	2.12	0.28	0.53	0.46	×	✓	100.9	97.8	199.9	0.120 Ne	2.9	PISN	×	-
ω = 0.3														
100	2.68	0.25	0.45	0.0	×	×	50.7	44.6	99.9	0.739 O	3.1	PPISN	BH	39.6
150	2.31	0.24	0.51	0.07	×	×	79.3	70.7	149.9	0.042 Ne	3.2	PISN	×	-
200	2.13	0.28	0.52	0.40	×	×	108.3	98.1	199.9	0.002 C	3.3	PISN	×	-
ω = 0.4														
100	2.70	0.26	0.44	0.18	×	✓	50.3	43.7	99.9	0.775 O	3.1	PPISN	BH	39.4
150	2.34	0.24	0.50	0.36	×	✓	68.6	67.1	149.9	0.883 O	2.7	PISN	×	-
200	2.15	0.23	0.51	0.37	×	✓	89.6	89.6	199.9	0.042 Ne	2.7	PISN	×	-
												DBH[e]	BH	180.0
ω = 0.5														
100	2.75	0.26	0.43	0.26	×	✓	49.7	43.4	99.9	0.708 O	3.1	PPISN	BH	39.0
150	2.36	0.25	0.48	0.84	×	✓	64.3	61.6	149.9	0.882 O	2.7	PPISN[d]	BH	35.8
												PISN[c]	×	-
												DBH[e]	BH	135.0
200	2.17	0.24	0.50	0.45	×	✓	85.0	83.8	199.9	0.047 Ne	2.7	PISN	×	-
												DBH[e]	BH	180.0
$\dot{M}_{max}$ ω = 0.0														
100	2.59	0.26	0.17	0.51	×	✓	37.1	34.3	95.0	0.412 O	2.8	fCCSN[a]	BH	85.5
												PPISN[b]	BH	30.9
150	2.33	0.23	0.32	0.36	✓	✓	77.5	72.6	147.7	0.019 Ne	3.1	PISN	×	-
200	2.15	0.22	0.30	0.35	✓	✓	102.9	95.1	197.6	0.001 C	3.2	PISN	×	-
ω = 0.2														
100	2.66	0.25	0.46	0.004	×	×	50.2	44.9	99.2	0.699 O	3.1	PPISN	BH	39.2
150	2.31	0.24	0.51	0.18	×	×	78.6	71.4	147.3	0.062 Ne	3.2	PISN	×	-
200	2.13	0.24	0.52	0.70	×	✓	48.7	48.7	192.0	0.834 O	2.5	PPISN	BH	46.7
												DBH[e]	BH	172.8
ω = 0.3														
100	2.68	0.26	0.45	0.00	×	×	50.7	44.7	99.2	0.701 O	3.1	PPISN	BH	39.5
150	2.33	0.24	0.51	0.11	×	×	78.6	70.0	147.6	0.024 Ne	3.2	PISN	×	-
200	2.14	0.24	0.53	0.51	×	✓	40.6	40.1	193.2	0.443 O	2.3	fCCSN[a]	BH	173.9
												PPISN[b]	BH	41.8
												DBH[e]	BH	173.9
ω = 0.4														
100	2.71	0.26	0.45	0.08	×	×	50.7	44.2	99.0	0.818 O	3.1	PPISN	BH	39.5
150	2.35	0.24	0.51	0.22	×	×	78.8	69.6	146.9	0.035 Ne	3.1	PISN	×	-
200	2.16	0.24	0.53	0.81	×	✓	41.7	41.5	192.2	0.285 O	2.3	fCCSN[a]	BH	173.0
												PPISN[b]	BH	42.4
												DBH[e]	BH	173.0
ω = 0.5														
100	2.76	0.26	0.43	0.41	×	✓	49.0	42.5	97.1	0.723 O	3.1	PPISN	BH	38.3
150	2.38	0.24	0.50	0.37	×	✓	73.1	68.7	146.0	0.884 O	2.9	PISN	×	-
200	2.18	0.23	0.52	0.34	×	✓	52.3	51.4	194.1	0.295 O	2.3	PPISN	BH	48.9
												DBH[e]	BH	174.7

Note—Table entries as in Table 6.1.
[a] failed CCSN. Following Farmer et al. (2019) I set the lower limit of M_{He} for PPISN at 45 $M_\odot$;
[b] following Woosley (2017) I set the lower limit of M_{He} for PPISN at 34 $M_\odot$;
[c] following Woosley (2017) I set the lower limit of M_{He} for PISN at 64 $M_\odot$;
[d] I set the lower limit of M_{He} for PISN at 65.24 $M_\odot$, which is the M_{He} of the T140D model in Woosley (2017)

In Table 6.1 and 6.2 I summarize the main properties that highlight the evolution and final outcome of the models.

Figure 6.1 presents the evolution of all models in the HRD, where we can see that there is a positive correlation between the models' luminosity and their initial rotation velocity, ω. This is most evident for models computed with $Z = 0.0002$, while in the case of $Z = 0$, the evolutionary tracks run almost superimposed except for the non-rotating ones. This behavior can be explained by the helium enrichment at the surface during MS, which forces both luminosity and effective temperature to increase. In turn, this helium enrichment is caused by two factors. First, the enhancement of the convective core between rotating and non-rotating models increases with metallicity (Groh et al. 2019). Second, at $Z = 0.0002$, the region above the convective core experiences greater rotational mixing as the rotation rate increases, compared to the $Z = 0$ models at the same rotation rates.

Another effect of rotation is to reduce or even quench the blue loops during the cHeB phase. We can see that in all panels of Figure 6.1, there is at least one non-rotating star that evolves toward higher effective temperatures. With the addition of rotation, this is not the case anymore. Models with $Z = 0$ and $\omega > 0$ evolve after the MS toward the red part of the HRD; while for $Z = 0.0002$ there are two models with $\omega = 0.2$ that perform a blue loop, but in the case of $\omega > 0.2$ no model evolves back to higher effective temperatures.

After the MS phase, due to rotational mixing and the occurrence of DUP episodes, 16 stellar models reach a surface hydrogen abundance $X < 0.3$ (starred symbols in Figure 6.1). When massive stars evolve into red supergiants, the convective envelope inflates and cools, while at low densities opacity is dominated by electron scattering. These lead to increasing atmospheric opacity and favor the development of convection in progressively deeper layers of the star, causing a DUP episode. It is worth noticing that the efficiency of the DUP depends on the envelope undershooting parameter as shown in Costa et al. (2021). According to our definition (see Section 2.3), these 16 stars exhibit a surface chemical composition similar to Wolf-Rayet (WR) stars. Still, they are not hot and spend most of their evolution with a low effective temperature in the red part of the HRD. For this reason, I refer to this kind of stars as WR-manqué (WRm) stars (note that the mass loss recipe adopted for these stars is that by de Jager et al. 1988). This drastic change in the surface chemical composition occurs too late to have a great impact on the models' effective temperature evolution. If the hydrogen surface abundance were to decrease below $\sim 20\%$ during MS (due to high rotation mixing), then the models would have followed the so-called chemically homogeneous evolution. In this case, they would have evolved towards higher effective temperatures, completely avoiding the red-supergiant phase (Yoon et al. 2012; Woosley and Heger 2006). I do not find any occurrence of chemically homogeneous evolution in my models. Among these 16 tracks, 6 stellar models reach a total amount of hydrogen between 0.26% and 0.1% of their total mass. Section 6.2.3 examines the impact of dredge-up and rotation on surface abundances and chemical ejecta, especially for these extreme WRm stellar models.

6.2.2 Internal Structure

Figure 6.2 shows the Kippenhahn diagrams of four different stellar models. They have the same initial mass $M_i = 200\,M_\odot$, but different metallicities, rotational velocities, and

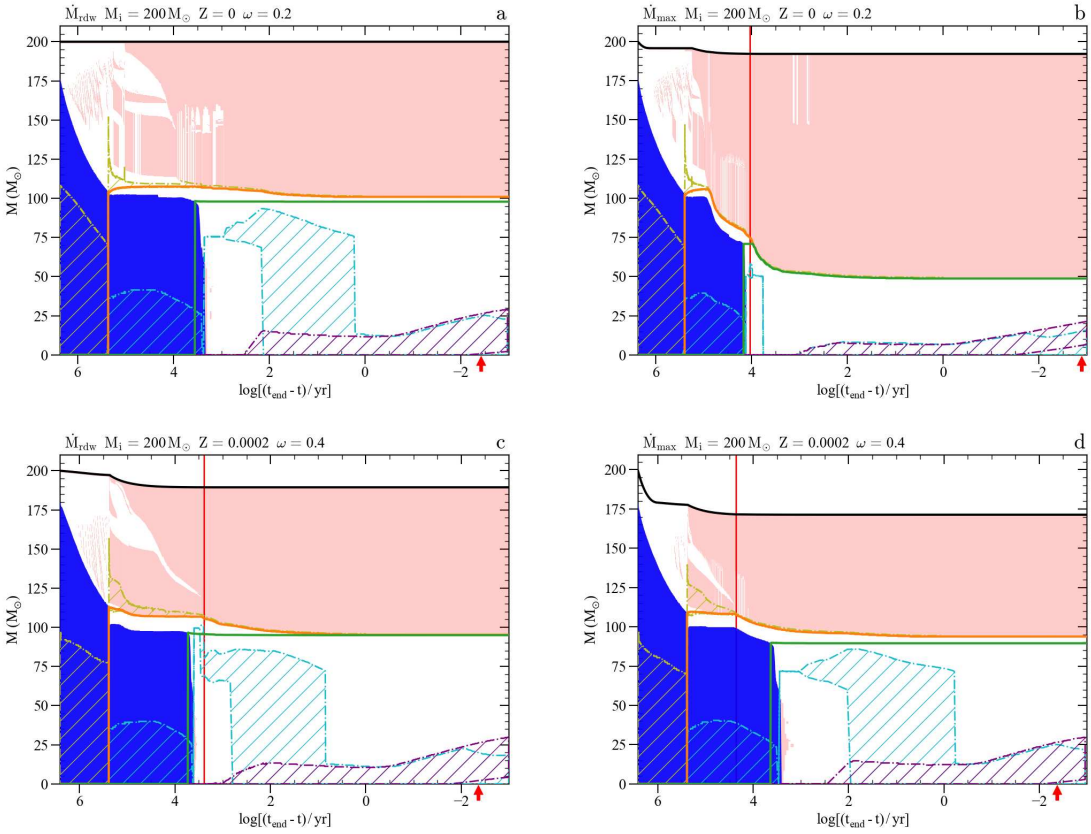

Figure 6.2: Kippenhahn diagrams of four selected models. The horizontal axis shows the age of the models as logarithm of time (in yr) until the end of computations. The blue regions correspond to the star's convective core, the pink area represents the convective envelope, semi-convective zones at the boundary of the helium convective core, and convective shells. The yellow, cyan, and purple hatch regions show the hydrogen, helium, and carbon-burning core/shells, respectively. The black continuous line indicates the total mass of the star, the orange one represents the helium core, and the green one corresponds to the carbon-oxygen core. The red arrow marks the time when the star enters the unstable region with $\langle\Gamma_1\rangle = 4/3 + 0.01$; while the red vertical line shows when the star becomes a WRm with $X < 0.3$. *Panels a,c*: models computed with the standard PARSEC mass-loss prescription for radiation-driven winds. *Panels b,d*: models that account also for pulsation-driven winds.

mass loss prescriptions. At the beginning of the MS, all these stars have a convective core equal to almost 90% of their total mass. This is because these models have a very large initial mass, and also rotation increases the extent of their convective cores. For example, comparing the models in panels a and c, we can notice that the star in this latter panel has a slightly bigger convective core, due to its higher initial rotational velocity. Then, the model in panel a is evolving almost at constant mass. The reason is that for this model, I adopted the mass-loss recipe $\dot{M}_{rdw}$ with $Z = 0$. On the other hand, for models in panels b, c, and d the total mass of the star decreases during the evolution. This is most evident for the stars in panels b and d, during the first part of the MS, when the

pulsation-driven mass loss is operating.

After the depletion of hydrogen in the stellar core and the start of the cHeB phase, these four models experience DUP episodes. In Figure 6.2 there are different degrees of envelope penetration, which imply different internal mixing. DUP episodes affect the structure of these models by reducing the mass of the helium core, which can be crucial for the final fate of the stars (see Section 6.2.4). They also impact the chemical composition of these four models. Depending on the efficiency of the DUP, these stars can remain classical red supergiants or they can become WRm stars. Despite the DUP, the model in panel a retains enough hydrogen at the surface such that it does not become a WRm star, while the opposite occurs for models in panels b, c, and d (see also Section 6.2.3). The red vertical line shows when $X < 0.3$ at the surface, and we see that this does not occur for the model in panel a. Moreover, the ($M_i = 200\,M_\odot$, $Z = 0$, $\dot{M}_{max}$, $\omega = 0.2$) model in panel b becomes an extreme WRm star, with only 0.11% of hydrogen out of its total final mass. Therefore, this star could be considered a pure helium star with a very small carbon-oxygen core (green line in Figure 6.2b), due to the very deep penetration of the stellar envelope.

The surface abundance evolution and wind ejecta masses of all extreme WRm models, along with other selected tracks, are discussed in the next section.

6.2.3 Surface Chemical Abundances and Mass of the Ejecta

In this section, I consider the surface abundances and the wind ejecta mass of some selected models. Both of these are affected by rotation-induced mixing, dredge-up episodes, and mass-loss history.

Figure 6.3 presents the surface abundance evolution of H, He, C, N, O, and $Z_{eff} = 1 - X - Y$. Each panel shows the results for the same model computed with two different mass-loss prescriptions, $\dot{M}_{rdw}$ (dotted line) and $\dot{M}_{max}$ (solid line). In Figure 6.3 there are all six extreme WRm models.

During MS, we see the effect of rotation-induced mixing, especially in the four $Z = 0$ models (panels a, b, c, and d). That is, for example, the gradual increase in nitrogen surface abundance, along with a slower enhancement in carbon and oxygen. Approximately $\sim 10^5$ yr before the end of computations, all six models start to experience DUP episodes. During cHeB, the hydrogen surface abundance lowers below 0.3 (vertical red line in each panel), while the effective metallicity increases very steeply. At the end of computations, all extreme WRm models in Figure 6.3 have $Z_{eff} > 0.6$, reaching ~ 0.77 in panel d for the highest initial rotational velocity. The interesting thing to notice is that at $Z = 0$, the mass-loss prescription accounting also for pulsation-driven mass loss favors the metal enrichment during the evolution, while at $Z = 0.0002$ the extreme WRm models are computed with $\dot{M}_{rdw}$. In panels c, d, and f, both models can be considered WRm stars (two red vertical lines), but only one in each plot is almost completely hydrogen-depleted. In these three cases, the extreme WRm models are those that meet the condition $X < 0.3$ earlier on during their evolution. At the end of calculations, these six extreme WRm stars have a surface composition mainly of helium, nitrogen, and oxygen.

Figure 6.4 shows the wind ejecta mass for He, C, N, O, Ne, and Mg, while tables of wind ejecta for all rotating models can be found on Zenodo[2]. In the six panels of

[2] https://doi.org/10.5281/zenodo.10225140

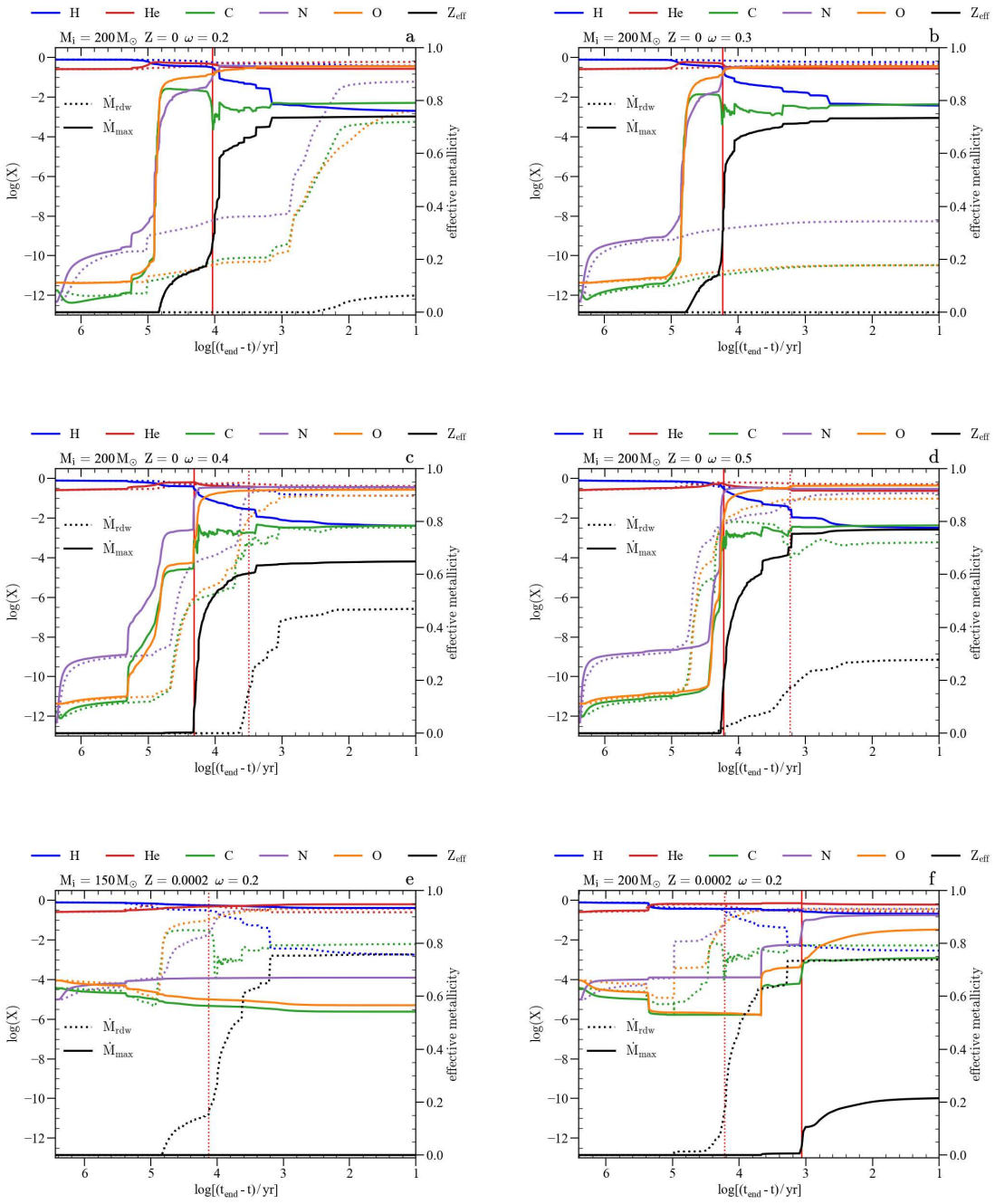

Figure 6.3: Surface chemical abundances' evolution of six selected pairs of models, from the ZAMS to ten years before the end of computations. In each panel, the abundances of hydrogen, helium, carbon, nitrogen, and oxygen, are color-coded as shown in the legend. The black line represents the effective metallicity, $Z_{eff} = 1 - X - Y$. The red vertical line marks when $X < 0.3$. The results are presented for two different mass-loss prescriptions. The horizontal axis is as in Figure 6.2.

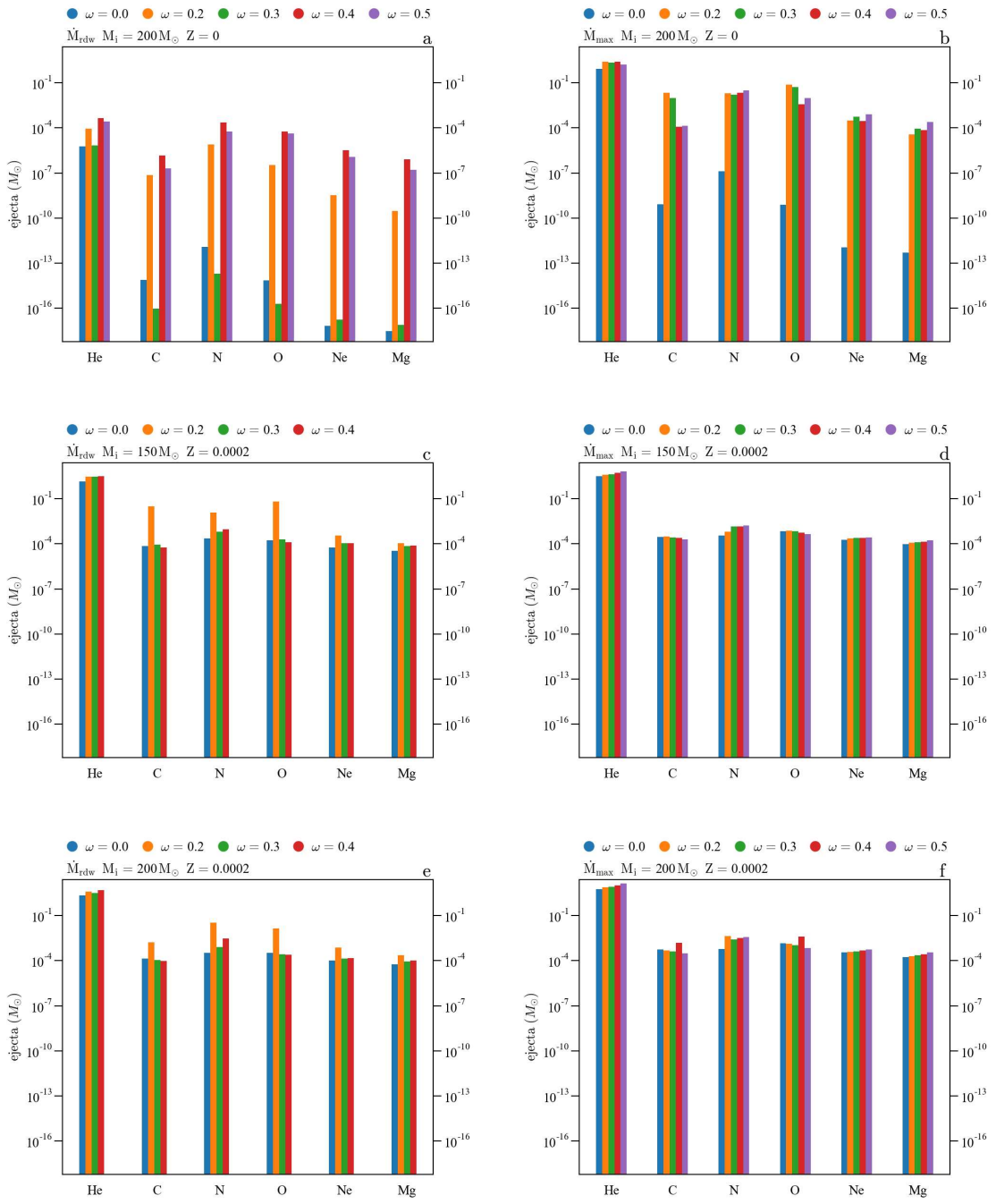

Figure 6.4: Wind ejecta mass of models with initial mass $M_i/M_\odot = 150, 200$. In each panel, there are the ejecta masses of helium, carbon, nitrogen, oxygen, neon, and magnesium for two mass-loss recipes, $\dot{M}_{rdw}$ and $\dot{M}_{max}$. *Panels a,b*: models calculated with Z = 0. *Panels c, d, e, f*: models calculated with Z = 0.0002.

Figure 6.4 there are all the models presented in Figure 6.3 along with stellar tracks computed with their same mass and metallicity, but different initial rotational velocity and

mass-loss prescription. In panels b, c, and e there are the extreme WRm models discussed in Sections 6.2.1 and 6.2.3. In these six panels, we can see the effect of different initial rotational velocities on wind ejecta masses, and also the impact of the DUP episodes. Instead, panels a-b, c-d, and e-f show the incidence of the two mass-loss prescriptions $\dot{M}_{rdw}$ and $\dot{M}_{max}$. The general trend is that accounting also for pulsation-driven mass loss, the ejecta mass of the considered elements increases. This is expected since the definition of the two mass-loss recipes adopted. Considering the initial metallicity of the models, at higher Z_i we have higher ejecta masses due to higher mass-loss rates. However, the most impactful process for example in panels a, b, c, and e is the occurrence of DUP episodes.

The extreme WRm models eject much more metals compared to the others and this is because of a deeper penetration of the stellar envelope (DUP) coupled to the mass loss history of the model. In panel a there are no extreme WRm models, but still, we see major differences between stars computed with $\omega = 0.2$, 0.4, and 0.5 with respect to those with $\omega = 0.0$, and 0.3. The reason for this is the metal enrichment of the models due to DUP episodes (see also Figure 6.3a). Finally, I can say that the differences in the ejecta are due to differences in the mass loss history, except when dealing with models with a very high metal enrichment due to DUP mixing episodes. In these latter cases, the relative ejecta mass of the elements considered is much higher, meaning that mass loss alone can not explain these differences and the main driving process is the mixing due to DUP episodes.

6.2.4 Final fate

Figure 6.5 shows the final helium core mass (M_{He}) at the end of calculations for all tracks. I use M_{He} as a proxy for the final fate of the star, following Woosley (2017); Farmer et al. (2019). M_i and M_{He} are positively related, however, both panels present stellar models that do not follow this trend. This is caused by DUP episodes that reduce the helium core of the models and in some cases even affect their final fate. The helium core mass is defined by the chemical composition of the envelope, and for this reason, for the 16 WRm stars (see Section 6.2.1) I consider two extreme possible cases for the final fate. In the first one, as usual, I use the M_{He} core to determine the final fate. While, in the second case, I use the total final mass of the star at the end of the computations (M_f) to derive the final fate. The combined effects of rotation and DUP episodes affect the stellar tracks in different ways. In panel a for example, we can see that rotation increases the helium core mass with respect to the non-rotating case for $M_i = 100\,M_\odot$ (see also Table 6.2). At the same time, DUP episodes and higher mass loss rates prevent a steady growth of the helium core with increasing initial rotation rate.

Stars with $M_i = 150$, $200\,M_\odot$ have He cores that are massive enough to cause a PISN, which disrupts the whole star. There are some exceptions though. In panel a, seven tracks do not follow the main pattern. Four of these models were computed with $\dot{M}_{max}$ and only one has $M_i = 150\,M_\odot$. This latter is computed with $\dot{M}_{rdw}$, $\omega = 0.5$ and has three possible fates. If we consider the strict definition of its helium core, this latter has a mass of $64.3\,M_\odot$. With this core, the model is inside the uncertainty strip around the PI - PPI boundary. The lower limit of this strip is set to $63.91\,M_\odot$, while the upper one is $65.24\,M_\odot$. They are the He core masses of the T135D and T140D models from Woosley (2017), respectively. These two models are computed with $Z = Z_\odot/10$ and $\dot{M} = 0$, sim-

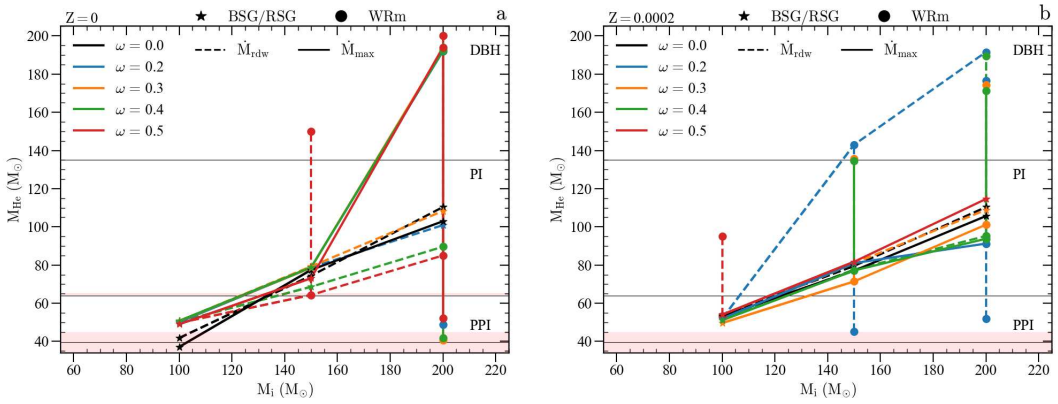

Figure 6.5: Each panel shows the helium core mass, M_{He}, as a function of the initial mass for all models of five different initial rotation rates with a fixed initial metallicity. Helium core mass is shown at the end of the calculations. Horizontal lines limit the PPI, PI explosion, and DBH regimes from bottom to top (Woosley 2017; Farmer et al. 2019, 2020). The lower red strip indicates the uncertainty range of the lower limit for PPI. Lower and upper boundaries are $34\,M_\odot$ (Woosley 2017), and $45\,M_\odot$ (Farmer et al. 2019), respectively. The black line is the average. *Panel a*: similar uncertainty strip between PPI and PI with boundaries $63.91\,M_\odot$ and $65.24\,M_\odot$. These values are the helium core masses of the T135D and T140D models from Woosley (2017), respectively (see text for more details).

ulating the evolution of a zero-metallicity star. Even though these two models have a He core mass very close, and in one case exceeding, the $64\,M_\odot$ limit, Woosley (2017) found that they produced a stellar mass BH. For this reason, I indicate that the stellar model with He core mass between these two limits could have two possible final fates: a PISN with no remnant or a PPISN leaving a stellar-mass BH. On the other hand, the low amount of hydrogen of the ($M_i = 150\,M_\odot$, Z = 0, $\dot{M}_{rdw}$, $\omega = 0.5$) star *could* imply that the helium core corresponds to the total final mass of the star, $M_{He} = 150\,M_\odot$. In this case, the final fate of the model should be DBH. This latter scenario also applies to the ($M_i = 200\,M_\odot$, Z = 0, $\dot{M}_{rdw}$, $\omega = 0.4$) and the ($M_i = 200\,M_\odot$, Z = 0, $\dot{M}_{rdw}$, $\omega = 0.5$) models if I consider $M_{He} = M_f$ (see Tables 6.1 and 6.2 for the different final fates considered for each model).

The other tracks in panel a with $M_i > 100\,M_\odot$ that do not become PISN are the models ($M_i = 200\,M_\odot$, Z = 0, $\dot{M}_{max}$) with $\omega = 0.2$, 0.3, 0.4 and 0.5. These four models are extreme WRm stars due to their almost H-free envelopes (see Sections 6.2.1 and 6.2.3). By considering their helium core masses, these models should undergo PPISN or fCCSN (see Figure 6.5 and Tables 6.1 and 6.2). On the other hand, in the case where $M_{He} = M_f$, their helium cores are above the $135\,M_\odot$ upper threshold for PISN, thus these stars should directly collapse forming a massive BH.

In panel b there are nine WR-manqué stars, five of which are computed with $\dot{M}_{max}$. Both the $M_i = 150\,M_\odot$ and $M_i = 200\,M_\odot$ models with $\dot{M}_{rdw}$ and $\omega = 0.2$ have $M_{He} > 135\,M_\odot$, in the case of $M_{He} = M_f$. Therefore, these two models *could* undergo DBH. Besides these two, seven stars in this panel have a double final fate. The ($M_i = 150\,M_\odot$, Z =

0.0002, $\dot{M}_{max}$, $\omega = 0.3, 0.4$), ($M_i = 200\,M_\odot$, $Z = 0.0002$, $\dot{M}_{max}$, $\omega = 0.2,\ 0.3, 0.4$) and ($M_i = 200\,M_\odot$, $Z = 0.0002$, $\dot{M}_{rdw}$, $\omega = 0.4$) models can either collapse directly to a BH or get totally disrupted in a PISN, depending on the helium core mass considered. On the other hand, the ($M_i = 100\,M_\odot$, $Z = 0.0002$, $\dot{M}_{rdw}$, $\omega = 0.5$) star is in the PPISN or PISN regime in the case $M_{He} < 64\,M_\odot$ or $M_{He} = M_f$, respectively (see also Table 6.1).

In both panels of Figure 6.5, stars with $M_i = 100\,M_\odot$ are in the pulsational-pair-instability regime, but outside the uncertainty region. The only exceptions are the two models computed with $\omega = 0.0$ (see discussion in Chapter 4) and ($M_i = 100\,M_\odot$, $Z = 0.0002$, $\dot{M}_{rdw}$, $\omega = 0.5$) already discussed above.

As in Chapter 4, I use the fit formula proposed by Mapelli et al. (2020, see Appendix 6.D for details) to compute the BH mass in the PPISN scenario, while also accounting for mass loss due to neutrino emission (10% of the baryonic mass of the proto-compact object, see Fryer et al. 2012; Rahman et al. 2022, and references therein). In DBH cases, I take the final mass of the star as a first approximation for M_{BH}, always accounting for mass loss due to neutrino emission. In Table 6.1 and 6.2, I give two (or even three) possible outcomes and the corresponding BH masses for all models with an uncertain fate based on the boundaries in Figure 6.5. Notice that for the ($M_i = 150\,M_\odot$, $Z = 0.0002$, $\dot{M}_{max}$, $\omega = 0.4$) model, I assume a 1% error on the $135\,M_\odot$ threshold for the upper limit for PISN in the fit formula by Mapelli et al. (2020). It is worth mentioning that these limits are based on non-rotating models, as long as the fit formula from Mapelli et al. (2020). There are different studies on the pair-instability limits and the effects of rotation, e.g. Glatzel et al. (1985); Woosley (2017); Marchant and Moriya (2020); Woosley and Heger (2021). For example, Woosley and Heger (2021) mention that high rotation rates could shift the lower limit for pair instability from $64\,M_\odot$ to $\sim 70\,M_\odot$. For the case where the He core mass is close to the $64\,M_\odot$ limit ($M_i = 150\,M_\odot$, $Z = 0$, $\dot{M}_{rdw}$, $\omega = 0.5$), I can not calculate the BH mass with the fit formula from Mapelli et al. (2020). For this reason, I use a linear interpolation between M_{He} and M_{BH} of the models T135D and T140D. In this way, I can give an estimate of the BH mass for the case of PPISN (see also Table 6.2).

Tables 6.1 and 6.2 and Figure 6.6 show the results obtained with different mass-loss prescriptions and initial rotation rates. In Figure 6.6, whenever there are multiple symbols for the same stellar model, it indicates that for that particular star, there is more than one possible outcome. For $Z = 0$, the most massive BHs reach $\sim 180\,M_\odot$, while for $Z = 0.0002$ they reach $\sim 172\,M_\odot$. The complex interplay between DUP and rotation sets the final mass of the BHs I expect from my models. It is worth noticing that rotation favors the occurrence of DUP episodes, shifting in some cases the mass of the possible remnant from zero to hundreds of solar masses. Within Section 6.2.5, the remnants' mass will be re-discussed and adjusted according to results from the analysis on possible jet-driven events (see also Tables 6.3 and 6.4).

6.2.5 Progenitors of Jet-driven Events

Within the collapsar scenario (Woosley 1993), the most important characteristics for being a GRB progenitor are a massive core to produce a BH, the lack of an extended hydrogen envelope to facilitate the jet outward propagation and high core specific angular momentum for the formation of an accretion disk. There are, however, different studies that suggest the possibility of a jet propagation even through the very massive envelope of

Table 6.3: Most Relevant Properties of Possible GRB Events for Models Computed with Z = 0.0002, $\dot{M}_{rdw}$ and $\dot{M}_{max}$

M_i [$M_\odot$] (1)	τ_{cross} [s] (2)	$\tau_{free-fall}$ [s] (3)	$\tau_{accretion}$ [s] (4)	$L_{accretion}$ [$\log_{10}$(erg s^{-1})] (5)	$E_{accretion}$ [$\log_{10}$(erg)] (6)	$E_{binding,\,envelope}$ [$\log_{10}$(erg)] (7)	Fate (8)	M_{BH} [$M_\odot$] (9)
				$\dot{M}_{rdw}$ ω = 0.2				
100	0.35	3.35	2.45	52.48	52.87	-	c	39.8
150	46.8	$5.09 \cdot 10^3$	5.66	52.52	52.74	50.21	a	40.2
	$2.32 \cdot 10^3$	$9.94 \cdot 10^5$	5.66	52.52	52.74	50.21	a$^{(a)}$	40.2
200	34.81	$2.97 \cdot 10^3$	6.21	52.09	52.89	51.08$^{(II)}$	d	41.4
	$2.38 \cdot 10^3$	$8.89 \cdot 10^5$	6.21	52.09	52.89	51.08$^{(II)}$	d$^{(a)}$	41.4
				ω = 0.3				
100	0.35	3.34	2.49	52.47	52.86	-	c	39.5
150	-	-	-	-	-	-	PISN	-
200	-	-	-	-	-	-	PISN	-
				ω = 0.4				
100	0.37	3.57	2.58	52.45	52.86	-	c	39.4
150	-	-	-	-	-	-	PISN	-
200	-	-	-	-	-	-	PISN	-
	$7.43 \cdot 10^3$	$4.94 \cdot 10^6$	13.23	52.10	53.22	50.93	d$^{(a)}$	85.7
				ω = 0.5				
100	0.39	3.86	2.97	52.40	52.88	-	c	40.7
	-	-	-	-	-	-	PISN$^{(a)}$	-
				$\dot{M}_{max}$ ω = 0.2				
100	0.35	3.31	2.46	52.48	52.87	-	c	39.6
150	-	-	-	-	-	-	PISN	-
200	-	-	-	-	-	-	PISN	-
	$7.05 \cdot 10^3$	$4.73 \cdot 10^6$	7.72	52.39	52.44	50.88	a$^{(a)}$	82.1
				ω = 0.3				
100	0.35	3.37	2.59	52.43	52.85	-	c	38.2
150	-	-	-	-	-	-	PISN	-
	$6.3 \cdot 10^3$	$4.56 \cdot 10^6$	9.47	52.11	53.09	50.69	d$^{(a)}$	64.3
200	-	-	-	-	-	-	PISN	-
	$6.75 \cdot 10^3$	$4.46 \cdot 10^6$	10.46	52.22	53.24	51.02	d$^{(a)}$	91.0
				ω = 0.4				
100	0.36	3.53	2.66	52.44	52.86	-	c	39.1
150	-	-	-	-	-	-	PISN	-
	$5.11 \cdot 10^3$	$3.35 \cdot 10^6$	8.94	52.17	53.12	50.93	d$^{(a)(III)}$	69.4
200	-	-	-	-	-	-	PISN	-
	$6.77 \cdot 10^3$	$4.52 \cdot 10^6$	11.66	52.14	53.21	50.94	d$^{(a)}$	84.4
				ω = 0.5				
100	0.39	3.8	2.83	52.43	52.88	-	c	40.8
150	-	-	-	-	-	-	PISN	-
200	-	-	-	-	-	-	PISN	-

NOTE—The table entries are as follows: (1) star's initial mass; (2) crossing timescale; (3) free-fall timescale; (4) accretion timescale, $\sum_i \tau_{acc,i}$; (5) accretion luminosity, $\sum_i L_{acc,i}$; (6) accretion energy, $\sum_i \tau_{acc,i} \cdot L_{acc,i}$; (7) envelope binding energy; (8) case for the possible fate of the GRB progenitor according to 4 cases outlined in Figure 6.8; (9) remnant mass

(II) the bottom of the envelope here is defined as the first point where $Y < 10^{-3}$;

(III) assuming an error of 1% on upper limit for PISN in fit formula by Mapelli et al. (2020);

(a) considering $M_{He} = M_f$.

Table 6.4: Most Relevant Properties of Possible GRB Events for Models Computed with $Z = 0$, $\dot{M}_{rdw}$ and $\dot{M}_{max}$

M_i $[M_\odot]$ (1)	τ_{cross} [s] (2)	$\tau_{free-fall}$ [s] (3)	$\tau_{accretion}$ [s] (4)	$L_{accretion}$ $[\log_{10}(erg\,s^{-1})]$ (5)	$E_{accretion}$ $[\log_{10}(erg)]$ (6)	$E_{binding,\,envelope}$ $[\log_{10}(erg)]$ (7)	Fate (8)	M_{BH} $[M_\odot]$ (9)
				$\dot{M}_{rdw}$ $\omega = 0.2$				
100	0.36	3.4	0.65	52.52	52.34		b	39.5
			1.66	52.32	52.54			
150	-	-	-	-	-	-	PISN	-
200	-	-	-	-	-	-	PISN	-
				$\omega = 0.3$				
100	0.36	3.46	2.67	52.44	52.87		c	39.6
150	-	-	-	-	-	-	PISN	-
200	-	-	-	-	-	-	PISN	-
				$\omega = 0.4$				
100	0.36	3.51	3.12	52.37	52.86		c	39.4
150	-	-	-	-	-	-	PISN	-
200	-	-	-	-	-	-	PISN	-
	$7.39 \cdot 10^3$	$4.77 \cdot 10^6$	11.04	52.15	53.19	50.92	d[a]	80.6
				$\omega = 0.5$				
100	0.36	3.47	3.01	52.38	52.86		c	39.0
150	-	-	-	-	-	-	PISN[b]	-
	$6.78 \cdot 10^3$	$4.85 \cdot 10^6$	9.12	52.08	53.04	50.61	d[a]	57.9
	0.31	2.85	2.08	52.50	52.82	-	c[c]	35.8
200	-	-	-	-	-	-	PISN	-
	$7.73 \cdot 10^3$	$5.10 \cdot 10^6$	9.86	52.17	53.17	50.84	d[a]	76.5
				$\dot{M}_{max}$ $\omega = 0.2$				
100	0.35	3.31	0.64	52.50	52.30	-	b	39.2
			1.40	52.23	52.38			
150	-	-	-	-	-	-	PISN	-
200	5.31	$1.80 \cdot 10^2$	0.07	52.40	51.25	-	d*	46.7
	$2.34 \cdot 10^3$	$8.66 \cdot 10^5$	0.07	52.40	51.25	50.43	d[a]	58.6
				$\omega = 0.3$				
100	0.35	3.38	2.66	52.44	52.86	-	c	39.5
150	-	-	-	-	-	-	PISN	-
200	54.73	$6.31 \cdot 10^3$	0.77	52.75	52.36	50.7	a[e]	36.5
	$2.97 \cdot 10^3$	$1.24 \cdot 10^6$	0.77	52.75	52.36	50.7	a[a]-[d]	36.5
				$\omega = 0.4$				
100	0.36	3.41	2.82	52.41	52.86	-	c	39.5
150	-	-	-	-	-	-	PISN	-
200	37.66	$3.57 \cdot 10^3$	5.74	52.08	52.84	50.84	d[e]	37.5
	$2.83 \cdot 10^3$	$1.15 \cdot 10^6$	5.74	52.08	52.84	50.84	d[a]-[d]	37.5
				$\omega = 0.5$				
100	0.36	3.52	3.14	52.35	52.85	-	c	38.3
150	-	-	-	-	-	-	PISN	-
200	6.34	$2.30 \cdot 10^2$	6.92	52.10	52.94	-	c	49.0
	$2.77 \cdot 10^3$	$1.11 \cdot 10^6$	6.92	52.10	52.94	50.9	d[a]	47.1

Note—Table entries as in Table 6.3.
[b] following Woosley (2017) I set the lower limit of M_{He} for PISN at $64\,M_\odot$;
[c] I set the lower limit of M_{He} for PISN at $65.24\,M_\odot$, which is the M_{He} of the T140D model in Woosley (2017);
[d] following Farmer et al. (2019) I set the lower limit of M_{He} for PPISN at $45\,M_\odot$;
[e] following Woosley (2017) I set the lower limit of M_{He} for PPISN at $34\,M_\odot$.
* concerning the expected BH mass, the model follows the c case since it should experience PPI

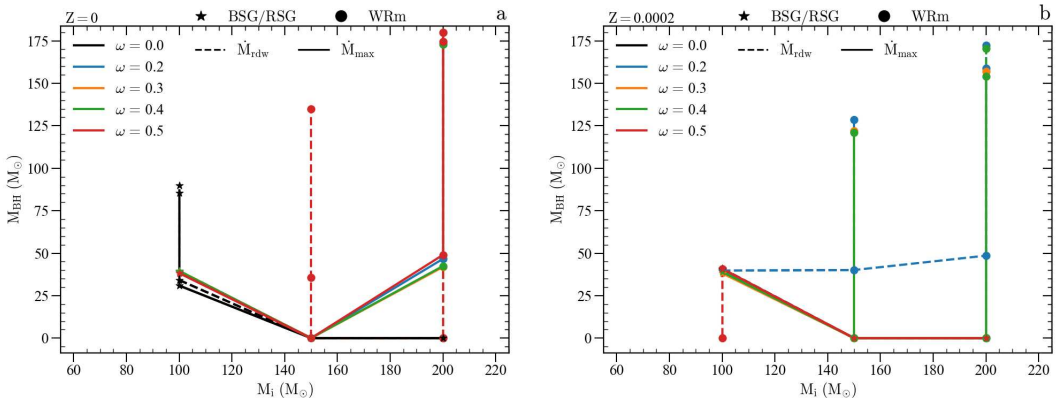

Figure 6.6: Expected remnant mass for all stellar models presented in this work as a function of M_i. The extra symbols indicate the predicted BH mass for those stars with multiple possible fates, see also Tables 6.1 and 6.2. *Panel a*: models calculated with $Z = 0$. *Panel b*: models calculated with $Z = 0.0002$.

Pop III stars (e.g., Ohkubo et al. 2009; Suwa and Ioka 2011; Toma et al. 2011; Nagakura et al. 2012; Wei and Liu 2022). Moreover, there are also multiple criteria for the minimum core specific angular momentum and the mass coordinate to consider when evaluating this latter (e.g., Woosley and Heger 2006; Yoon et al. 2006; Meynet and Maeder 2007; Yoon et al. 2012; Aguilera-Dena et al. 2018; Aloy and Obergaulinger 2021; Obergaulinger and Aloy 2022).

First of all, I have to consider all the shells that have a sufficient specific angular momentum to form a disk instead of falling directly into the newly-formed BH (see Appendix 6.B for a different approach in the calculations of the shell inertial moment). Figure 6.7 shows four example models that summarize all possible cases within my current work. This choice is based on different angular momentum configurations within the progenitors and also the different final fates for the jet-driven events. In each panel, I consider the two limiting cases for the minimum specific angular momentum needed to support mass at the last stable orbit (LSO) of a Schwarzschild and a maximally rotating Kerr BH. Then, the general case considers a BH with mass and angular momentum within the specific mass coordinate in the stellar model (see Bardeen et al. 1972, for the exact expressions). We can see that the specific angular momentum profile is very different between the four models, and therefore the expression $j > j_{crit}$ where I expect disk formation follows different patterns in these four progenitors. I assume that the inner $3\,M_\odot$ of material would form the BH, and therefore do not contribute to the accretion disk. For this reason, I exclude the inner $3\,M_\odot$ from subsequent calculations throughout this work for all my models (see Appendix 6.A where I consider the case of $M_{BH} = 5\,M_\odot$ for the only model where this implies a sizeable difference).

To have enough angular momentum and form a disk is a necessary but not sufficient condition for a successful GRB. On top of that, the lack of an extended envelope is needed to allow the jet outlet. To analyze in further detail the jet propagation through the progenitor, I proceed as in Yoon et al. (2015) by computing the accretion rate from the disk. With the approximation introduced by Woosley and Heger (2012), the accretion

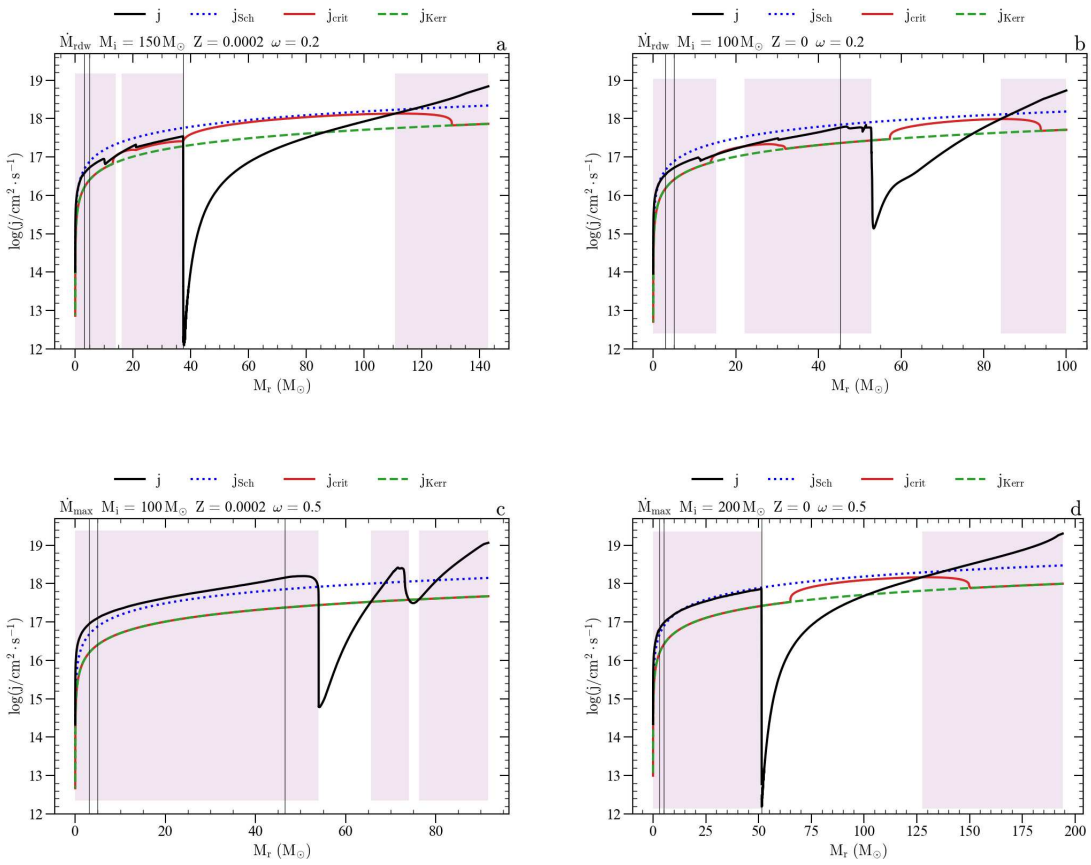

Figure 6.7: Specific angular momentum profile as a function of the mass coordinate. In each panel the black line shows the specific angular momentum for the model considered, the blue line refers to the minimum angular momentum needed to support mass at the LSO of a Schwarzschild BH, while the green line denotes the minimum angular momentum for a maximally rotating Kerr BH. The red line shows the specific angular momentum at the LSO for a BH with mass and angular momentum inside the considered mass coordinate in the computed stellar model. All panels show in lilac the regions within the stars where $j > j_{crit}$. In these regions, I expect the formation of an accretion disk. The two innermost vertical lines in each panel refer to the mass coordinate $3\,M_\odot$ and $5\,M_\odot$, respectively; while the outer one corresponds to the carbon-oxygen core of the model considered.

rate reads

$$\dot{M} = \frac{2M_r}{t_{ff}} \frac{\rho}{\bar{\rho} - \rho}, \tag{6.5}$$

with $t_{ff} = 1/\sqrt{24\pi G\bar{\rho}}$ the free-fall timescale and $\bar{\rho} = 3M_r/4\pi r^3$ the mean density within each shell. As in Yoon et al. (2015), also in this work such accretion rates should be considered as lower limits. This is because my models do not reach the pre-collapse stage, and hence the density should increase with respect to the considered one.

Figure 6.8 shows the accretion rate, the free-fall timescale, and the crossing timescale

for those models presented in Figure 6.7. Also in these four panels, I highlight where the shells have enough specific angular momentum to support a disk (see Figure 6.7 and related discussion). Panels b and c do not show the entire progenitor. This is because in the PPISN cases, I plot only the model up to the mass coordinate calculated with the fit formula by Mapelli et al. (2020). In this way, I consider the model after the loss of the envelope due to pulsational-pair instability (Ekström et al. 2008), assuming that the pair-induced pulsations do not affect the angular momentum of the stellar core (Aguilera-Dena et al. 2018). As a first approximation for the velocity of the ejected material due to PPI, I consider the escape velocity at the mass coordinate given by the fit formula from Mapelli et al. (2020). I find that $v_{esc} \sim 10^4\,km\,s^{-1}$ and the timescale between the pulsational-pair instability and the collapse of the star should be of the order of $\sim 100\,yr$. I can safely stop considering the ejected material in my calculations since it should be at distances of $\sim 1\,pc$ when the jet forms, thus reducing the density of the ejected envelope by a factor $(1\,pc)^3$. Instead, in panels a and d I show the entire stellar model since I consider the $M_{He} = M_f$ case and therefore the stars do not undergo PPI (see Section 6.2.4 and Tables 6.1, 6.2).

The models in Figure 6.8 represent the four possible cases for a jet-driven event among all my rotating stellar tracks, except those that undergo PISN. For this reason, I assign the letter a, b, c, or d in the final fate column of Tables 6.3 and 6.4, according to the structure and final fate of the models following one of these four possible cases. Tables 6.3 and 6.4 also summarize different physical properties of possible jet-driven events for all rotating models considered in this work.

The model in Figure 6.8a does not experience pulsational-pair instability and it is within the DBH scenario (taking the upper limit $M_{He} = M_f$, note in Table 6.3 that the final fate should not change even considering the lower value for M_{He}). Therefore, I plot the entire stellar structure where the final mass of the model is $143\,M_\odot$. Panel a shows that there could be three distinct accretion episodes due to the distribution of specific angular momentum within the star from matter at $3\,M_\odot - 14\,M_\odot$, $16\,M_\odot - 38\,M_\odot$ and $111\,M_\odot - 143\,M_\odot$, respectively.

Combining the first two accretion episodes, the accretion timescale for matter within the stellar core is 5.66 s. However, this is much lower compared to the crossing timescale for jet propagation through the envelope, which is $\sim 10^3$ s (see Table 6.3). This shows that the jets powered by core accretion are not expected to produce a successful GRB, due to a much difficult jet propagation. Moreover, the crossing timescale is more than two orders of magnitude smaller than the free-fall timescale ($\tau_{cross} \ll \tau_{ff}$), and thus the jets would not remain collimated during its propagation within the star (Yoon et al. 2015). Following Suwa and Ioka (2011), to calculate the energy of a jet I assume the following expression for the luminosity:

$$L = \eta\,\dot{M}\,c^2, \tag{6.6}$$

where $\dot{M}$ is the mass accretion rate from Eq. 6.5 and the accretion-to-jet conversion efficiency is $\eta = \eta_0\,a^2 = 10^{-3}\,a^2$, where a is the dimensionless spin parameter ($a = J \cdot c/(G \cdot M^2)$) of the central BH with $M_{BH} = 3M_\odot$ and J the corresponding angular momentum. The first term η_0 comes from Suwa and Ioka (2011), while the dependence on the BH spin is from Blandford and Znajek (1977). In those models where there are two accretion episodes within the stellar core, to calculate the luminosity of the second

jet I assume $M_{BH} = 3\,M_\odot + M_{acc}$, where M_{acc} is the total mass accreted by the BH before the second accretion episode. Thus, also the accretion-to-jet efficiency changes too, because the dimensionless spin parameter is not calculated for a BH of $3\,M_\odot$ as for the other jets. The energy that the jets pump into the stellar envelope is $\sim 3.3 \cdot 10^{52}$ erg. Because these jets can not break out from the progenitor and they are going to spread out instead of remaining collimated, I sum their energy to compare it with the binding energy of the envelope. I define the bottom of the stellar envelope as the first point where $X < 10^{-3}$ (note the only exception in Table 6.3 to estimate more accurately M_{BH}), hence the total envelope binding energy is $\sim 1.6 \cdot 10^{50}$ erg. Because of this, the whole envelope would be ejected by the jets' energy, therefore hindering the third accretion episode. In this case, the final outcome of the model should be a jet-driven SN.

In panel b, the model has enough angular momentum in its inner core to support the formation of an accretion disk. The first accretion episode lasts 0.65 seconds, while the crossing timescale for the jet to reach the surface of the star is 0.36 seconds. This means that in this case, there could be a successful GRB event, powered by the accretion of matter between $3\,M_\odot$ and $15\,M_\odot$. The crossing timescale is more than four times smaller compared to the accretion timescale for matter between $22\,M_\odot$ and $44\,M_\odot$. This implies that the second accretion episode can not form another jet before the first one breaks out from the star. Here I assume as an upper limit that the first jet does not blow away any mass of the outer stellar core, though this mass could be very little (Zhang et al. 2004). Thus, in this case, we have two accretion episodes that produce successful GRBs."Case b" corresponds to progenitors of successful GRB events that are powered by two accretion episodes, where in Tables 6.3 and 6.4 there are the results for the two jets in the τ_{acc}, L_{acc}, and E_{acc} columns.

Case c is very much similar to the latter. The only difference is that the entire model has enough angular momentum to form a disk: there is a single accretion episode that involves the whole star. Even in this case, the accretion timescale is higher concerning the crossing one, 2.83 and 0.39 seconds, respectively. Therefore, this model should also produce a successful GRB event. Here I assume that the whole mass of the star is going to be accreted, and this gives an upper limit for the accretion timescale and hence the total accretion energy of GRB progenitors that follow the kind of structure presented in this case c.

The model in Figure 6.8d is very similar to that in panel a (taking the upper limit $M_{He} = M_f$). As between cases b and c, the most important difference is that in Figure 6.8d there should be only one accretion episode from matter within the stellar core. Even in this case, the accretion timescale is much shorter compared to the crossing timescale, (see Table 6.4). Hence, also in this model, the jet powered by core accretion should produce a jet-driven SN, to which I refer as final fate d in Tables 6.3 and 6.4. On the other hand, if I consider the lower value of M_{He} for this specific model, the jet-driven event changes deeply. Because of the lack of an extended envelope, the jet could reach the stellar surface and produce a successful GRB (see Table 6.4 for the numerical details).

Tables 6.3 and 6.4 also present the expected mass of the remnant after the jet-driven event, where also here I account for neutrino emission and take 90%[3] of the considered final mass for the expected M_{BH} (Fryer et al. 2012; Rahman et al. 2022, and references therein). For jet-driven SNe in cases a and d, I consider only the mass of the core,

[3]I assume this for consistency with the discussion in Section 6.2.4

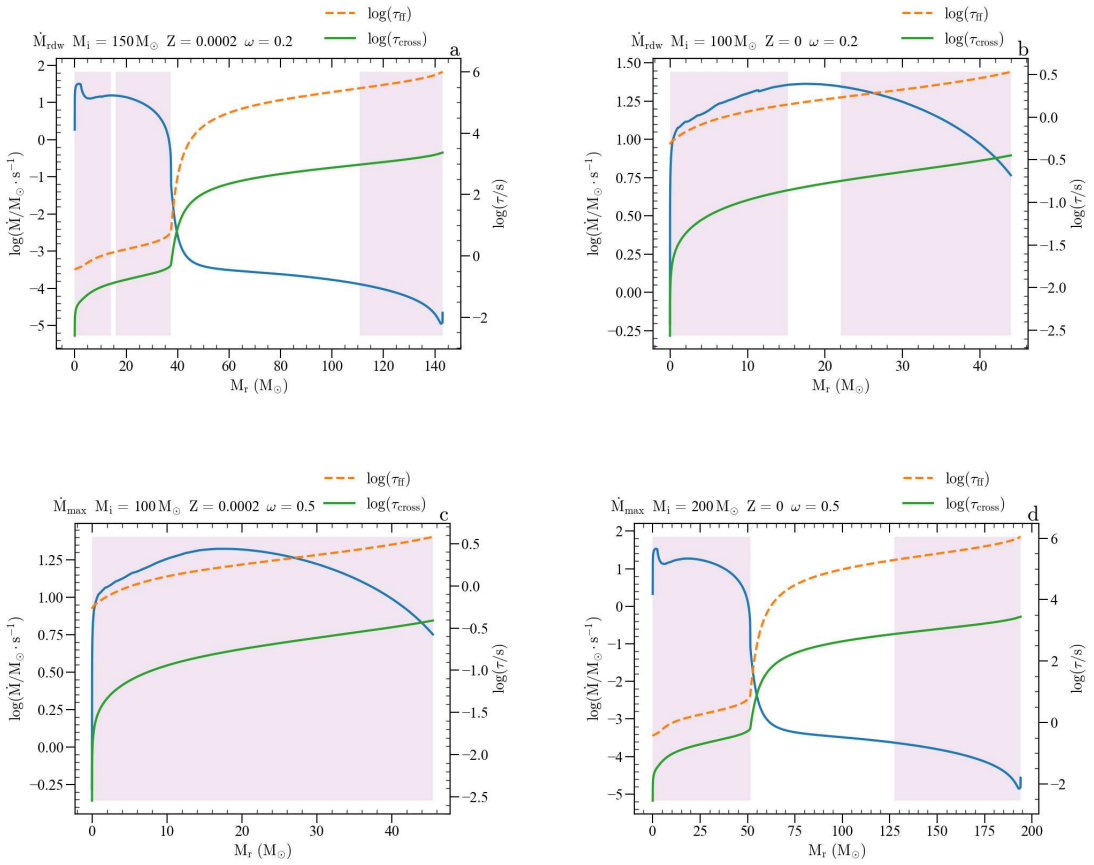

Figure 6.8: Accretion rate, free-fall timescale, and crossing timescale as a function of the mass coordinate. Lilac regions show the shells with sufficient specific angular momentum to support a disk, where $j > j_{crit}$. The two timescales refer to the y-axis on the right, while the accretion rate is shown on the left.

because the envelope is ejected by the energy of the jet(s). Instead, in cases b and c I take into account the total mass of the model after pulsational-pair instability mass loss. All values in the last column in Tables 6.3 and 6.4 are to be considered as upper limits for the BH mass. This is because there could be more mass ejected by the jet, even though it might not be that large (Zhang et al. 2004).

Figure 6.9 shows the luminosity due to accretion-powered jets for all rotating models considered (except those that undergo PISN). The two brightest GRB events have $\log(L) \sim 52.5$. The main driver of the jet-powered events is the accretion rate shown in Figure 6.8, which depends on the density of the models.

Now I consider different values for the accretion-to-jet conversion efficiency parameter. With $\eta_0 = 10^{-2}; 10^{-4}$, the overall results do not change. Of course, I obtain respectively higher and lower luminosities and accretion energies, but the cases highlighted in Tables 6.3 and 6.4 remain unchanged. There is only one exception, which is the ($M_i = 200\,M_\odot$, $Z = 0$, $\dot{M}_{max}$, $\omega = 0.2$) model in the case of DBH scenario (see Table 6.4). With $\eta_0 = 10^{-4}$ the accretion energy results lower than the binding energy of

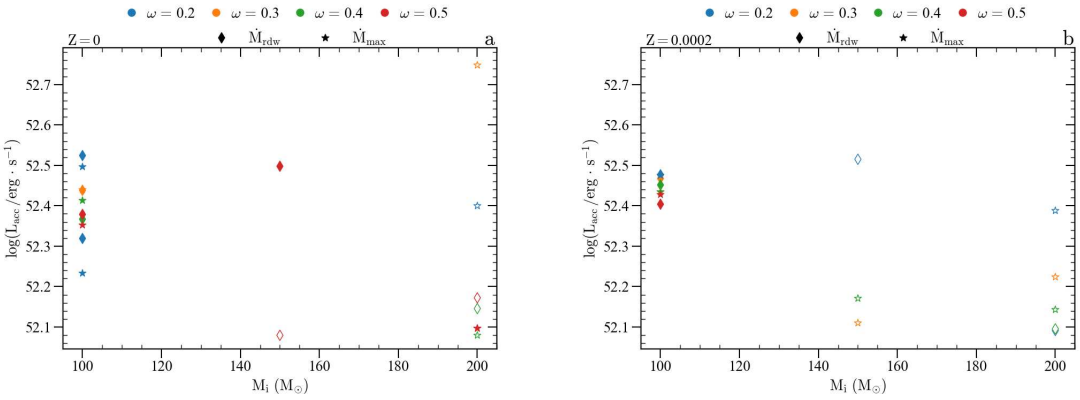

Figure 6.9: Jet-driven luminosity for all rotating models besides those that undergo PISN. Different colors indicate the initial rotation rate of the models, while different symbols indicate the mass-loss prescription used in the computations. Full symbols indicate a successful GRB event, while the others refer to jet-driven SNe. *Panel a*: all models with initial metallicity $Z = 0$; *Panel b*: all models with initial metallicity $Z = 0.0002$.

the stellar envelope. Thus in this case the expected remnant mass from this progenitor is higher, $78\,M_\odot$. It is worth noting that this latter is almost $20\,M_\odot$ above the value expected when the total stellar envelope is ejected by the energy of the jet. Considering this lower efficiency, I should expect a failed jet-driven SN from this progenitor, which greatly impacts the final mass of the BH.

6.3 Concluding Remarks

In this work, I study the evolution of rotating zero-metallicity and metal-poor very massive stars, with initial masses between $100\,M_\odot$ and $200\,M_\odot$. I investigate the resulting effect arising from different initial rotation rates $\omega = 0.0$, 0.2, 0.3, 0.4, 0.5 and pulsation-driven winds (following the prescription of Nakauchi et al. 2020), accounting also for radiation-driven winds throughout the entire HRD. These are the first very massive models that consider both stellar rotation and pulsation-driven mass loss, extending the parameter space covered by the PARSEC evolutionary tracks. I follow the evolution until the occurrence of electron-positron pair instability after carbon, neon, or oxygen ignition depending on the initial mass, metallicity, rotation, and mass-loss prescription adopted for the models (see Tables 6.1 and 6.2). For all models, I checked that rotation and radial pulsations should not influence each other, with the former dominating over the latter (see discussion in Appendix 6.C).

As in Chapter 4, I discuss the final fate of these stars (Section 6.2.4), but then accounting also for stellar rotation I analyze the possibility of jet-driven phenomena from these rotating progenitors (Section 6.2.5). I consider the accretion-to-jet efficiency parameter $\eta = \eta_0 a^2$, where $\eta_0 = 10^{-2}$, 10^{-3}, 10^{-4}, while a is the dimensionless spin parameter of the central BH with $M_{BH} = 3\,M_\odot$ (see Appendix 6.A where I explore the $M_{BH} = 5\,M_\odot$ case). Results in Tables 6.3 and 6.4 assume the standard value of

$\eta_0 = 10^{-3}$ from Suwa and Ioka (2011). Following the analysis of Yoon et al. (2015), I identify four possible cases among my rotating models with different structures and final fates.

For stars that do not lose any mass due to pair instability and still form a BH (DBH scenario, cases a and d), the expected outcome is a jet-driven SN. In these cases, the extended stellar envelope prevents the jet breakout, but the energy of this latter is higher than the envelope binding energy, and thus the jet unbinds the outer layers of the star. The progenitors of these successful jet-driven SNe have $M_i = 200\,M_\odot$, except for four models with $M_i = 150\,M_\odot$ (see Tables 6.3 and 6.4). Within case d when considering $\eta_0 = 10^{-4}$, there is only one exception to the fact that the accretion energy of the jet is bigger than the envelope binding energy, i.e. ($M_i = 200\,M_\odot$, Z = 0, $\dot{M}_{max}$, $\omega = 0.2$) model when considering $M_{He} = M_f$. This implies an increase of the expected BH mass of almost $20\,M_\odot$.

All models that undergo pulsational-pair instability lose their envelope, hence fostering the propagation of the jet as opposed to the models in Yoon et al. (2015). Case b and c correspond only to models with $M_i = 100\,M_\odot$, except the ($M_i = 150\,M_\odot$, Z = 0, $\dot{M}_{rdw}$, $\omega = 0.5$) model, which has three possible fates (see Table 6.4). The major difference between the b and c scenarios is that in the former the star does not have enough angular momentum throughout the whole structure, and thus there are two distinct accretion episodes. Instead, in the latter, the whole mass of the star is accreted through the disk in one single episode, which increases the accretion timescale. This difference also occurs between models in cases a and d.

A factor potentially pivotal in the evolution of these rotating stars, which is not addressed in this Thesis, is magnetic angular momentum transport (Walder et al. 2012; Keszthelyi 2023). Magnetic fields effectively transfer angular momentum from the stellar core outward (Aerts et al. 2019, and references therein). Consequently, the surface rotational velocity may increase compared to non-magnetic stars. This could influence chemical mixing and expected mass loss rates in these models. Conversely, magnetic stars may have slower-rotating stellar cores, impacting anticipated final outcomes. Due to magnetic angular momentum transport and magnetic field interactions with stellar winds, these rotating stellar models might exhibit specific angular momentum profiles below the required threshold for successful GRB events.

A GRB event can be detected by the BAT X-ray detector up to redshift z $\sim$ 20 if it has $L \gtrsim 10^{52}\,erg\,s^{-1}s$ (Komissarov and Barkov 2010; Yoon et al. 2015). All successful GRB events displayed in Figure 6.9 would be luminous enough to be detected. This changes as I consider different values for the parameter η_0. When adopting a lower value for efficiency, all the models get below the observability threshold above. On the other hand, increasing the accretion-to-jet efficiency boosts the possibility of detecting this kind of event. Also, the afterglow of these GRBs could be of paramount importance. The reason is that with a bigger energy budget, and therefore a radio flux peaked at late times at gigahertz frequencies (Toma et al. 2011), the radio afterglow of GRBs from Pop III progenitors should be much brighter than that of Pop II/Pop I stars (Salvaterra 2015; Burlon et al. 2016). Hence, this could be key for distinguishing GRB events from different progenitor populations. With current instruments like the Australian Square Kilometer Array Pathfinder telescope and James Webb Space Telescope with both Near-InfraRed Camera and Near-InfraRed Spectrograph, the observation of the afterglow from Pop III

GRB events should be within reach (Macpherson and Coward 2017).

Jet-driven events also have a deep impact on the expected M_{BH} for some of these progenitors. Comparing the results for the expected BH mass in Tables 6.1 and 6.2 with those in Tables 6.3 and 6.4, there are fifteen models with a different remnant mass. These stars are all within the a and d cases (see discussion in Section 6.2.5), while for models following cases b and c, the expected mass of the BH does not change. The differences are due to jet-driven SNe that unbind the stellar envelope during the accretion-powered jet's propagation. Hence, the BH mass can be reduced by more than $130\,M_\odot$ in the most extreme cases.

Out of fifteen models with a reduced M_{BH}, thirteen stars have an expected remnant mass that falls within the pair-instability black-hole mass gap ($40 - 65\,M_\odot$ to $120\,M_\odot$, see also Farmer et al. 2020; Sakstein et al. 2020; Croon et al. 2020; Farrell et al. 2021; Costa et al. 2021; Vink et al. 2021; Tanikawa et al. 2021; Farag et al. 2022, for different formation scenarios). Several stellar models can produce BHs with a mass close to one of the primary and the secondary BHs in the gravitational wave event GW190521 (Abbott et al. 2020), which are $85^{+21}_{-14}\,M_\odot$ and $66^{+17}_{-18}\,M_\odot$, respectively. Therefore, rotating primordial very massive stars could provide a new pathway for the formation of BHs within the pair-instability black-hole mass gap.

Appendix 6.A An alternative case for central Black Hole mass

Here I investigate the case study where I assume $M_{BH} = 5\,M_\odot$ instead of $3\,M_\odot$, while keeping $\eta = 10^{-3}\,a^2$. The different mass of the central BH has two major effects on the calculations for the jet-driven episode. First, there are two solar masses less for the BH to accrete, which impacts the total rate of mass accretion and the accretion timescale. Taking out some of the material with a high accretion rate reduces $\dot{M}$ while increasing τ_{acc}. The second effect is that in the luminosity calculations, I have to take into account the dimensionless spin parameter derived for the inner $5\,M_\odot$. This in principle has a different value compared to $a(M_{BH} = 3\,M_\odot)$.

For all my rotating models, considering $M_{BH} = 5\,M_\odot$ has very little effects on the results shown in Tables 6.3 and 6.4. At most there is a difference of $\sim 0.5\,s$ in τ_{acc} and ~ 0.01 in $\log(L_{acc})$. The only exception is the ($M_i = 200\,M_\odot$, $Z = 0$, $\dot{M}_{max}$, $\omega = 0.2$) model when I consider $M_{He} = M_f$, whose timescales and accretion rates are shown in Figure 6.A.1. We see that there are no shells with $j > j_{crit}$ within the core outside $5\,M_\odot$. The model has sufficient angular momentum only in the very outer envelope, but the accretion rate there is much lower compared to the inner core. Since all the inner layers of the star would fall into the BH right away, the jet formed by the accretion of the outer layers would not have to pierce any stellar envelope and therefore in this case the crossing timescale is zero.

In this particular case, the model could be a progenitor of a successful GRB, but much fainter than those presented above due to the lower accretion rate. The luminosity is $L \sim 9.3 \cdot 10^{45}\,erg\,s^{-1}$, and this transient could last for more than two weeks because of the very long accretion timescale, $\sim 1.4 \cdot 10^6\,s$. This different GRB event also impacts the expected BH mass from this progenitor. Contrary to cases a and d (see Section 6.2.5), the envelope is not ejected, and therefore I have to consider the 90% of the *total* mass of

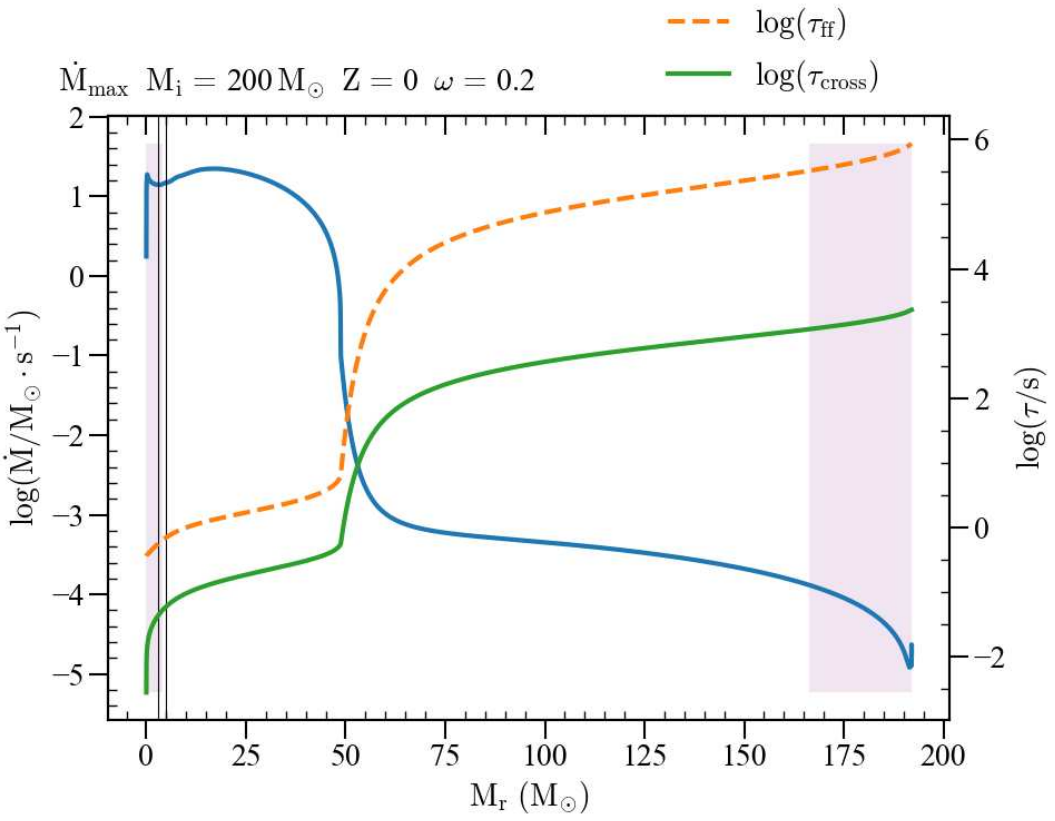

Figure 6.A.1: Same as in Figure 6.8. The two black vertical lines are at $3\,M_\odot$ and $5\,M_\odot$, respectively.

the model. This increases the mass of the black hole to $M_{BH} = 172.8\,M_\odot$.

On the other hand in the PPISN case, if I assume $M_{BH} = 5\,M_\odot$ then in this model there are no shells with enough angular momentum able to form an accretion disk. Hence, the whole stellar core should collapse into a BH.

Appendix 6.B GRB Analysis with improved moment of inertia

Here I show a different approach in the moment of inertia calculations for the shells in two different models (see in Figure 6.B.1). In Section 6.2.5, I evaluate the specific angular momentum profile averaging the inertia moment within each shell. I improve my analysis by splitting the integral for the moment of inertia into a polar region and an equatorial region as follows:

$$I_{\rm pol} = 2 \cdot 2\pi\rho \frac{R_1^5 - R_2^5}{5} \int_0^{\pi/4} \sin^3(\theta) d\theta, \tag{6.7}$$

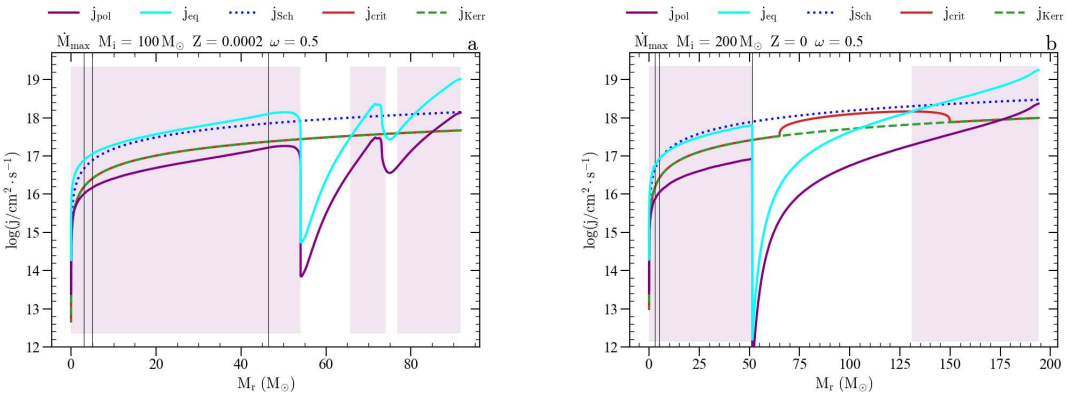

Figure 6.B.1: The two limiting cases in blue and green, the red curve, and the three vertical lines are as in Figure 6.7. In each panel, the purple line shows the specific angular momentum for the polar region, while the cyan line displays it for the equatorial region. I highlight in lilac where $j_{eq} > j_{crit}$.

$$I_{eq} = 2 \cdot 2\pi\rho \frac{R_1^5 - R_2^5}{5} \int_{\pi/4}^{\pi/2} \sin^3(\theta) d\theta, \tag{6.8}$$

with $\rho = \frac{3}{4\pi}(M_1 - M_2)/(R_1^3 - R_2^3)$ where M_1, M_2, R_1, and R_2 are the limiting masses and radii for the considered shell. The specific angular momentum profile is $j_{eq\,(pol)} = I_{eq\,(pol)} \cdot \omega/M$, where ω is the angular velocity and M the mass of the shell. In this way, in Figure 6.B.1 there are two different profiles for the specific angular momentum in the polar (purple) and equatorial (cyan) regions. As expected, we can see that $j_{eq} > j_{pol}$ since the angular momentum is more concentrated in the equatorial region.

To assess the possibility of a successful GRB, I have to consider two different aspects. First, whether the equatorial region has enough angular momentum to form a disk and therefore to launch a jet. Second, whether the material in the polar region collapses directly into the BH, thus favoring the jet propagation.

For every mass coordinate, there could be three possible scenarios, depending on the relations between j_{eq}, j_{pol} and j_{crit}. The best scenario for a successful GRB would be when $j_{eq} > j_{crit}$ and $j_{pol} < j_{crit}$. In this situation, we would have an accretion disk that powers the jet and no stellar matter that hampers its propagation through the poles. In the second scenario, both the equatorial and polar regions have enough angular momentum to prevent direct accretion onto the BH. Here the jet would not break out and therefore we could not have a successful GRB. Finally, we could have the case where both j_{eq} and j_{pol} are smaller than j_{crit}. In this case, the jet could not be launched since there would be no accretion disk.

I also checked that with this improved analysis, all my rotating models are still described by the four possible cases presented in Section 6.2.5. The results in Tables 6.3 and 6.4 are still valid except for the models ($M_i = 150\,M_\odot$, $Z = 0.0002$, $\dot{M}_{rdw}$, $\omega = 0.2$), ($M_i = 200\,M_\odot$, $Z = 0.0002$, $\dot{M}_{rdw}$, $\omega = 0.2$), ($M_i = 200\,M_\odot$, $Z = 0$, $\dot{M}_{max}$, $\omega = 0.2$), ($M_i = 200\,M_\odot$, $Z = 0$, $\dot{M}_{max}$, $\omega = 0.3$), and ($M_i = 200\,M_\odot$, $Z = 0$, $\dot{M}_{max}$, $\omega = 0.4$) that in the PPISN scenario should follow the b/c cases discussed in Section 6.2.5.

In Figure 6.B.1, I present two models already discussed in Section 6.2.5 to show the

differences with respect to the previous analysis (they are the models in Figures 6.7c and 6.7d, respectively). In panel a, the star undergoes PPI, so I have to consider only the stellar core. Here we see that the equatorial region has always enough angular momentum to form a disk. Instead, the material in the polar region should collapse directly into the BH. This is the most favorable scenario discussed above. On the other hand, in panel b I have to consider the whole star since this model should not experience PPI when I take $M_{He} = M_f$. Within the CO core, the situation is very similar to that in panel a. However, the presence of the stellar envelope should prevent the jet from breaking out.

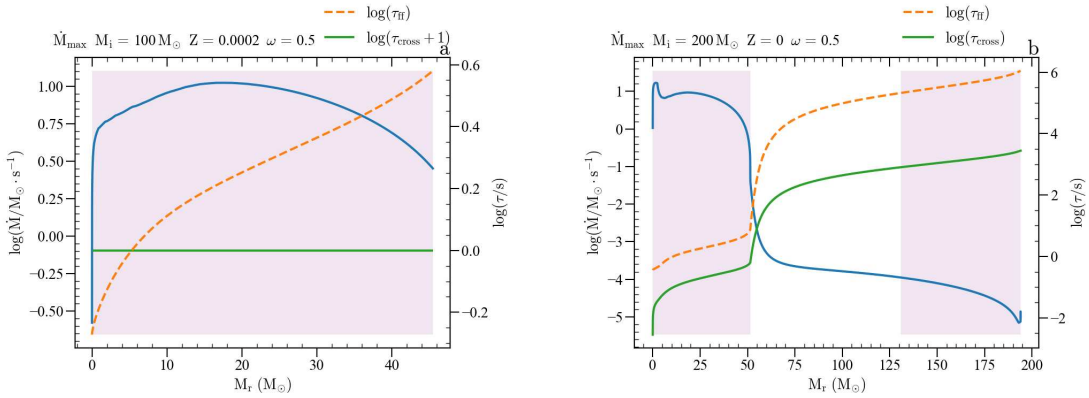

Figure 6.B.2: Same as in Figure 6.8, but the lilac regions refer to $j_{eq} > j_{crit}$.

Figure 6.B.2 shows the corresponding accretion rates, crossing timescales, and free-fall timescales. There are two main differences with respect to the models presented in Figure 6.8. Since I split each shell into a polar and an equatorial region, only half of the total shell mass can be accreted through the disk and power the jet. For this reason, the mass accretion rate is a factor of 1/2 lower. This implies a difference of ∼0.3 dex in $\log(L_{acc})$. The other difference is in the crossing timescale. All models present a smaller τ_{cross} for the jet powered by the inner core material. The difference is not that relevant because it does not change the outcome of the jet-driven event (e.g. $\Delta\tau_{cross} \sim 0.14\,s$ for the first jet in the model $M_i = 100\,M_\odot$, $Z = 0$, $\dot{M}_{rdw}$, $\omega = 0.2$). For models like the one in panel a, τ_{cross} is set to zero. The reason is that the polar region is devoid of matter, and thus the jet should freely propagate outward. Similarly, the second possible jet in models following Figure 6.7b should have $\tau_{cross} = 0$.

Appendix 6.C Interplay between pulsation-driven mass loss and rotation

Currently, no description of the interplay between rotation and stellar oscillations is included in PARSEC. However, it can easily be shown that such effects are negligible under the conditions we are interested in. Indeed, I only consider radial oscillations, which are unaffected by the centrifugal deformation (e.g. Saio 1981; Anderson et al. 2016). The magnitude of the remaining effects scales approximately as $(P/P_{rot})^2$, the squared ratio between the pulsation and rotation periods (Anderson et al. 2016). To assess the importance of such effects, the pulsation period can be approximated by the

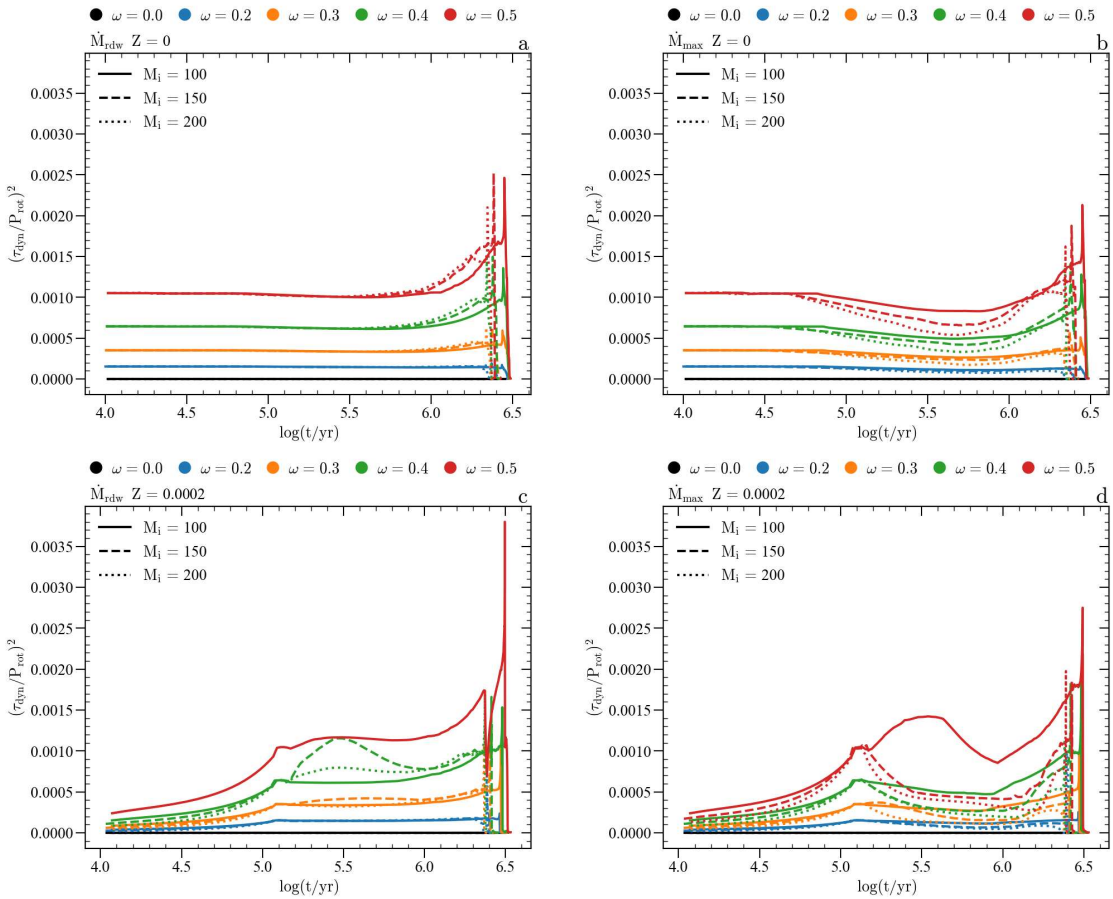

Figure 6.C.1: Squared ratio between dynamical timescale $\tau_{\rm dyn}$ and rotation period $P_{\rm rot}$ as a function of time (log(t/yr)) for all stellar models computed in this work. For simplicity and visualization convenience, these panels show $(\tau_{\rm dyn}/P_{\rm rot})^2$ from $t = 10^4$ yr after the beginning of the pre-main sequence until the end of computations. Different colors indicate different initial rotational velocities, while different line-styles refer to the three possible initial masses. The initial metallicity and the mass-loss recipe adopted in the sets are indicated at the top of each panel. The three possible initial masses are in units of $M_\odot$.

dynamical time scale $\tau_{\rm dyn} \sim \sqrt{R_*^3/2GM}$ (e.g. Catelan and Smith 2015).

Figure 6.C.1 shows the squared ratio between $\tau_{\rm dyn}$ and $P_{\rm rot}$ for all models considered in this work. We see that there is a consistent difference between $\tau_{\rm dyn}$ and $P_{\rm rot}$, with a maximum squared ratio of ~ 0.038 in panel c. The resulting effects should be within at most $\sim 0.4\%$, thus indicating that rotation and radial pulsations should not influence each other.

Appendix 6.D Fit formula by Mapelli et al. 2020

I adopt the fitting formula by Mapelli et al. (2020), which relies on models by Woosley (2017), to calculate the expected remnant mass of my models. The general expression for

the mass of the remnant is $\mathrm{m_{rem}} = \alpha_{\mathrm{P}}\, \mathrm{m_{no\,PPI}}$, where $\mathrm{m_{no\,PPI}}$ is the mass I would obtain without considering PPISN/PISN. In this work, I assume $\mathrm{m_{no\,PPI}} = 0.9\,\mathrm{M_f}$, to account for mass loss due to neutrino emission (see Fryer et al. 2012; Rahman et al. 2022, and references therein).

The fitting formula is a function of the helium core mass $\mathrm{M_{He}}$, the final mass $\mathrm{M_f}$, and the parameters F, K, and S defined as follows

$$F = \frac{M_{\mathrm{He}}}{M_{\mathrm{f}}},\ K = 0.67000F + 0.10000,\ S = 0.52260F - 0.52974. \tag{6.9}$$

Then, the coefficient α_{P} reads

$$\alpha_P = \begin{cases} 1 \quad \text{if } \mathrm{M_{He}} \leq 32\,\mathrm{M_\odot}, \forall\,\mathrm{F}, \forall\,\mathrm{S} \\ 0.2(\mathrm{K}-1)\mathrm{M_{He}} + 0.2(37-32\mathrm{K}) \quad \text{if } 32 < \mathrm{M_{He}/M_\odot} \leq 37, \mathrm{F} < 0.9, \forall\,\mathrm{S} \\ \mathrm{K} \quad \text{if } 37 < \mathrm{M_{He}/M_\odot} \leq 60,\ \mathrm{F} < 0.9,\ \forall\,\mathrm{S} \\ \mathrm{K}(16.0 - 0.25\mathrm{M_{He}}) \quad \text{if } 60 < \mathrm{M_{He}/M_\odot} < 64,\ \mathrm{F} < 0.9,\ \forall\,\mathrm{S} \\ \mathrm{S}(\mathrm{M_{He}} - 32) + 1 \quad \text{if } \mathrm{M_{He}} \leq 37\mathrm{M_\odot},\ \mathrm{F} \geq 0.9,\ \forall\,\mathrm{S} \\ 5\mathrm{S} + 1 \quad \text{if } 37 < \mathrm{M_{He}/M_\odot} \leq 56,\ \mathrm{F} \geq 0.9,\ 5\mathrm{S} + 1 < 0.82916 \\ (-0.1381\mathrm{F} + 0.1309)(\mathrm{M_{He}} - 56) + 0.82916 \quad \text{if } 37 < \mathrm{M_{He}/M_\odot} \leq 56,\ \mathrm{F} \geq 0.9,\ 5\mathrm{S} + 1 \geq 0.82916 \\ -0.103645\mathrm{M_{He}} + 6.63328 \quad \text{if } 56 < \mathrm{M_{He}/M_\odot} < 64,\ \mathrm{F} \geq 0.9,\ \forall\,\mathrm{S} \\ 0 \quad \text{if } 64 \leq \mathrm{M_{He}/M_\odot} < 135,\ \forall\,\mathrm{F},\ \forall\,\mathrm{S} \\ 1 \quad \text{if } \mathrm{M_{He}} \geq 135\mathrm{M_\odot},\ \forall\,\mathrm{F},\ \forall\,\mathrm{S}. \end{cases}$$

§Chapter 7

Conclusion

In summary, this Thesis concludes by providing a concise overview of its various components, each representing distinct stages of my doctoral exploration. Beginning with Chapter 1, I introduced a unique category of stars central to the two studies presented in this work. These stars exhibit distinctive traits, including a primordial chemical composition and an exceptionally high initial mass.

To explore this specific category of stars, I used the PARSEC code, employing it to compute various stellar evolution models. Chapter 2 then delved into our stellar evolution code, providing a comprehensive overview of its key aspects, beginning with the equations governing stellar structure and evolution.

Subsequently, in Chapter 3, I provided a concise historical overview of stellar pulsations, honing in on massive and very massive stars. The discussion then shifted towards the primary mechanisms governing stellar pulsations within this specific mass range, with a specific mention of the work by Nakauchi et al. (2020). Drawing from their research, the initial segment of this Thesis hinges on pulsation-driven mass loss in primordial very massive stars. I elucidated the integration of this novel mass loss mechanism into our PARSEC code, distinguishing between two distinct phases: the MS phase and the red-supergiant phase. In the former, radial stellar pulsations are propelled by the $\epsilon-$mechanism, while in the latter, the sustenance of pulsations is contingent upon the opacity of stellar matter, known as the $\kappa-$mechanism.

In Chapter 4, I elucidated the evolutionary pathways of primordial very massive stars, considering both radiation-driven winds and pulsation-driven mass loss, with a sensitivity to the Eddington factor Γ_e. These stars, initialized with masses of $100\,M_\odot$, $150\,M_\odot$, $200\,M_\odot$, $300\,M_\odot$, $500\,M_\odot$, $750\,M_\odot$, and $1000\,M_\odot$, were examined under two initial metallicity conditions: $Z = 0$ or $Z = 0.0002$. The interplay between the two distinct mass loss mechanisms manifests dominance at different phases of stellar evolution. Contrary to ex-

pectations for zero-metallicity or very-metal-poor stars, these models exhibit substantial mass loss—upwards of several tens or even hundreds of solar masses, particularly evident during the MS phase owing to pulsation-driven mechanisms.

I traced the evolution of these models from the zero-age main sequence until the initiation of the pair-creation instability, which occurs after the ignition of carbon, neon, or oxygen, contingent upon the star's initial mass. Models with an initial mass ranging between $300\,M_\odot$ and $1000\,M_\odot$ are anticipated to culminate in direct collapse into a black hole. Conversely, stars within the mass range $150 \leq M_i/M_\odot \leq 200$ are not expected to leave any remnants, as they are likely to undergo PISN. For lower mass models, the expectation is for PPISN or, in the scenario of zero-metallicity, the possibility of failed CCSN. In the latter case, the formation of black holes akin to the primary black hole observed in the gravitational wave event GW190521 ($M_{BH} \simeq 85\,M_\odot$) is in agreement.

Subsequently, in Chapter 5, I explored the importance of stellar rotation, as a pivotal process in stellar evolution. I outlined the key aspects of incorporating stellar rotation into the PARSEC code, drawing inspiration from the work of Costa (2019); Costa et al. (2019a,b)—for detailed technical insights, readers are referred to these sources. Stellar rotation influences both the structure and mixing processes within a star, consequently altering surface physical characteristics such as luminosity and effective temperature. Moreover, it impacts the duration of nuclear-burning phases and ultimately shapes the star's final destiny. Additionally, the relationship between rotation, angular momentum content, and the mass loss rate further underscores the interconnected nature of these factors. Geometric distortions induced by rotation facilitate the ejection of external layers, contributing to the removal of angular momentum from the stellar surface.

In Chapter 6, I explored the combined influence of stellar rotation and various mass loss mechanisms by introducing rotating stellar evolution models within the mass range $100 \leq M_i/M_\odot \leq 200$. I recalculated the models presented in Chapter 4, incorporating four different initial rotational velocities ranging from $\omega = 0.2$ to $\omega = 0.5$. Consequently, these models comprehensively consider the effects of pulsation-driven mass loss. This expanded set of calculations broadened the PARSEC parameter space, presenting, for the first time in the literature, models of rotating very massive stars encompassing both radiative winds and mass loss induced by stellar pulsations.

In this study, particular emphasis was placed on the ultimate destinies of these models, with a specific focus on the impact of stellar rotation leading to diverse jet-driven events within the collapsar scenario proposed by Woosley (1993). Models undergoing PPISN are anticipated to generate successful GRBs due to the absence of an extended stellar envelope in the progenitor. On the other hand, models undergoing DBH formation are expected to give rise to jet-driven supernovae, significantly influencing the mass of the resultant BH. In these cases, due to envelope ejection, the models should yield black holes within the pair-instability BH mass gap, consistent with those observed in the primary and secondary black holes of the GW190521 merger event. Various values for the accretion-to-jet efficiency were considered, leading to different expected luminosities for GRBs and jet-driven supernova events. This variability influences the detectability of successful GRB explosions by the Swift-BAT X-ray detector, while the observability of the afterglows produced by these progenitors should be attainable using current telescopes, such as the JWST.

To wrap up this study, an analysis was conducted on the progenitors under varying

assumptions regarding the initial BH mass and a distinct moment of inertia distribution for the polar and equatorial stellar regions. The outcomes remain largely consistent when considering different initial BH masses. However, in the latter scenario, where the moment of inertia is split between the polar and equatorial regions, the equatorial region plays a crucial role in the formation of the accretion disk—the engine of the jet-driven event. Meanwhile, the polar region influences the jet's propagation through the progenitor. In this context, the most favorable conditions for a successful GRB event involve a high specific angular momentum in the equatorial region, facilitating the generation of a powerful jet, and a low specific angular momentum in the polar region, promoting the collapse of that part of the star and facilitating the propagation of the jet through a hollow region.

These various investigations into primordial very massive stars could serve as a foundation for enhancing our comprehension of this specific stellar category. Future studies have the potential to expand the explored parameter space by augmenting the initial mass and, notably, by considering higher initial rotational velocities for the stellar models. Additionally, there is an opportunity to delve into more advanced phases of these stars' evolution, particularly focusing on models that are anticipated to result in failed CCSN.

Other physical processes could affect the evolution of my models, which I did not take into account in this Thesis. The first one, as mentioned in Section 6.3, is the presence of magnetic fields. They impact the evolution of massive and very massive stars in different ways. First of all, as already discussed, there is the transport of angular momentum from the core to the outer layers of the envelope. Magnetic angular momentum transport can impact the rotational velocity profile of the star, leading toward solid-body rotation, and thus slowing down the core of these models. This, in turn, could change the expected GRB event from these progenitors.

Magnetic field lines are very efficient in transporting angular momentum but also can play a big role in the rotational instabilities developing throughout the star. In this way, meridional currents increase and therefore affect the internal mixing of the different chemical species (Maeder and Meynet 2005). On top of this, two more factors can alter the evolution of this kind of stars: magnetic braking and mass loss quenching. The former is due to the higher loss of angular momentum through mass loss; while the latter is caused by the coupling of magnetic field with stellar winds. The magnetosphere of the star traps stellar matter, which eventually falls back onto the star. Therefore, this effect reduces the mass loss rate expected via stellar winds (Walder et al. 2012; Keszthelyi 2023). These effects could heavily impact the final mass of these models and thus the expected mass of the BHs formed by these progenitors.

The second process is the evolution of massive stars in a binary system. Binarity is a paramount aspect since the majority of massive stars are in binaries or higher-order multiples (e.g., Sana et al. 2012; Moe and Di Stefano 2017). The most impactful difference between single-stellar evolution and binary evolution is the possibility of mass transfer interactions. When and how these interactions take place are linked to the filling of the donor's Roche lobe and the expansion or contraction of the donor's radius with respect to its Roche lobe (Costa et al. 2023a). In turn, this stellar interaction is dictated by the evolution of stellar radii and how energy is transported through the stellar envelopes.

As one would expect, mass transfer impacts in a different way donor and accretor

stars. In the former, the helium core growth could be limited by envelope stripping and thus affect the final fate of the star. This depends on the evolutionary stage at which the first mass-transfer interaction occurs, along with its efficiency. The first interaction also depends on the stellar metallicity. For high-metallicity stars, this interaction should occur earlier due to the radial expansion of the star and with a higher efficiency due to the higher expected mass loss rates. In this case, the donor should become a WR star and produce a lower-mass compact object. On top of this, the degree of envelope stripping may affect the subsequent evolution of the binary such as the orbital separation and the possibility of unbinding the system.

On the other hand, mass accretion can significantly rejuvenate the accretor star, which can develop a bigger helium core. This could imply a higher mass compact remnant. The accretor also gains angular momentum therefore increasing its rotational velocity. However, the subsequent evolution of the star should be different compared to a faster rotating higher mass model computed within the single stellar evolution scenario. The reason is the different impact of the accretion on the stellar core, which could experience only in a partial way the mass and angular momentum gained by the external layers.

Effects other than the mass transfer interaction could be due to tidal forces and the emission of gravitational waves. The former ones reduce the eccentricity and set the stellar spins perpendicular to the orbital plane. The stars could even be tidally locked thus fostering a chemically homogeneous evolution. I do not find this chemically homogeneous evolution among my models but it could be crucial in yielding binary BH systems due to the reduced orbital separation.

In future studies, we will investigate the effects of both magnetic fields and binary evolution that can be crucial for these primordial very massive stars, especially for their expected remnants and GRB events. Another avenue for future exploration is the critical consideration of stellar opacity, as improvements in this aspect could not only alter the position of our models in the H-R diagram but also significantly impact internal structure and ensuing chemical mixing. Enhanced opacity might induce deeper or shallower DUP episodes, consequently influencing the evolution of the helium core and, in turn, substantially altering the final fate and expected remnant mass of these massive and very massive stars.

§Appendix A

A *python* routine to identify the critical points

A.1 Introduction

The critical points along a stellar track previously computed with a stellar evolution code (e.g. PARSEC), are of fundamental importance because they define sections of tracks that can be safely interpolated during the process of creating isochrones.

For stars with mass greater than $\sim 2\,M_\odot$, the total number of critical points that we define is 15, where the last one corresponds to the onset of thermal pulses during the AGB phase or the ignition of carbon in the core (see the $5\,M_\odot$ star in Figure A1). This last distinction depends on whether the initial mass M_i exceeds $\sim 8\,M_\odot$ or not. For stellar models with $M_i \lesssim 2\,M_\odot$ there are 6 or 11 critical points depending on whether the track reaches the end of the main sequence or not.

In the following sections, there will be a brief description of each critical point and how they are found in the routine, in order to provide for them a more righteous stellar

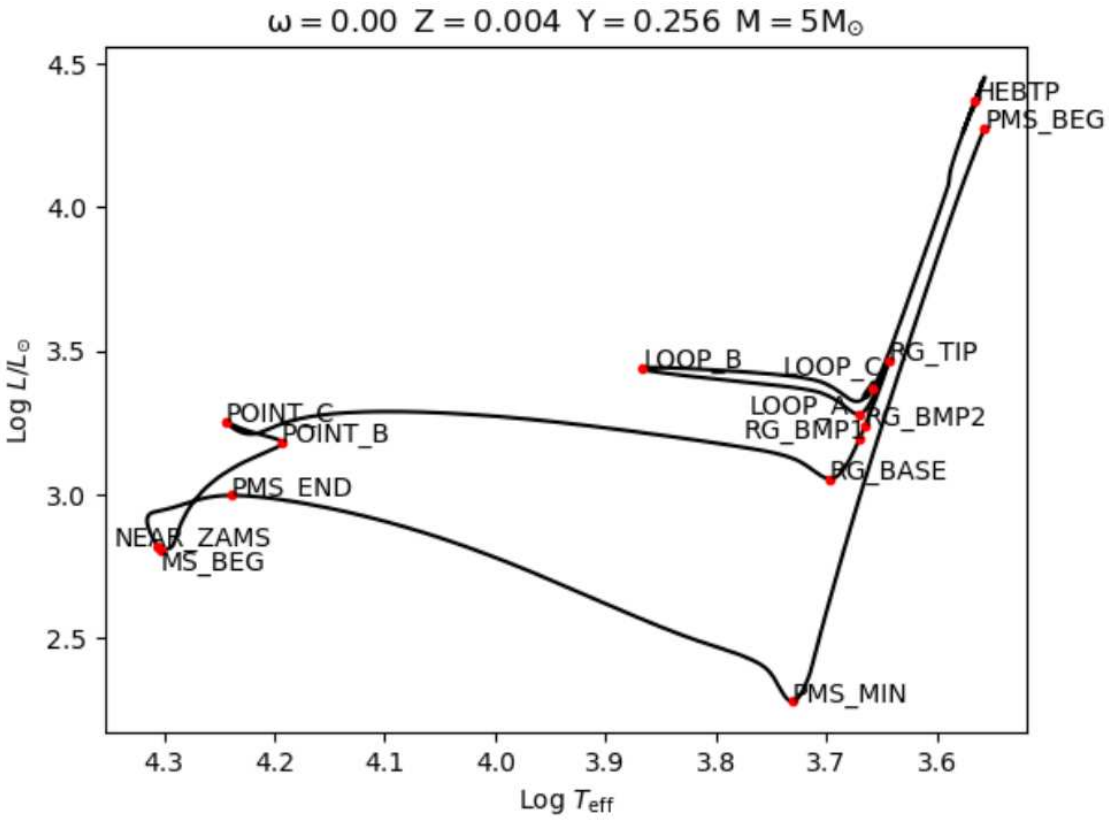

Figure A1: HRD of a $5\,M_\odot$ Z = 0.004 model. The evolution starts at the PMS phase and ends at the first thermal pulse during the AGB phase. For this intermediate-mass star, there are 15 critical points highlighted in red.

evolutionary context besides the mere python code one.

A.2 Beginning of the pre-main sequence phase

The first critical point, PMS_BEG, corresponds to the first model along the track which has an age bigger than 0.2 yr, since before that there are some fictitious models generated by the stellar evolution code.

Then there is the first definition of the critical point PMS_END, though it will be found later on in the code. This point corresponds, now, to the last model which has a central temperature $T_c > 10^6\,K$ and the luminosity due to gravitational contraction $L_{grav} > 60\%\,L_{tot}$, this index is referred to as ipms.

Before going on with the other critical points, there is a very important step where the code defines the end of each track in the set. This is done to search for critical points only up to this model. The point tra_end will be useful also in the definition of the last critical point for intermediate and massive stars. The first differentiation, only for those tracks that have an initial mass $M < 8\,M_\odot$, is whether or not the last model available has a central helium abundance Y = 0. If this is the case, models with Y = 0 and the luminosity due to the carbon burning, with respect to the total one, $L_C > 3$

are considered, where the total number of such models is cnt1. Then, also models with $Y = 0$ and $L_C > L_\nu$ are taken into account, where L_ν is the neutrino luminosity, with cnt2 the total number of these models. If any of these two counts, cnt1 and cnt2, is non-zero, then tra_end is defined as the first model with the characteristics described above.

In the case where we have both cnt1 and cnt2 bigger than zero, then tra_end is the maximum between the first models that have $L_C > 3$, $Y = 0$ and $L_C > L_\nu$, $Y = 0$. For stars that have both cnt1 and cnt2 equal to zero, I consider models with $Y = 0$, $L_Y > 3$, L_Y being the luminosity due to helium burning, and $M_{CO} > \frac{3}{4} M_{He}$. If there are models with these properties, then tra_end is the first one among them. Instead, if there is not at least one model like this, then tra_end is set to the last model available for the track.

The same definition of tra_end is applied to those tracks that have an initial mass $M \geq 8\,M_\odot$ or $Y > 0$ for the last model available, i.e. those tracks that do not fulfill the first differentiation.

Finally, there is one last case: if the initial mass of the star $M < 3\,M_\odot$, then is considered the final hydrogen abundance at the center of the star. If this latter is zero, the code looks for those tracks that are still burning helium in the last model available: for this kind of stars tra_end is set to the last model with $X > 0$.

A.3 Beginning of the main sequence phase

To find the beginning of the main sequence phase, MS_BEG, the arrays with the differential increment in x and y axis of the HR diagram are created from those with the logarithm of the effective temperature T_{eff}, logte, and the logarithm of the luminosity $L/L_\odot$, logl. This differential increment reads

$$dx = \frac{\log(T_{eff})[1 : nmod] - \log(T_{eff})[0 : nmod - 1]}{\max(\log(T_{eff}) - \min(\log(T_{eff})}, \tag{A.1}$$

where nmod is the last index of the array here considered and this goes as well for the array dy derived from logl.

Having found dx and dy, the derivative of the position in the HR diagram is

$$ds\_dt = \sqrt{(dx^2 + dy^2)}/dt, \tag{A.2}$$

where dt contains the time step for each model.

Now I take the minimum in ds_dt, dmin, but considering only models after the possible end of the pre-main sequence phase, meaning after ipms, where the central hydrogen abundance is higher than $X_i - 0.2$, with X_i the initial hydrogen abundance. Then, the beginning of the main sequence phase is the last model before dmin where ds_dt is ten times larger than dmin. This procedure is followed first for those tracks that during their evolution deplete hydrogen in their core and then for those that do not complete the main sequence. In this latter case, the only difference is that the model for the beginning of the main sequence is still chosen among those that have a ds_dt value ten times bigger than dmin, but it is not simply the last one. It is the last model for which ds_dt is bigger than all models that follow. Before the next critical point, two

arrays are calculated as follows

$$\mathrm{dl\_dt} = \frac{\mathrm{dy}}{\mathrm{dt} \cdot \max(\mathrm{dt})} \tag{A.3}$$

$$\mathrm{dte\_dt} = \frac{\mathrm{dx}}{\mathrm{dt} \cdot \max(\mathrm{dt})}, \tag{A.4}$$

which are the time derivatives for luminosity and effective temperature.

A.4 Critical points in pre-main sequence phase

Here I consider all models between the PMS_BEG critical point and the index ipms. First of all, the first model with central temperature T_c greater than 10^6 K is found (i.e imin1), and then the code searches for the minimum luminosity among all models up to imin1. If this minimum occurs before the luminosity minimum of all models up to ipms, then it is set to this latter value. Moreover, if this is the case ipms is reset to the model with the maximum luminosity, imaxlum, if this latter occurs later than the overall minimum and before ipms.

Finally, there is one last check: if the index corresponding to the minimum luminosity is exactly ipms, then is set to the last model with central temperature T_c lower than that corresponding to the luminosity minimum of the previous track analyzed. So with this procedure are found the two critical points PMS_MIN and PMS_END.

A.5 Point B during the main sequence phase

To find this critical point, stellar tracks are divided into different cases according to the properties of their evolution.

The first differentiation is whether or not a star reaches a central hydrogen abundance $0 < X < 0.4$; if this is not the case, then POINT_B corresponds to the last model of the track. This situation occurs for very low mass stars, approximately with a mass $M \lesssim 0.5\,M_\odot$. For the positive case, the second differentiation is whether or not there are models with the central hydrogen abundance $0.001 < X < 0.4$, the luminosity due to contraction of the star $L_{grav} > 0$ and a mass of the convective core, given by Schwarzschild criterion, $Q_{SCHW} > 0$. Then, assuming that there are some models with these characteristics and that they are grouped in an array, it is considered the first such model with its index being not consecutive with respect to that of the following model in the array. From this one, namely ipb, are considered models with an effective temperature T_{eff} lower than that of ipb, but only in a range of 50 indexes from ipb, with this latter included. Finally, POINT_B is the model with the minimum effective temperature among these, but only in the case that $X < 0.05$ for this model, otherwise POINT_B becomes the last model with $X \geq 0.05$.

In the case where the track never fulfills the requirements in the second differentiation, then ipb is set to the last model with the luminosity due to hydrogen core burning $L_x > 0.5$. Here there are two different sub-cases: if ipb has a hydrogen central abundance $X \leq 0.05$, then POINT_B is the first model with $X \leq 0.05$; instead, if at ipb $X > 0.05$, then POINT_B is the last model with $X \geq 0.05$.

A.6 The NEAR_ZAMS critical point

For stellar tracks with an initial mass M $>$ 5, the effective temperature and the stellar luminosity at the end of the pre-main sequence phase, ipms, and at POINT_B, ipb, are stored in different variables, respectively $\mathbf{x_a}$, $\mathbf{x_b}$ for T_{eff} and $\mathbf{y_a}$, $\mathbf{y_b}$ for the luminosity. Then, is considered the effective temperature of all models between ipms and ipb, and the core stores these values in the xxx array. The next step is to calculate the luminosity corresponding to this temperature array with the following interpolation

$$yyy = y_a + \frac{y_b - y_a}{x_b - x_a}(xxx - x_a). \tag{A.5}$$

With this new array yyy, the point NEAR_ZAMS, ilmin, is the model for which yyy[i]-log(L)[i] is maximized, where i is the index of the model.

Instead, for stars with M $\leq$ 5, only those models with X $>$ 0.2 are considered. Here ilmin is the minimum luminosity among those models; if ilmin occurs after the fourth model before the beginning of the main sequence phase, imsbeg, then ilmin is set to imsbeg-4. In the case where ilmin $<$ ipms+2, meaning before the second model after the end of the pre-main sequence phase, ipms is set to ilmin-2 and NEAR_ZAMS remains ilmin.

After this critical point, the code skips the research for the following ones for stars that don't deplete the hydrogen in the core, therefore stellar tracks that have an incomplete main sequence phase have only 6 critical points.

A.7 Point C during the main sequence phase

Here are considered models, after ipb, with T_{eff} greater than that of POINT_B; then ipc, the index for the critical point POINT_C, is set to that model among these with the maximum T_{eff}. If there is not at least one model with the characteristics described above, then for this critical point I take the first model which has X = 0. Finally, if neither of these is the case, then POINT_C coincides with the last model for the track, i.e. tra_end.

A.8 The tip of the red-giant branch: RG_TIP

For this critical point, the stellar tracks are divided into three categories. For those that do not extinguish helium in their core, RG_TIP, with index itip, is the model with the minimum effective temperature between the beginning of the main sequence and tra_end. For those that do extinguish helium, models with a central helium abundance Y $>$ 0.9 $-$ Z are considered, where Z is the initial metallicity of the star. In this case, RG_TIP coincides with the minimum T_{eff} among those models. The last possible kind of track in the research of this critical point is a track that has an incomplete main sequence phase, i.e. a very low-mass star. For this kind of tracks, RG_TIP is set to tra_end.

A.9 The base of the red-giant branch: RG_BASE

First of all, in this section, I consider all models in the tracks between ipc and itip, with the latter being included while the former is not. Once I have both the luminosity and the effective temperature for each one of these models, with all these values stored respectively in the l_ and te_ array, I use the following relation to compute the array dist2

$$\mathrm{dist2} = \frac{|\mathrm{l\_} - \log(\mathrm{L})[\mathrm{ipms_min}]|}{|\max(\mathrm{l\_}) - \min(\mathrm{l\_})|} + \frac{|\mathrm{te\_} - \log(\mathrm{T_{eff}})[\mathrm{ipms\_min}]|}{|\max(\mathrm{te\_}) - \min(\mathrm{te\_})|}, \tag{A.6}$$

where the minimum of this latter is stored in the variable irgbb.

Then in iminrgbl and aveteff are stored the index of minimum luminosity among these models and the index of average T_{eff}, respectively. If iminrgbl > 0, the corresponding minimum luminosity is lower than log(L)[irgbb] and the corresponding T_{eff} is lower than the average one, then irgbb is set to iminrgbl. After that, there is a check performed only for low-mass stars, i.e. those stars that do not extinguish helium in their core. Here, models with QDISC > 0 and X $= 0$ are taken into account, where QDISC is the fractional mass, normalized to the total value, of the first mesh point in the stellar track where the chemical composition changes with respect to the stellar surface, i.e. the end of the external envelope of the star in mass coordinate. Then, the minimum QDISC value for these models is calculated, i23, and irgbb is set to the minimum between irgbb and i23. The final step for this critical point is to check whether or not irgbb is a "false" red-giant branch base. If $\log(T_{eff}) > 3.9$ or $L_Y > 0.99$, then the red giant branch base is too hot and so irgbb is set to itip-20. In this latter case, RG_BASE is "false", while in all the other possible cases the critical point RG_BASE set to irgbb is a real feature of the stellar track.

A.10 Luminosity bumps during hydrogen shell burning

For this critical point, the first distinction is whether or not a star is a low-mass star (see for example the $0.8\,M_\odot$ model in Figure A2), i.e. whether or not it extinguishes helium in its core. If this is the case, we consider models between irgbb+1 and tra_end with an helium core mass $0.1\,M_\odot < M_{He} < 0.4\,M_\odot$. After that, among these models is selected the first one that has a greater luminosity compared to those that follow and those that precede. The index of this model is indicated as isearchbump. If this latter is either zero or bigger than itip then it is set to (itip + irgbb)/2 and the index of the first bump, irgbbp1, is set to isearchbump. The next step is to consider models after the first bump with a luminosity $\log L < \log L[\mathrm{irgbbp1}] + 0.1$. The irgbbp2 index, corresponding to the second bump, is then set to minimum luminosity for these models. If irgbbp2 is not the following model with respect to irgbb1, then the second bump is kept to irgbbp2, while in the other possible case, irgbbp2 is irgbbp1 plus the difference between irgbbp2 and irgbbp1 for the previous track. Finally, for this kind of stars, an additional check. If there is not a single model such that $\mathrm{dl\_dt}[\mathrm{irgbbp1} + 3 : \mathrm{irgbbp2}] < 0$, then irgbbp2 is set to irgbbp1+10. In the opposite case, the index irgbump1 is set to the first model with those characteristics. Having irgbump1 smaller or equal to irgbbp1+3, irgbump1 takes the value of irgbbp1, otherwise irgbump does not change. Now I take into account those models after irgbbp1+3 that have dl_dt < 0 and L $<$ L[irgbump1]. If the track

does not have any of such models then irgbump2 = irgbbp2, otherwise irgbump2 is the last model among these. After that, irgbbp1 = irgbump1 and irgbbp2 = irgbump2, but this latter only if the luminosity of irgbump2 is smaller than that of irgbbp2.

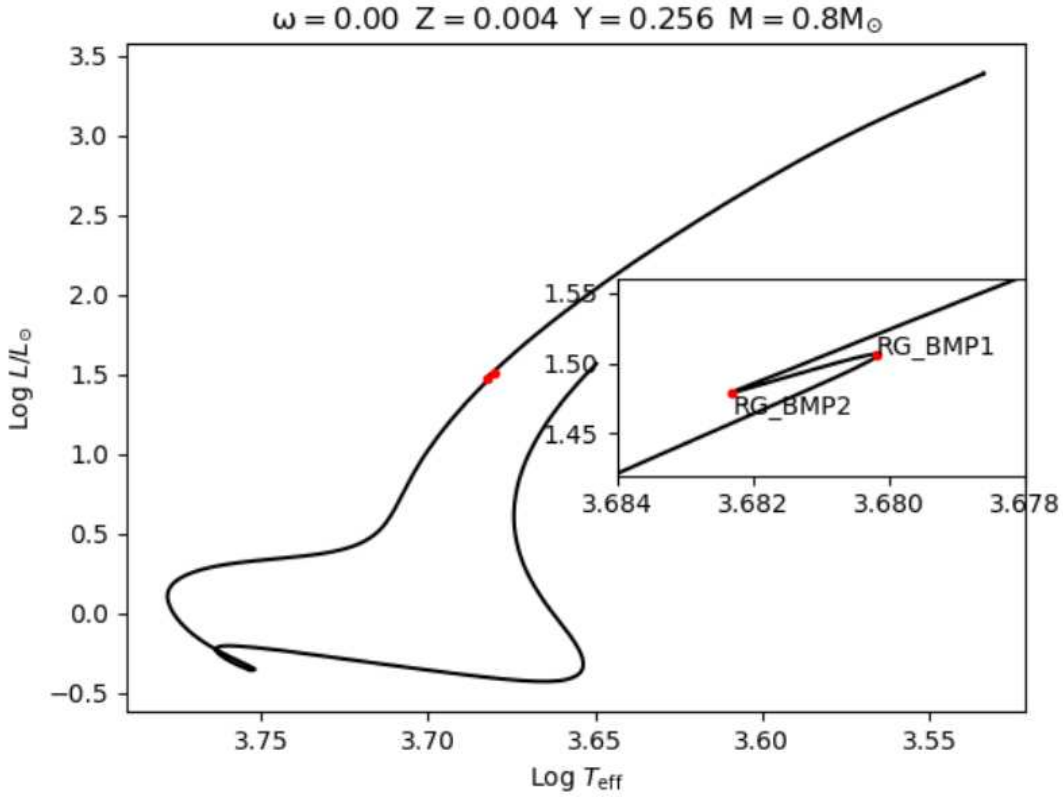

Figure A2: HRD evolution of a stellar track with $M_i = 0.8\,M_\odot$ and Z = 0.004. The inset shows the temporary decrease in luminosity when the h-burning shell crosses the hydrogen discontinuity left by the first DUP episode.

The research for luminosity bumps now continues for intermediate and massive stars, if they do not have a false red-giant branch base. The index isearchbump is found in the same way as before. In the case that isearchbump is larger or equal to itip then it is set to (itip + irgbb)/2, but if isearchbump is not found, i.e. it is equal to irgbb+1, then this index becomes the first model, after irgbb+1, with a luminosity larger than l_med; with this latter computed as follows:

$$\text{l\_med} = \log(\text{L})[\text{irgbb}] + \frac{\log(\text{L})[\text{itip}] - \log(\text{L})[\text{irgbb}]}{3}, \tag{A.7}$$

and eventually, irgbbp1 is set to isearchbump. Moreover, now following what has been done for lower mass stars, irgbbp2 is set to the minimum luminosity between irgbbp+1 and itip. If irgbbp2 is not the following model with respect to irgbbp1 then we keep its value, otherwise, irgbbp2 is equal to irgbbp1+1+dirgbbp, where this latter is equal to:

$$\text{dirgbbp} = \min\left\{5, \max\left[\left(\frac{\text{itip} - \text{irgbbp1}}{2}\right), 1\right]\right\}. \tag{A.8}$$

After this, there are two last checks: if irgbbp2 coincides with itip then irgbbp2 = itip-1, and if irgbbp1 = irgbbp2 then the previous one is set to irgbbp2-1. Finally, for intermediate and massive stars that have a "false" red-giant branch base, irgbbp1 is equal to itip-12 and irgbbp2 is itip-8.

A.11 Blue-loop during CHeB

Three different points characterize this evolutionary phase of intermediate and massive stars: LOOP_A, LOOP_B, and LOOP_C. First of all it's found the last model with X = 0 and Y > 0.1, imx, and then the index of minimum luminosity and maximum effective temperature for those models between itip+1 and imx, minl, and mxte respectively, with ltmax as the luminosity of this latter. If minl > mxte, minl is set to the index of minimum luminosity between itip+1 and mxte and the flag lmin_before_tmax is set to false. After that, all models between itip+1 and imx with a luminosity smaller than that of imx are considered, where the first one among these is called istart. If this latter does not coincide with itip+1, then the following search is performed for all models between istart and minl. Each one of these models is considered singularly inside a "for loop": with respect to model j, those between itip+1+j and imx with a luminosity bigger than L[j] are taken into account. Then, the first one of these is called ipara and it is computed the following:

$$\mathrm{dt} = \log(\mathrm{T_{eff}})[\mathrm{ipara}] - \log(\mathrm{T_{eff}})[\mathrm{j}]. \tag{A.9}$$

The indexes ipm1 and ipm2 are set to respectively j and ipara if dt is bigger than maxdt, which initially is set to a negative value, and if this is the case, maxdt = dt at the end of the iteration. In this way, when the "for loop" is over, ipm1 and ipm2 are the two models with the biggest difference in effective temperature where ipm2 is the first model that has a luminosity bigger than that of ipm1. A first check on ipm2 follows: if mxte > ipm2 and ltmax > $\log(\mathrm{T_{eff}})[\mathrm{ipm2}]$, then ipm2 is set to mxte. A second check on ipm1 and ipm2 is performed after that: if $|\mathrm{ipm2} - \mathrm{ipm1}| < 10$ or $\max(\log(\mathrm{T_{eff}})[\mathrm{itip}+1:\mathrm{imx}]) - \log(\mathrm{T_{eff}})[\mathrm{ipm2}] > 0.2$, then ipm2 is set to the model with maximum effective temperature between itip+1 and imx, minl is now the index of the minimum luminosity between itip+1 and ipm2 and finally even ipm1 is reset. If there are models between itip+1 and minl that have a luminosity smaller than that of ipm2, then ipm1 is the first one among such models, otherwise, ipm1 is set to minl/2.

Another "distance" in the HR diagram is now computed as follows:

$$\begin{aligned}\mathrm{dt2} = &\left[\frac{\log(\mathrm{L})[\mathrm{minl}+1:\mathrm{imx}] - \log(\mathrm{L})[\mathrm{ipm1}]}{\max(\log(\mathrm{L})[\mathrm{minl}+1:\mathrm{imx}]) - \min(\log(\mathrm{L})[\mathrm{minl}+1:\mathrm{imx}])}\right]^2 + \\ &+\left[\frac{\log(\mathrm{T_{eff}})[\mathrm{minl}+1:\mathrm{imx}] - \log(\mathrm{T_{eff}})[\mathrm{ipm1}]}{\max(\log(\mathrm{T_{eff}})[\mathrm{minl}+1:\mathrm{imx}]) - \min(\log(\mathrm{T_{eff}})[\mathrm{minl}+1:\mathrm{imx}])}\right]^2.\end{aligned} \tag{A.10}$$

The index corresponding to the minimum of dt2 is then called ipm3. This index ipm3 is useful in the following check: if the flag lmin_before_tmax is false, minl1 corresponds to the index of minimum luminosity between ipm3 and imx, if minl1 is bigger than ipm3, then this latter is set to minl1 and if ipm2 > minl, then minl and ipm2 are switched. After this check, ipm3 is set to the first model with Y = 0 and two final checks are

performed: if minl coincides with itip then minl is set to itip+2 and if minl $\geq$ ipm2 then ipm2 is set to minl+5.

Finally, having minl, ipm2, and ipm3 these three indexes correspond respectively to the critical points LOOP_A, LOOP_B, and LOOP_C.

A.12 Final critical point: TPAGB or C_BUR

For this last critical point, the definition of tra_end that we saw earlier in §A.2 now comes in handy. The critical point C_BUR is set to tra_end if there is at least one model within the track with a luminosity due to carbon burning $L_C > 3$ and $Y = 0$, otherwise to the index tra_end corresponds the critical point TPAGB. These two different cases correspond to massive and intermediate-mass stars, respectively. There is an exception regarding intermediate-mass stars, for which the last critical point is set to HEBTP, where this latter stands for helium before the thermal pulse. If the current track has at least one model, after the end of core helium burning, with the luminosity due to helium burning $L_Y > 2$ and $L_Y > 3 \cdot L_X$, where L_X is the luminosity due to hydrogen burning, then a thermal pulse is present. HEBTP is set to the last model with $L_Y < 3 \cdot L_X$ before the first thermal pulse in the track.

A.13 Critical points for WR stars

If a massive star, initial mass $M > 10\,M_\odot$, has a ratio between initial and final mass below 0.8 and reaches an effective temperature $\log(T_{eff})[\text{tra\_end}] > 4.5$ (and also is not the only one with these characteristics in the set), then it is considered a WR star. This kind of stars is treated differently from the others, and so the critical points of a WR star are not the same as those seen so far, except for PMS_BEG, MS_BEG, and C_BUR.

A.13.1 Critical points in pre-main sequence phase

During the pre-main sequence phase, the same two points, PMS_MIN and PMS_END, are found. In this case, the definition of the previous one, imin, is simply the minimum luminosity along the track before ipms, with this latter included. If PMS_MIN coincides with the beginning of the pre-main sequence phase, then imin is set to ipms/4. PMS_END holds the definition of the end of this phase that we found above.

A.13.2 Point B and Point C

For a track that eventually becomes a WR star, the two points described above after the beginning of the main sequence, POINT_B and POINT_C, are computed with a slightly different definition. Here POINT_B is set to the last model with $X > 0$, while POINT_C, with index ipb1, is the first model that has $X = 0$, $Y > 0$ and $L_Y > 0.01$.

A.13.3 Critical points HE_HE and He_08

The index ipb2 refers to the last model with $X = 0$, $Y > 0.8$ and $L_Y > 0.01$. If $\text{ipb2} - \text{ipb1} < 10$, then the new value for ipb1 is ipb1-6, while ipb is set to ipb2-3; otherwise, in the other possible case, minipb is set to the index of minimum effective

temperature between ipb1 and ipb2. If minipb $>$ ipb $+ 3$ and minipb $<$ ipb2 $- 3$, then ipb is minipb, else ipb is (ipb1 + ipb2)/2. Having ipb and ipb2, these two indexes correspond to the critical points HE_HE and He_08, respectively.

A.13.4 Other critical points during CHeB

There are 6 other critical points regarding this type of track, bringing the total number of critical points to that found for intermediate and massive stars.

Namely they are He_06, He_05, He_04, He_02, He_01 and He_001. The first three are found as the last model in the track that has X $= 0$, $L_Y > 0.01$ and, respectively, Y > 0.6, 0.5 or 0.4. For the last three, instead, the first two conditions are the same, while the third one is, respectively, Y < 0.2, 0.1 or 0.01, where the critical point is set to the first model with these characteristics.

So, all the possible tracks inside a set have now been processed and all critical points available for each track have been found; this leaves us with an output file that shows all the critical points found for each track in an ordered table.

A.14 Critical points for HB stars

In the code, there is another section separated from the main one, other than that regarding WR stars. Here the focus is on stars in the so-called HR diagram horizontal branch. These are low-mass stars that successfully evolve beyond the helium-flash and after that start to burn helium in a non-degenerate core. This HR diagram feature is explained by the fact that all low-mass stars start to burn He with approximately the same core mass, hence the luminosity during this phase is almost entirely independent of the initial mass of the star. To properly model the evolution of a low-mass star through the helium flash and the consequent helium burning, the evolution of this kind of stars is resumed after the flash with a stellar track that burns helium in its core having a smaller total mass, since the experienced mass loss during the Red-Giant phase.

The first critical point, He1, is set to the first available model in the track, which corresponds to the beginning of the core helium burning phase. Then, there are eight critical points, He0.5, He0.4, He0.3, He0.2, He0.1, He0.01, He0.001 and He0, that refer to the last model where the central helium abundance is greater than 0.5, 0.4, 0.3, 0.2, 0.1, 10^{-2}, 10^{-3} and 10^{-5}, respectively. Finally, the last critical point in this kind of tracks is HEBTP as defined in §A.12, or, in case this latter can not be found, it is the last available model, which is labeled HeLST.

A.15 Input files for TRILEGAL and IDL

In the following, the two main possible output files of the code are described, which then can be used as input files for isochrones computing codes such as TRILEGAL (Girardi et al. 2005; Marigo et al. 2017) and an IDL routine. The main difference between the two possible formats of the output files is the number of models that are written for each track. To select those models that are going into the final file is used the function "compute_selmods", whose main task is to return the selmods array containing the

indexes of the selected models. Through the parameter "shstep" it is possible to set how many models will be in the output. The variable "nsteps" is computed as

$$\text{nsteps} = \frac{\max(\text{sh})}{\text{shstep}}, \tag{A.11}$$

where sh is the cumulative sum of the derivative of the position in the HRD during the track's evolution. So, by increasing or decreasing shstep you can decrease or increase the number of the models in the output respectively. Then, if nsteps is smaller than the total number of models present in the track, the array selmods is calculated with a linear interpolation as

$$\text{selmods} = \text{np.interp}(\text{shvals}, \text{sh}, \text{tmd}), \tag{A.12}$$

where shvals = shstep ∗ np.arange(nsteps) and tmd = np.arange(nmod), with "nmod" corresponding to the model of the last critical point.

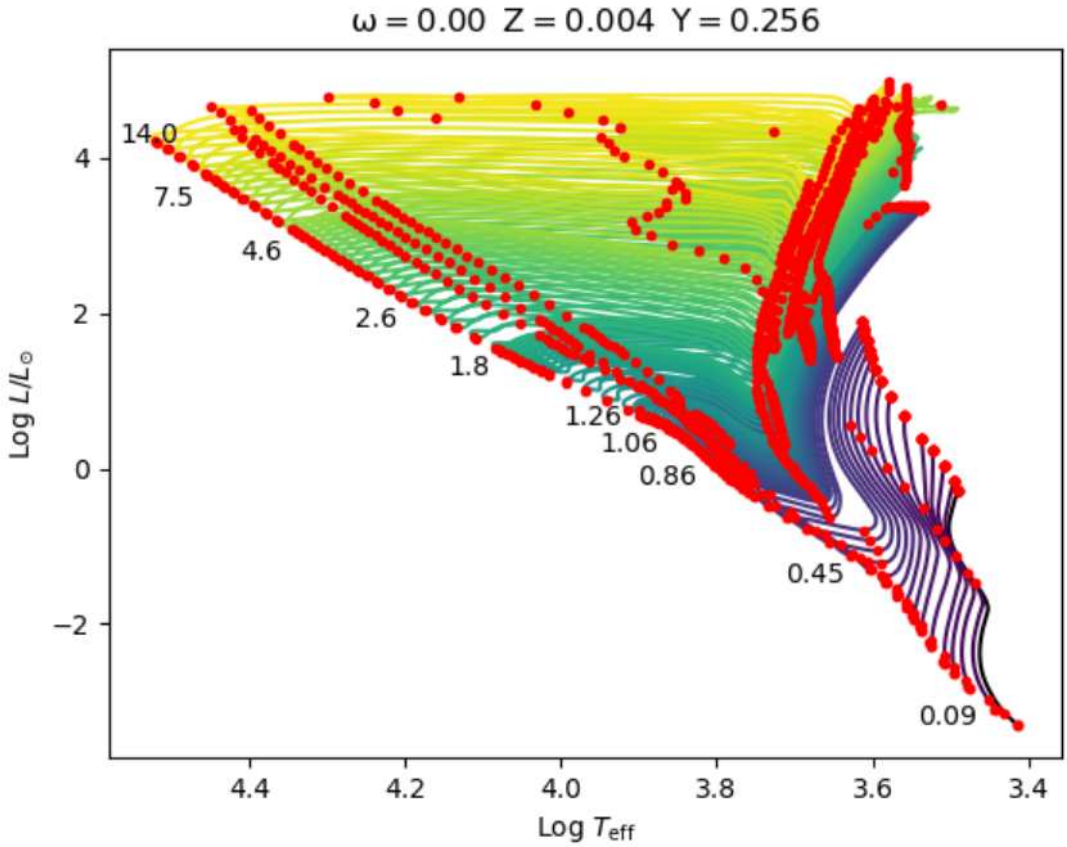

Figure A3: HRD with a set of 91 stellar tracks by Nguyen et al. (2022). The diagram shows the evolution from the PMS until carbon ignition, the first thermal pulse in the AGB, the helium flash, and the end of the MS for massive, intermediate, low, and very low-mass stars, respectively. In red, there are the critical points found for each track in the set. Numbers indicate the initial mass in $M_\odot$ of 10 selected stellar tracks.

Having computed selmods for each track in the current set, you can choose the format of the output file setting the parameters "trilegal" or "idl" to true. In the first case,

usually, shstep is 0.017, while for the latter is 0.004. For TRILEGAL there are three possible formats: default, rot, and sismo. For each one of these, you can choose to create the file INT2, LOW2, or HB2 or instead INT, LOW, or HB for IDL format.

If you choose this latter then in the file INT will be printed a total of 24 columns, from the F7 file, including data about nuclear abundances and rotation-correlated quantities, for each model present in the selmods array for all the tracks in the set. As preliminary information in the first lines of the output, there are the numbers of very low, low, intermediate, massive, and very massive stars in the set; the number of models in the selmods array for each track, and also their masses. After the last model of the last track, there is the total number of critical points found for each track (see Figure A3 for a visual example) and the models in selmods corresponding to these critical points. Finally, the He core mass at the beginning of the thermally pulsing AGB phase is printed for all tracks with kind=3. The LOW and HB files are very similar to INT, but in the former, only very low and low tracks are present, while in the latter there are only HB tracks.

The rot format (for INT2, LOW2, and HB2) of TRILEGAL is quite similar to the INT output of IDL, except for the number of models that are written; while the default format contains only 11 columns without any information on nuclear abundances and rotation.

§Appendix B

Algorithm for isochrones

B.1 Introduction

Given a set of tracks of masses M_i, with $i = 1, 2, 3, \ldots$, we have information about stellar properties (L, T_{eff}) along vertical lines in the age versus mass diagram of Figure B1. The problem of making isochrones is that of deriving the same information for an arbitrary horizontal line, of age t_0, in this diagram.

The interpolation of L and T_{eff} is better (and easier) if performed between points of equivalent evolutionary stage located on two neighboring tracks. Thus, it's convenient to change the representation and use the "evolutionary stage" versus mass diagram in Figure B2.

Isochrones in this diagram run diagonally. The intersection of an isochrone t_0 with any evolutionary track is straightforward to find (dots in the figure). This already gives you some (very few) points in the isochrone. The problem, instead, is to derive interpolations of L and T_{eff}, for a given age t_0, between any pair of equivalent evolutionary points.

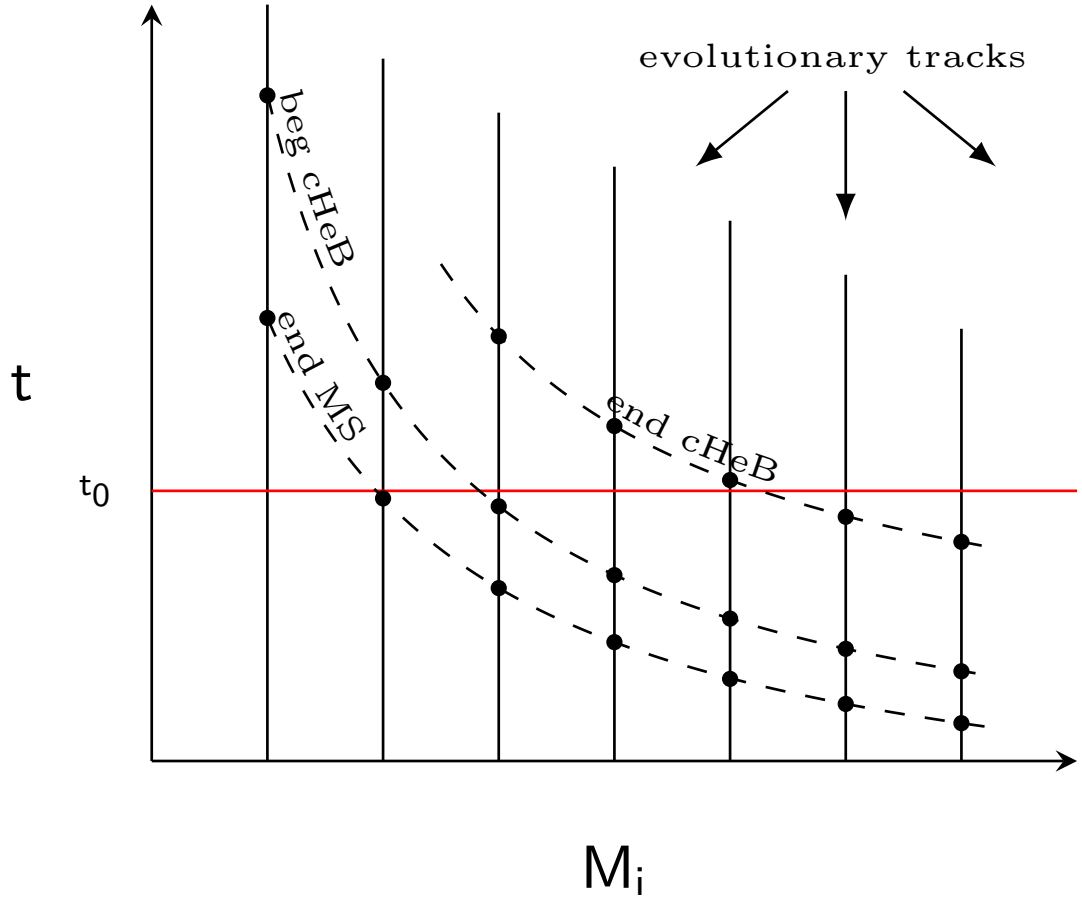

Figure B1: Age versus mass diagram with 7 stellar tracks. The red horizontal line at t_0 represents an example of isochrone. The black dots along each dashed curve show equivalent evolutionary points for the end of the MS, the beginning of helium burning, and the end of cHeB.

B.2 Defining equivalent evolutionary stages

The important evolutionary stages are the points j, with $j = 0, 1, 2, 3, \ldots$. They can be, for instance, points of maximum and minimum L and/or T_{eff} along the tracks. The end of the MS phase (with central X=0) is an important stage and defined for all tracks. Other important stages are the points of maximum and minimum T_{eff} during the overall contraction phase at the end of the MS, but they can be defined only for stars with $M > 1.1M_{\odot}$. This is not a problem, as we'll see later.

Once you have defined the important stages, you should isolate, one at a time, the squares drawn in the plane of Figure B2. Every square is limited by: two adjacent tracks i and i+1, of masses M_i and M_{i+1} and two subsequent evolutionary stages, j, and j+1.

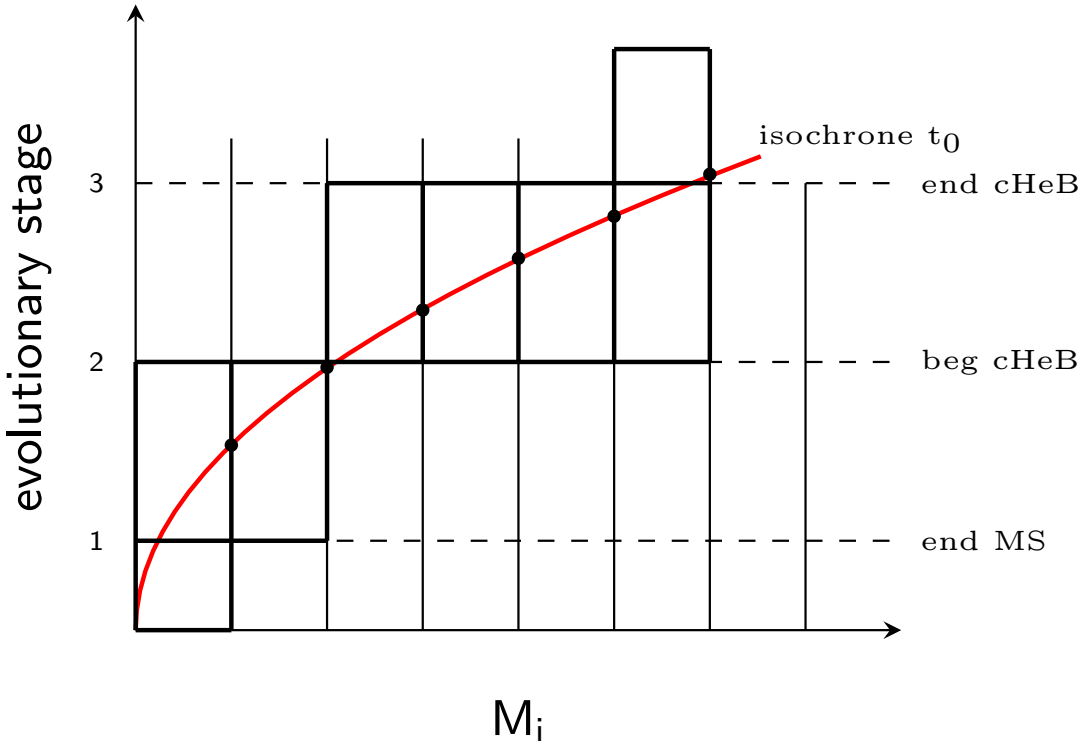

Figure B2: Evolutionary stage versus mass diagram. Each horizontal line in this plot is a line of equivalent evolutionary stages. The red line shows an example of isochrone, which in this diagram runs diagonally. There are the same three evolutionary stages as in Figure B1. The black dots indicate the intersections between the isochrone and the evolutionary tracks.

B.3 Interpolations inside a square

Figure B3 details one of these squares. The corners of the square are the points with ages t_i^j, t_i^{j+1} (both along the track i), and t_{i+1}^j, t_{i+1}^{j+1} (along the track i+1). First, we should know if the isochrone t_0 crosses it: if ($t_i^j < t_0 < t_i^{j+1}$) or ($t_{i+1}^j < t_0 < t_{i+1}^{j+1}$) then continue to work with this square, else jump to the next square.

Let us suppose the isochrone crosses the square from a to b as shown in Figure B3. For every point over the first track i, we should find an equivalent point over the track i+1. This is easy. This point over the first track has an age t, which satisfies $t_i^j < t_i < t_i^{j+1}$. It is located at a fraction $f_1 = (t_i - t_i^j)/(t_i^{j+1} - t_{i+1}^j)$ of the interval $[t_i^j, t_i^{j+1}]$. An equivalent point over the second track is the one located at the same fraction f_1 of the interval $[t_{i+1}^j, ti + 1^{j+1}]$. By using the formula $f_1 = (t_{i+1} - t_{i+1}^j)/(t_{i+1}^{j+1} - t_{i+1}^j)$ where only t_{i+1} is unknown, we can find the age t_{i+1}.

Then, we single out the values of L and T_{eff} for the points of age t_i and t_{i+1}. This is also easy since you have a lot of points in every evolutionary track.

Now, we test if the age t_i and t_{i+1} contain a point of the isochrone: we test if $t_i < t_0 < t_{i+1}$ or $t_i > t_0 > t_{i+1}$. If this is the case, the isochrone age is located at a fraction $f_2 = (\log(t_0) - \log(t_i))/(\log(t_{i+1}) - \log(t_i))$ of the interval $[t_i, t_{i+1}]$. This fraction f_2

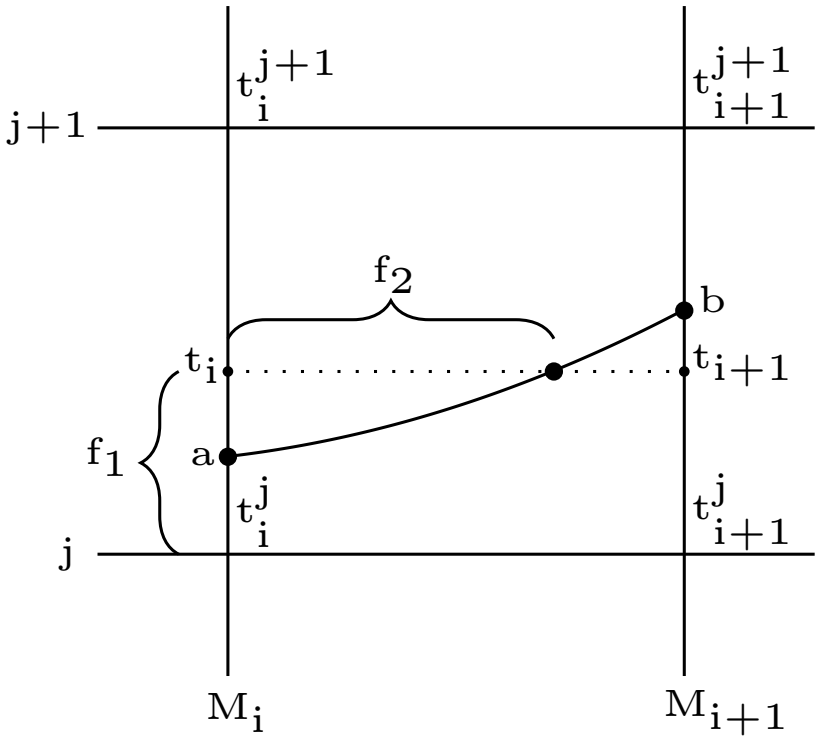

Figure B3: Detail of one of the highlighted squares in Figure B2. This illustrates the interpolation process at the basis of isochrone construction. See text for more details.

is then used to interpolate the quantities L and T_{eff} between the two tracks. For instance $f_2 = (\log L/L_\odot(t_0) - \log L/L_\odot(t_i))/(\log L/L_\odot(t_{i+1}) - \log(t_i))$, where only $\log L/L_\odot(t_0)$ is unknown, or $\log L/L_\odot(t_0) = (1 - f_2) * \log L/L_\odot(t_i) + f_2 * \log L/L_\odot(t_{i+1})$.

Why did I use log(t) instead of t for computing f_2? Because I want to estimate also the mass of the isochrone point, and, for the main evolutionary stages, $\log M$ scales more or less linearly with log(t). This means that by using log we can safely use linear interpolations between the quantities on the different tracks.

The stellar mass of the isochrone point, M_{t_0}, is found using $\log(M_{t_0}) = (1 - f_2) * \log(M_i) + f_2 * \log(M_{i+1})$. Then, we have found M, $\log L/L_\odot$, and $\log T_{eff}$ for a single isochrone point. You repeat the process for as many points as you want over the track. When you finish the interpolations inside a square, you jump to the next square between the tracks [i, i+1]. When you finish the tracks [i, i+1], you jump to the tracks [i+1, i+2].

B.4 Interpolating between tracks with different numbers of equivalent evolutionary stages

Figure B4 illustrates the situation we find passing from stars with radiative to convective burning core: suddenly we have to consider the important evolutionary stages of minimum and maximum T_{eff} which delimit the overall contraction phase.

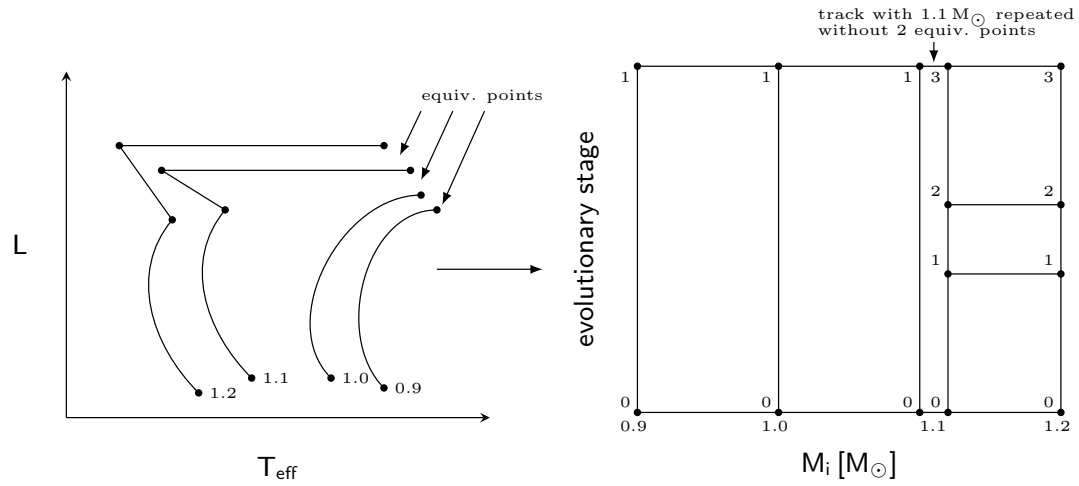

Figure B4: Example of HRD with four different evolutionary tracks, and the transposition in the corresponding evolutionary stage versus mass diagram. These two plots show the transition from tracks with radiative core hydrogen burning to those with a convective one. The black dots show the corresponding equivalent points in the two cases.

This situation is dealt very simply with the "squares algorithm" described above. The right panel of Figure B4 shows the sample of squares for some tracks, limited to those that comprehend the core H-burning. For masses $M < 1.1M_{\odot}$, the complete MS is described by a single square per pair of tracks, whereas for $M > 1.1M_{\odot}$ we need 3 squares per pair. $M = 1.1M_{\odot}$ is the transition mass: passing from left to right, we simply introduce additional squares, taking care that the definition of the equivalent evolutionary stages is consistent (notice e.g. that for $M < 1.1M_{\odot}$ the stage $X_c = 0$ is the second one, whereas for $M > 1.1M_{\odot}$ it becomes the fourth one).

B.5 Practical issues

It is convenient to deal with small tables containing a limited number of points per track (about 200 models well distributed on the HR diagram), in which the important evolutionary stages are marked. Mark the equivalent evolutionary points with a simple (increasing) number so that the code can easily identify which points to use in the square corners. When the number of equivalent points increases (e.g. the case of the $1.1M_{\odot}$ track in Figure B4), the simplest thing to do is to write this track twice. The first time with a smaller number of equivalent points, the second time with more equivalent points. In this way, you have always pairs of tracks with the same number of squares to

interpolate between.

B.6 Practical application

For this application, I selected the stellar models shown in Figure A3, computed by Nguyen et al. (2022). Then, I divided each track within the set into evolutionary phases with the *python* code presented in Appendix A. Next, I adopted the TRILEGAL code to construct the isochrones by interpolating the stellar properties as described in the sections above. The present algorithms have been used in Nguyen et al. (2022) and are now being adapted to the more complicated case of Volpato et al. (2023) tracks.

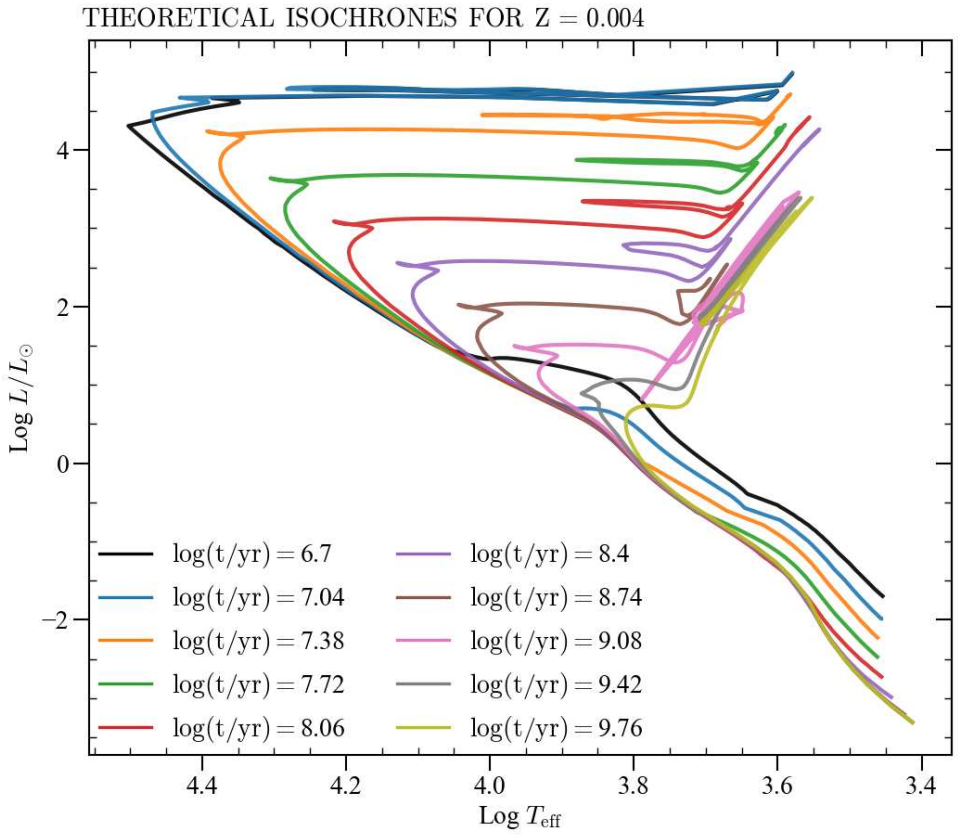

Figure B5: Theoretical isochrones calculated with the TRILEGAL code. The diagram shows isochrones of the models in Figure A3 for ten different ages.

These theoretical isochrones cover a range of masses, from very low mass ($\sim 0.09 M_\odot$) up to massive stars ($\sim 14 M_\odot$). They have an initial metallicity of Z = 0.004 and zero initial rotational velocity. You can find a detailed discussion of rotating and non-rotating theoretical isochrones at different metallicities in Nguyen (2022).

You can obtain the same isochrones using a dedicated web interface[1]. Additionally,

[1] http://stev.oapd.inaf.it/cgi-bin/cmd_3.7

there is a separate web interface[2] for stellar tracks computed with the PARSEC code. Both of these repositories are managed by the PARSEC team, with Dr. Léo Girardi and Dr. Guglielmo Costa being primarily responsible for them.

[2] http://stev.oapd.inaf.it/PARSEC/tracks_v2.html

§Bibliography

B. P. Abbott, R. Abbott, T. D. Abbott, M. R. Abernathy, F. Acernese, et al. "GW150914: First results from the search for binary black hole coalescence with Advanced LIGO". *PhRvD*, 93(12):122003, June 2016. doi:10.1103/PhysRevD.93.122003.

R. Abbott, T. D. Abbott, S. Abraham, F. Acernese, K. Ackley, et al. "GW190521: A Binary Black Hole Merger with a Total Mass of 150 $M_\odot$". *PhRvL*, 125(10):101102, Sept. 2020. doi:10.1103/PhysRevLett.125.101102.

T. Abel, G. L. Bryan, and M. L. Norman. "The Formation of the First Star in the Universe". *Science*, 295(5552):93–98, Jan. 2002. doi:10.1126/science.1063991.

C. Aerts, S. Mathis, and T. M. Rogers. "Angular Momentum Transport in Stellar Interiors". *ARA&A*, 57:35–78, Aug. 2019. doi:10.1146/annurev-astro-091918-104359.

D. R. Aguilera-Dena, N. Langer, T. J. Moriya, and A. Schootemeijer. "Related Progenitor Models for Long-duration Gamma-Ray Bursts and Type Ic Superluminous Supernovae". *ApJ*, 858(2):115, May 2018. doi:10.3847/1538-4357/aabfc1.

M. L. Aizenman, C. J. Hansen, and R. R. Ross. "Pulsation Properties of Upper-Main Stars". *ApJ*, 201:387–391, Oct. 1975. doi:10.1086/153897.

M. Alongi, G. Bertelli, A. Bressan, and C. Chiosi. "Effects of envelope overshoot on stellar models.". *A&A*, 244:95, Apr. 1991.

M. Á. Aloy and M. Obergaulinger. "Magnetorotational core collapse of possible GRB progenitors - II. Formation of protomagnetars and collapsars". *MNRAS*, 500(4):4365–4397, Jan. 2021. doi:10.1093/mnras/staa3273.

R. I. Anderson, H. Saio, S. Ekström, C. Georgy, and G. Meynet. "On the effect of rotation on populations of classical Cepheids. II. Pulsation analysis for metallicities 0.014, 0.006, and 0.002". *A&A*, 591:A8, June 2016. doi:10.1051/0004-6361/201528031.

I. Appenzeller. "The evolution of a vibrationally unstable main-sequence star of 130 M sun.". *A&A*, 5:355, May 1970.

I. Baraffe, A. Heger, and S. E. Woosley. "On the Stability of Very Massive Primordial Stars". *ApJ*, 550(2):890–896, Apr. 2001. doi:10.1086/319808.

J. M. Bardeen, W. H. Press, and S. A. Teukolsky. "Rotating Black Holes: Locally Nonrotating Frames, Energy Extraction, and Scalar Synchrotron Radiation". *ApJ*, 178:347–370, Dec. 1972. doi:10.1086/151796.

Z. Barkat, G. Rakavy, and N. Sack. "Dynamics of Supernova Explosion Resulting from Pair Formation". *PhRvL*, 18(10):379–381, Mar. 1967. doi:10.1103/PhysRevLett.18.379.

H. Belkus, J. Van Bever, and D. Vanbeveren. "The Evolution of Very Massive Stars". *ApJ*, 659(2):1576–1581, Apr. 2007. doi:10.1086/512181.

P. D. Bennett. Chromospheres and Winds of Red Supergiants: An Empirical Look at Outer Atmospheric Structure. In C. Leitherer, P. D. Bennett, P. W. Morris, and J. T. Van Loon, editors, *Hot and Cool: Bridging Gaps in Massive Star Evolution*, volume 425 of *Astronomical Society of the Pacific Conference Series*, page 181, June 2010.

R. D. Blandford and R. L. Znajek. "Electromagnetic extraction of energy from Kerr black holes.". *MNRAS*, 179:433–456, May 1977. doi:10.1093/mnras/179.3.433.

E. Böhm-Vitense. "Über die Wasserstoffkonvektionszone in Sternen verschiedener Effektivtemperaturen und Leuchtkräfte. Mit 5 Textabbildungen". *ZA*, 46:108, Jan. 1958.

J. R. Bond, W. D. Arnett, and B. J. Carr. "The evolution and fate of Very Massive Objects". *ApJ*, 280:825–847, May 1984. doi:10.1086/162057.

J. Braithwaite and H. C. Spruit. "Magnetic fields in non-convective regions of stars". *Royal Society Open Science*, 4(2):160271, Feb. 2017. doi:10.1098/rsos.160271.

A. Bressan, P. Marigo, L. Girardi, B. Salasnich, C. Dal Cero, S. Rubele, and A. Nanni. "PARSEC: stellar tracks and isochrones with the PAdova and TRieste Stellar Evolution Code". *MNRAS*, 427(1):127–145, Nov. 2012. doi:10.1111/j.1365-2966.2012.21948.x.

A. G. Bressan, C. Chiosi, and G. Bertelli. "Mass loss and overshooting in massive stars". *A&A*, 102(1):25–30, Sept. 1981.

V. Bromm, P. S. Coppi, and R. B. Larson. "Forming the First Stars in the Universe: The Fragmentation of Primordial Gas". *ApJL*, 527(1):L5–L8, Dec. 1999. doi:10.1086/312385.

I. Brott, S. E. de Mink, M. Cantiello, N. Langer, A. de Koter, C. J. Evans, I. Hunter, C. Trundle, and J. S. Vink. "Rotating massive main-sequence stars. I. Grids of evolutionary models and isochrones". *A&A*, 530:A115, June 2011. doi:10.1051/0004-6361/201016113.

A. S. Brun and M. K. Browning. "Magnetism, dynamo action and the solar-stellar connection". *Living Reviews in Solar Physics*, 14(1):4, Sept. 2017. doi:10.1007/s41116-017-0007-8.

D. Brunt. "Some problems of astronomy (I The problem of the Cepheid variables)". *The Observatory*, 36:59–62, Jan. 1913.

D. Burlon, T. Murphy, G. Ghirlanda, P. J. Hancock, R. Parry, and R. Salvaterra. "Gamma-ray bursts from massive Population-III stars: clues from the radio band". *MNRAS*, 459(3):3356–3362, July 2016. doi:10.1093/mnras/stw905.

E. Caffau, H. G. Ludwig, M. Steffen, B. Freytag, and P. Bonifacio. "Solar Chemical Abundances Determined with a CO5BOLD 3D Model Atmosphere". *SoPh*, 268(2): 255–269, Feb. 2011. doi:10.1007/s11207-010-9541-4.

M. Catelan and H. A. Smith. *Pulsating Stars*. Weinhem: Wiley-VCH, 2015. doi:10.1002/9783527655182.

K.-J. Chen, S. Woosley, A. Heger, A. Almgren, and D. J. Whalen. "Two-dimensional Simulations of Pulsational Pair-instability Supernovae". *ApJ*, 792(1):28, Sept. 2014. doi:10.1088/0004-637X/792/1/28.

Y. Chen, A. Bressan, L. Girardi, P. Marigo, X. Kong, and A. Lanza. "PARSEC evolutionary tracks of massive stars up to 350 $M_\odot$ at metallicities $0.0001 \leq Z \leq 0.04$". *MNRAS*, 452(1):1068–1080, Sept. 2015. doi:10.1093/mnras/stv1281.

P. C. Clark, S. C. O. Glover, R. S. Klessen, and V. Bromm. "Gravitational Fragmentation in Turbulent Primordial Gas and the Initial Mass Function of Population III Stars". *ApJ*, 727(2):110, Feb. 2011. doi:10.1088/0004-637X/727/2/110.

G. Costa. *Evolution of rotating stars with PARSEC: implementation and comparison with observations*. PhD thesis, SISSA, 2019. URL https://iris.sissa.it/handle/20.500.11767/103863?mode=full.

G. Costa, L. Girardi, A. Bressan, Y. Chen, P. Goudfrooij, P. Marigo, T. S. Rodrigues, and A. Lanza. "Multiple stellar populations in NGC 1866. New clues from Cepheids and colour-magnitude diagram". *A&A*, 631:A128, Nov. 2019a. doi:10.1051/0004-6361/201936409.

G. Costa, L. Girardi, A. Bressan, P. Marigo, T. S. Rodrigues, Y. Chen, A. Lanza, and P. Goudfrooij. "Mixing by overshooting and rotation in intermediate-mass stars". *MNRAS*, 485(4):4641–4657, June 2019b. doi:10.1093/mnras/stz728.

G. Costa, A. Bressan, M. Mapelli, P. Marigo, G. Iorio, and M. Spera. "Formation of GW190521 from stellar evolution: the impact of the hydrogen-rich envelope, dredge-up, and $^{12}C(\alpha, \gamma)^{16}O$ rate on the pair-instability black hole mass gap". *MNRAS*, 501 (3):4514–4533, Mar. 2021. doi:10.1093/mnras/staa3916.

G. Costa, M. Chruślińska, J. Klencki, F. S. Broekgaarden, C. L. Rodriguez, T. D. Joseph, and S. Saracino. "Stellar Black Holes and Compact Stellar Remnants". *arXiv e-prints*, art. arXiv:2311.15778, Nov. 2023a. doi:10.48550/arXiv.2311.15778.

G. Costa, M. Mapelli, G. Iorio, F. Santoliquido, G. J. Escobar, R. S. Klessen, and A. Bressan. "Massive binary black holes from Population II and III stars". *MNRAS*, 525(2):2891–2906, Oct. 2023b. doi:10.1093/mnras/stad2443.

T. G. Cowling. "The stability of gaseous stars (Second paper)". *MNRAS*, 96:42, Nov. 1935. doi:10.1093/mnras/96.1.42.

A. N. Cox and J. H. Cahn. "The Pulsational Stability of Wolf-Rayet Stars". *ApJ*, 326: 804, Mar. 1988. doi:10.1086/166139.

J. P. Cox. "The pulsational stability of models for red giant stars". *Publications of the Goethe Link Observatory*, 16:139–145, Jan. 1955.

J. P. Cox. "Non-Adiabatic Stellar Pulsation. I.". *ApJ*, 127:194, Jan. 1958. doi:10.1086/146451.

J. P. Cox and C. Whitney. "Stellar Pulsation.IV. a Semitheoretical Period-Luminosity Relation for Classical Cepheids.". *ApJ*, 127:561, May 1958. doi:10.1086/146489.

D. Croon, S. D. McDermott, and J. Sakstein. "New physics and the black hole mass gap". *Phys. Rev. D*, 102:115024, Dec 2020. doi:10.1103/PhysRevD.102.115024. URL https://link.aps.org/doi/10.1103/PhysRevD.102.115024.

P. A. Crowther. "Massive Stars in the Tarantula Nebula: A Rosetta Stone for Extragalactic Supergiant HII Regions". *Galaxies*, 7(4):88, Nov. 2019. doi:10.3390/galaxies7040088.

R. H. Cyburt, A. M. Amthor, R. Ferguson, Z. Meisel, K. Smith, et al. "The JINA REACLIB Database: Its Recent Updates and Impact on Type-I X-ray Bursts". *ApJS*, 189(1):240–252, July 2010a. doi:10.1088/0067-0049/189/1/240.

R. H. Cyburt, A. M. Amthor, R. Ferguson, Z. Meisel, K. Smith, et al. "The JINA REACLIB Database: Its Recent Updates and Impact on Type-I X-ray Bursts". *ApJS*, 189(1):240–252, July 2010b. doi:10.1088/0067-0049/189/1/240.

C. de Jager, H. Nieuwenhuijzen, and K. A. van der Hucht. "Mass loss rates in the Hertzsprung-Russell diagram.". *A&AS*, 72:259–289, Feb. 1988.

M. Dijkstra and J. S. B. Wyithe. "Very massive stars in high-redshift galaxies". *MNRAS*, 379(4):1589–1598, Aug. 2007. doi:10.1111/j.1365-2966.2007.12039.x.

A. S. Eddington. "The problem of the Cepheid variables". *MNRAS*, 79:2, Nov. 1918.

A. S. Eddington. "On the pulsations of a gaseous star". *MNRAS*, 79:177–189, Jan. 1919.

A. S. Eddington. *The Internal Constitution of the Stars*. "Cambridge University Pres", 1926.

A. S. Eddington. "Internal circulation in rotating stars". *MNRAS*, 90:54, Nov. 1929. doi:10.1093/mnras/90.1.54.

S. Eddington, A. S. "On the cause of Cepheid pulsation". *MNRAS*, 101:182, Jan. 1941. doi:10.1093/mnras/101.4.182.

S. Ekström, G. Meynet, C. Chiappini, R. Hirschi, and A. Maeder. "Effects of rotation on the evolution of primordial stars". *A&A*, 489(2):685–698, Oct. 2008. doi:10.1051/0004-6361:200809633.

S. Ekström, C. Georgy, P. Eggenberger, G. Meynet, N. Mowlavi, et al. "Grids of stellar models with rotation. I. Models from 0.8 to 120 $M_\odot$ at solar metallicity (Z = 0.014)". *A&A*, 537:A146, Jan. 2012. doi:10.1051/0004-6361/201117751.

R. Emden. *Gaskugeln.* 1907.

A. S. Endal and S. Sofia. "The evolution of rotating stars. I. Method and exploratory calculations for a 7 M sun star.". *ApJ*, 210:184–198, Nov. 1976. doi:10.1086/154817.

I. Epstein. "Pulsation Properties of Giant-Star Models.". *ApJ*, 112:6, July 1950. doi:10.1086/145316.

E. Farag, M. Renzo, R. Farmer, M. T. Chidester, and F. X. Timmes. "Resolving the peak of the black hole mass spectrum". *The Astrophysical Journal*, 937(2):112, oct 2022. doi:10.3847/1538-4357/ac8b83. URL https://dx.doi.org/10.3847/1538-4357/ac8b83.

R. Farmer, M. Renzo, S. E. de Mink, P. Marchant, and S. Justham. "Mind the Gap: The Location of the Lower Edge of the Pair-instability Supernova Black Hole Mass Gap". *ApJ*, 887(1):53, Dec. 2019. doi:10.3847/1538-4357/ab518b.

R. Farmer, M. Renzo, S. E. de Mink, M. Fishbach, and S. Justham. "Constraints from Gravitational-wave Detections of Binary Black Hole Mergers on the $^{12}C(\alpha, \gamma)^{16}O$ Rate". *ApJL*, 902(2):L36, Oct. 2020. doi:10.3847/2041-8213/abbadd.

E. Farrell, J. H. Groh, R. Hirschi, L. Murphy, E. Kaiser, S. Ekström, C. Georgy, and G. Meynet. "Is GW190521 the merger of black holes from the first stellar generations?". *MNRAS*, 502(1):L40–L44, Mar. 2021. doi:10.1093/mnrasl/slaa196.

W. A. Fowler and F. Hoyle. "Neutrino Processes and Pair Formation in Massive Stars and Supernovae.". *ApJS*, 9:201, Dec. 1964. doi:10.1086/190103.

G. Fragione, A. Loeb, B. Kocsis, and F. A. Rasio. "Merger Rates of Intermediate-mass Black Hole Binaries in Nuclear Star Clusters". *ApJ*, 933(2):170, July 2022. doi:10.3847/1538-4357/ac75d0.

G. S. Fraley. "Supernovae Explosions Induced by Pair-Production Instability". *Ap&SS*, 2(1):96–114, Aug. 1968. doi:10.1007/BF00651498.

C. L. Fryer and V. Kalogera. "Theoretical Black Hole Mass Distributions". *ApJ*, 554(1): 548–560, June 2001. doi:10.1086/321359.

C. L. Fryer, K. Belczynski, G. Wiktorowicz, M. Dominik, V. Kalogera, and D. E. Holz. "Compact Remnant Mass Function: Dependence on the Explosion Mechanism and Metallicity". *ApJ*, 749(1):91, Apr. 2012. doi:10.1088/0004-637X/749/1/91.

X. Fu, A. Bressan, P. Marigo, L. Girardi, J. Montalbán, Y. Chen, and A. Nanni. "New PARSEC data base of α-enhanced stellar evolutionary tracks and isochrones - I. Calibration with 47 Tuc (NGC 104) and the improvement on RGB bump". *MNRAS*, 476 (1):496–511, May 2018. doi:10.1093/mnras/sty235.

C. Georgy, G. Meynet, and A. Maeder. "Effects of anisotropic winds on massive star evolution". *A&A*, 527:A52, Mar. 2011. doi:10.1051/0004-6361/200913797.

C. Georgy, S. Ekström, P. Eggenberger, G. Meynet, L. Haemmerlé, et al. "Grids of stellar models with rotation. III. Models from 0.8 to 120 $M_\odot$ at a metallicity Z = 0.002". *A&A*, 558:A103, Oct. 2013. doi:10.1051/0004-6361/201322178.

L. Girardi, M. A. T. Groenewegen, E. Hatziminaoglou, and L. da Costa. "Star counts in the Galaxy. Simulating from very deep to very shallow photometric surveys with the TRILEGAL code". *A&A*, 436(3):895–915, June 2005. doi:10.1051/0004-6361:20042352.

W. Glatzel and M. Kiriakidis. "The stability of massive main-sequence stars". *MNRAS*, 262(1):85–92, May 1993. doi:10.1093/mnras/262.1.85.

W. Glatzel, K. J. Fricke, and M. F. El Eid. "The fate of rotating pair-unstable carbon-oxygen cores". *A&A*, 149(2):413–422, Aug. 1985.

S. Goswami, A. Slemer, P. Marigo, A. Bressan, L. Silva, M. Spera, L. Boco, V. Grisoni, L. Pantoni, and A. Lapi. "The effects of the initial mass function on Galactic chemical enrichment". *A&A*, 650:A203, June 2021. doi:10.1051/0004-6361/202039842.

S. Goswami, L. Silva, A. Bressan, V. Grisoni, G. Costa, P. Marigo, G. L. Granato, A. Lapi, and M. Spera. "Impact of very massive stars on the chemical evolution of extremely metal-poor galaxies". *A&A*, 663:A1, July 2022. doi:10.1051/0004-6361/202142031.

G. Gräfener and W. R. Hamann. "Mass loss from late-type WN stars and its Z-dependence. Very massive stars approaching the Eddington limit". *A&A*, 482(3):945–960, May 2008. doi:10.1051/0004-6361:20066176.

J. H. Groh, S. Ekström, C. Georgy, G. Meynet, A. Choplin, et al. "Grids of stellar models with rotation. IV. Models from 1.7 to 120 $M_\odot$ at a metallicity Z = 0.0004". *A&A*, 627: A24, July 2019. doi:10.1051/0004-6361/201833720.

M. Haft, G. Raffelt, and A. Weiss. "Standard and Nonstandard Plasma Neutrino Emission Revisited". *ApJ*, 425:222, Apr. 1994. doi:10.1086/173978.

A. Heger and S. E. Woosley. "The Nucleosynthetic Signature of Population III". *ApJ*, 567(1):532–543, Mar. 2002. doi:10.1086/338487.

A. Heger, L. Jeannin, N. Langer, and I. Baraffe. "Pulsations in red supergiants with high L/M ratio. Implications for the stellar and circumstellar structure of supernova progenitors". *A&A*, 327:224–230, Nov. 1997. doi:10.48550/arXiv.astro-ph/9705097.

A. Heger, N. Langer, and S. E. Woosley. "Presupernova Evolution of Rotating Massive Stars. I. Numerical Method and Evolution of the Internal Stellar Structure". *ApJ*, 528 (1):368–396, Jan. 2000. doi:10.1086/308158.

A. Heger, C. L. Fryer, S. E. Woosley, N. Langer, and D. H. Hartmann. "How Massive Single Stars End Their Life". *ApJ*, 591(1):288–300, July 2003. doi:10.1086/375341.

E. R. Higgins, J. S. Vink, G. N. Sabhahit, and A. A. C. Sander. "The hydrogen clock to infer the upper stellar mass". *MNRAS*, Sept. 2022. doi:10.1093/mnras/stac2485.

S. Hirano, T. Hosokawa, N. Yoshida, H. Umeda, K. Omukai, G. Chiaki, and H. W. Yorke. "One Hundred First Stars: Protostellar Evolution and the Final Masses". *ApJ*, 781(2): 60, Feb. 2014. doi:10.1088/0004-637X/781/2/60.

S. Höfner and H. Olofsson. "Mass loss of stars on the asymptotic giant branch. Mechanisms, models and measurements". *A&A Rv*, 26(1):1, Jan. 2018. doi:10.1007/s00159-017-0106-5.

T. Hosokawa, K. Omukai, N. Yoshida, and H. W. Yorke. "Protostellar Feedback Halts the Growth of the First Stars in the Universe". *Science*, 334(6060):1250, Dec. 2011. doi:10.1126/science.1207433.

C. A. Iglesias and F. J. Rogers. "Updated Opal Opacities". *ApJ*, 464:943, June 1996. doi:10.1086/177381.

K. Inayoshi, T. Hosokawa, and K. Omukai. "Pulsational instability of supergiant protostars: do they grow supermassive by accretion?". *MNRAS*, 431(4):3036–3044, June 2013. doi:10.1093/mnras/stt362.

A. W. Irwin. FreeEOS: Equation of State for stellar interiors calculations. Astrophysics Source Code Library, record ascl:1211.002, Nov. 2012.

N. Itoh and Y. Kohyama. "Neutrino-pair bremsstrahlung in dense stars. I. Liquid metal case.". *ApJ*, 275:858–866, Dec. 1983. doi:10.1086/161579.

N. Itoh, S. Uchida, Y. Sakamoto, Y. Kohyama, and S. Nozawa. "The Second Born Corrections to the Electrical and Thermal Conductivities of Dense Matter in the Liquid Metal Phase". *ApJ*, 677(1):495–502, Apr. 2008. doi:10.1086/529367.

N. D. Kee, J. O. Sundqvist, L. Decin, A. de Koter, and H. Sana. "Analytic, dust-independent mass-loss rates for red supergiant winds initiated by turbulent pressure". *A&A*, 646:A180, Feb. 2021. doi:10.1051/0004-6361/202039224.

Z. Keszthelyi. "Magnetism in High-Mass Stars". *Galaxies*, 11(2):40, Mar. 2023. doi:10.3390/galaxies11020040.

R. Kippenhahn and H. C. Thomas. *A Simple Method for the Solution of the Stellar Structure Equations Including Rotation and Tidal Forces*. IAU Colloq. 4: Stellar Rotation, 1970.

M. Kiriakidis, K. J. Fricke, and W. Glatzel. "The stability of massive stars and its dependence on metallicity and opacity.". *MNRAS*, 264:50–62, Sept. 1993. doi:10.1093/mnras/264.1.50.

E. Komatsu, K. M. Smith, J. Dunkley, C. L. Bennett, B. Gold, et al. "Seven-year Wilkinson Microwave Anisotropy Probe (WMAP) Observations: Cosmological Interpretation". *ApJS*, 192(2):18, Feb. 2011. doi:10.1088/0067-0049/192/2/18.

S. S. Komissarov and M. V. Barkov. "Supercollapsars and their X-ray bursts". *MNRAS*, 402(1):L25–L29, Feb. 2010. doi:10.1111/j.1745-3933.2009.00792.x.

A. Kozyreva, S. C. Yoon, and N. Langer. "Explosion and nucleosynthesis of low-redshift pair-instability supernovae". *A&A*, 566:A146, June 2014. doi:10.1051/0004-6361/201423641.

A. Kozyreva, M. Gilmer, R. Hirschi, C. Fröhlich, S. Blinnikov, et al. "Fast evolving pair-instability supernova models: evolution, explosion, light curves". *MNRAS*, 464 (3):2854–2865, Jan. 2017. doi:10.1093/mnras/stw2562.

N. Langer, C. A. Norman, A. de Koter, J. S. Vink, M. Cantiello, and S. C. Yoon. "Pair creation supernovae at low and high redshift". *A&A*, 475(2):L19–L23, Nov. 2007. doi:10.1051/0004-6361:20078482.

R. B. Larson. "Early star formation and the evolution of the stellar initial mass function in galaxies". *MNRAS*, 301(2):569–581, Dec. 1998. doi:10.1046/j.1365-8711.1998.02045.x.

H. S. Leavitt and E. C. Pickering. "Periods of 25 Variable Stars in the Small Magellanic Cloud.". *Harvard College Observatory Circular*, 173:1–3, Mar. 1912.

P. Ledoux. "On the Vibrational Stability of Gaseous Stars.". *ApJ*, 94:537, Nov. 1941. doi:10.1086/144359.

S.-C. Leung, K. Nomoto, and S. Blinnikov. "Pulsational Pair-instability Supernovae. I. Pre-collapse Evolution and Pulsational Mass Ejection". *ApJ*, 887(1):72, Dec. 2019. doi:10.3847/1538-4357/ab4fe5.

M. Limongi and A. Chieffi. "Presupernova Evolution and Explosive Nucleosynthesis of Rotating Massive Stars in the Metallicity Range -3 $\leq$ [Fe/H] $\leq$ 0". *ApJS*, 237(1):13, July 2018. doi:10.3847/1538-4365/aacb24.

D. Macpherson and D. Coward. "Multiwavelength detectability of Pop III GRBs from afterglow simulations". *MNRAS*, 467(2):2476–2493, May 2017. doi:10.1093/mnras/stx198.

A. Maeder. "Stellar evolution III: the overshooting from convective cores.". *A&A*, 40(3): 303–310, May 1975.

A. Maeder. "Vibrational instability of Wolf-Rayet stars". *A&A*, 147(2):300–308, June 1985.

A. Maeder. *Physics, Formation and Evolution of Rotating Stars*. Springer Berlin, Heidelberg, 2009. doi:10.1007/978-3-540-76949-1.

A. Maeder and G. Meynet. "Stellar evolution with rotation. VI. The Eddington and Omega -limits, the rotational mass loss for OB and LBV stars". *A&A*, 361:159–166, Sept. 2000. doi:10.48550/arXiv.astro-ph/0006405.

A. Maeder and G. Meynet. "Stellar evolution with rotation and magnetic fields. III. The interplay of circulation and dynamo". *A&A*, 440(3):1041–1049, Sept. 2005. doi:10.1051/0004-6361:20053261.

M. Mapelli, M. Spera, E. Montanari, M. Limongi, A. Chieffi, N. Giacobbo, A. Bressan, and Y. Bouffanais. "Impact of the Rotation and Compactness of Progenitors on the Mass of Black Holes". *ApJ*, 888(2):76, Jan. 2020. doi:10.3847/1538-4357/ab584d.

P. Marchant and T. J. Moriya. "The impact of stellar rotation on the black hole mass-gap from pair-instability supernovae". *A&A*, 640:L18, Aug. 2020. doi:10.1051/0004-6361/202038902.

P. Marchant, M. Renzo, R. Farmer, K. M. W. Pappas, R. E. Taam, S. E. de Mink, and V. Kalogera. "Pulsational Pair-instability Supernovae in Very Close Binaries". *ApJ*, 882(1):36, Sept. 2019. doi:10.3847/1538-4357/ab3426.

P. Marigo and B. Aringer. "Low-temperature gas opacity. ÆSOPUS: a versatile and quick computational tool". *A&A*, 508(3):1539–1569, Dec. 2009. doi:10.1051/0004-6361/200912598.

P. Marigo, L. Girardi, C. Chiosi, and P. R. Wood. "Zero-metallicity stars. I. Evolution at constant mass". *A&A*, 371:152–173, May 2001. doi:10.1051/0004-6361:20010309.

P. Marigo, C. Chiosi, and R. P. Kudritzki. "Zero-metallicity stars. II. Evolution of very massive objects with mass loss". *A&A*, 399:617–630, Feb. 2003. doi:10.1051/0004-6361:20021756.

P. Marigo, L. Girardi, A. Bressan, P. Rosenfield, B. Aringer, et al. "A New Generation of PARSEC-COLIBRI Stellar Isochrones Including the TP-AGB Phase". *ApJ*, 835(1): 77, Jan. 2017. doi:10.3847/1538-4357/835/1/77.

P. Marigo, B. Aringer, L. Girardi, and A. Bressan. "Updated Low-temperature Gas Opacities with ÆSOPUS 2.0". *ApJ*, 940(2):129, Dec. 2022. doi:10.3847/1538-4357/ac9b40.

S. Martinet, G. Meynet, S. Ekström, C. Georgy, and R. Hirschi. "Very Massive Star Models: I. Impact of Rotation and Metallicity and Comparisons with Observations". *arXiv e-prints*, art. arXiv:2309.00062, Aug. 2023. doi:10.48550/arXiv.2309.00062.

G. Meynet and A. Maeder. "Stellar evolution with rotation. I. The computational method and the inhibiting effect of the μ-gradient.". *A&A*, 321:465–476, May 1997.

G. Meynet and A. Maeder. "Stellar evolution with rotation. V. Changes in all the outputs of massive star models". *A&A*, 361:101–120, Sept. 2000. doi:10.48550/arXiv.astro-ph/0006404.

G. Meynet and A. Maeder. "Stellar evolution with rotation. VIII. Models at Z = 10^{-5} and CNO yields for early galactic evolution". *A&A*, 390:561–583, Aug. 2002. doi:10.1051/0004-6361:20020755.

G. Meynet and A. Maeder. "Wind anisotropies and GRB progenitors". *A&A*, 464(2): L11–L15, Mar. 2007. doi:10.1051/0004-6361:20066509.

M. Moe and R. Di Stefano. "Mind Your Ps and Qs: The Interrelation between Period (P) and Mass-ratio (Q) Distributions of Binary Stars". *ApJS*, 230(2):15, June 2017. doi:10.3847/1538-4365/aa6fb6.

T. J. Moriya and N. Langer. "Pulsations of red supergiant pair-instability supernova progenitors leading to extreme mass loss". *A&A*, 573:A18, Jan. 2015. doi:10.1051/0004-6361/201424957.

H. Munakata, Y. Kohyama, and N. Itoh. "Neutrino Energy Loss in Stellar Interiors". *ApJ*, 296:197, Sept. 1985. doi:10.1086/163436.

L. J. Murphy, J. H. Groh, S. Ekström, G. Meynet, C. Pezzotti, et al. "Grids of stellar models with rotation - V. Models from 1.7 to 120 $M_{\odot}$ at zero metallicity". *MNRAS*, 501(2):2745–2763, Feb. 2021. doi:10.1093/mnras/staa3803.

D. K. Nadyozhin and T. L. Razinkova. "Similarity Theory of Stellar Models and the Structure of Very Massive Stars". *Astronomy Letters*, 31(10):695–705, Oct. 2005. doi:10.1134/1.2075312.

H. Nagakura, Y. Suwa, and K. Ioka. "Population III Gamma-Ray Bursts and Breakout Criteria for Accretion-powered Jets". *ApJ*, 754(2):85, Aug. 2012. doi:10.1088/0004-637X/754/2/85.

F. Nakamura and M. Umemura. "On the Initial Mass Function of Population III Stars". *ApJ*, 548(1):19–32, Feb. 2001. doi:10.1086/318663.

D. Nakauchi, K. Inayoshi, and K. Omukai. "Pulsation-driven Mass Loss from Massive Stars behind Stellar Mergers in Metal-poor Dense Clusters". *ApJ*, 902(1):81, Oct. 2020. doi:10.3847/1538-4357/abb463.

C. T. Nguyen. *Stellar Evolution with Rotation in PARSEC v2.0: Tracks and Isochrones for Low- and Intermediate-mass Stars*. PhD thesis, SISSA, 2022.

C. T. Nguyen, G. Costa, L. Girardi, G. Volpato, A. Bressan, Y. Chen, P. Marigo, X. Fu, and P. Goudfrooij. "PARSEC V2.0: Stellar tracks and isochrones of low- and intermediate-mass stars with rotation". *A&A*, 665:A126, Sept. 2022. doi:10.1051/0004-6361/202244166.

K. Nomoto, C. Kobayashi, and N. Tominaga. "Nucleosynthesis in Stars and the Chemical Enrichment of Galaxies". *ARA&A*, 51(1):457–509, Aug. 2013. doi:10.1146/annurev-astro-082812-140956.

W. W. Ober, M. F. El Eid, and K. J. Fricke. "Evolution of Massive Pregalactic Stars - Part Two - Nucleosynthesis in Pair Creation Supernovae and Pregalactic Enrichment". *A&A*, 119:61, Mar. 1983.

M. Obergaulinger and M. Á. Aloy. "Magnetorotational core collapse of possible gamma-ray burst progenitors - IV. A wider range of progenitors". *MNRAS*, 512(2):2489–2507, May 2022. doi:10.1093/mnras/stac613.

T. Ohkubo, K. Nomoto, H. Umeda, N. Yoshida, and S. Tsuruta. "Evolution of Very Massive Population III Stars with Mass Accretion from Pre-main Sequence to Collapse". *ApJ*, 706(2):1184–1193, Dec. 2009. doi:10.1088/0004-637X/706/2/1184.

M. Onoue, N. Kashikawa, Y. Matsuoka, N. Kato, T. Izumi, et al. "Subaru High-z Exploration of Low-luminosity Quasars (SHELLQs). VI. Black Hole Mass Measurements of Six Quasars at $6.1 \leq z \leq 6.7$". *ApJ*, 880(2):77, Aug. 2019. doi:10.3847/1538-4357/ab29e9.

J. C. B. Papaloizou. "Non-linear pulsations of upper main sequence stars-II.Direct numerical integrations". *MNRAS*, 162:169, Jan. 1973a. doi:10.1093/mnras/162.2.169.

J. C. B. Papaloizou. "Non-linear pulsations of upper main sequence stars-II.Direct numerical integrations". *MNRAS*, 162:169, Jan. 1973b. doi:10.1093/mnras/162.2.169.

B. Paxton, M. Cantiello, P. Arras, L. Bildsten, E. F. Brown, et al. "Modules for Experiments in Stellar Astrophysics (MESA): Planets, Oscillations, Rotation, and Massive Stars". *ApJS*, 208(1):4, Sept. 2013. doi:10.1088/0067-0049/208/1/4.

H. G. Plummer. "Note on the velocity of light and Doppler's principle". *MNRAS*, 74: 660, June 1914. doi:10.1093/mnras/74.8.660.

J. Puls, J. S. Vink, and F. Najarro. "Mass loss from hot massive stars". *A&A Rv*, 16 (3-4):209–325, Dec. 2008. doi:10.1007/s00159-008-0015-8.

N. Rahman, H. T. Janka, G. Stockinger, and S. E. Woosley. "Pulsational pair-instability supernovae: gravitational collapse, black hole formation, and beyond". *MNRAS*, 512 (3):4503–4540, May 2022. doi:10.1093/mnras/stac758.

G. Rakavy and G. Shaviv. "Instabilities in Highly Evolved Stellar Models". *ApJ*, 148: 803, June 1967. doi:10.1086/149204.

M. Renzo, C. D. Ott, S. N. Shore, and S. E. de Mink. "Systematic survey of the effects of wind mass loss algorithms on the evolution of single massive stars". *A&A*, 603:A118, July 2017. doi:10.1051/0004-6361/201730698.

A. Ritter. *Wiedemanns Ann.* 1879.

S. Rosseland. "On the luminosity-velocity relation of Cepheids". *MNRAS*, 110:440, Jan. 1950. doi:10.1093/mnras/110.5.440.

P. Saini, S. A. Bhat, and K. G. Arun. "Premerger localization of intermediate mass binary black holes with lisa and prospects of joint observations with athena and lsst". *Phys. Rev. D*, 106:104015, Nov 2022. doi:10.1103/PhysRevD.106.104015. URL `https://link.aps.org/doi/10.1103/PhysRevD.106.104015`.

H. Saio. "Rotational and tidal perturbations of nonradial oscillations in polytropic star.". *ApJ*, 244:299–315, Feb. 1981. doi:10.1086/158708.

J. Sakstein, D. Croon, S. D. McDermott, M. C. Straight, and E. J. Baxter. "Beyond the Standard Model Explanations of GW190521". *PhRvL*, 125(26):261105, Dec. 2020. doi:10.1103/PhysRevLett.125.261105.

Y. Sakurai, N. Yoshida, M. S. Fujii, and S. Hirano. "Formation of intermediate-mass black holes through runaway collisions in the first star clusters". *MNRAS*, 472(2): 1677–1684, Dec. 2017. doi:10.1093/mnras/stx2044.

R. Salvaterra. “High redshift Gamma-Ray Bursts”. *Journal of High Energy Astrophysics*, 7:35–43, Sept. 2015. doi:10.1016/j.jheap.2015.03.001.

H. Sana, S. E. de Mink, A. de Koter, N. Langer, C. J. Evans, M. Gieles, E. Gosset, R. G. Izzard, J. B. Le Bouquin, and F. R. N. Schneider. “Binary Interaction Dominates the Evolution of Massive Stars”. *Science*, 337(6093):444, July 2012. doi:10.1126/science.1223344.

A. A. C. Sander, W. R. Hamann, H. Todt, R. Hainich, T. Shenar, V. Ramachandran, and L. M. Oskinova. “The Galactic WC and WO stars. The impact of revised distances from Gaia DR2 and their role as massive black hole progenitors”. *A&A*, 621:A92, Jan. 2019. doi:10.1051/0004-6361/201833712.

F. R. N. Schneider, H. Sana, C. J. Evans, J. M. Bestenlehner, N. Castro, et al. “An excess of massive stars in the local 30 Doradus starburst”. *Science*, 359(6371):69–71, Jan. 2018. doi:10.1126/science.aan0106.

M. Schwarzschild. *Structure and evolution of the stars*. 1958.

M. Schwarzschild and R. Härm. “On the Maximum Mass of Stable Stars.”. *ApJ*, 129: 637, May 1959. doi:10.1086/146662.

H. Shapley. “On the Nature and Cause of Cepheid Variation”. *ApJ*, 40:448, Dec. 1914. doi:10.1086/142137.

M. M. Shara, S. M. Crawford, D. Vanbeveren, A. F. J. Moffat, D. Zurek, and L. Crause. “The spin rates of O stars in WR + O binaries - I. Motivation, methodology, and first results from SALT”. *MNRAS*, 464(2):2066–2074, Jan. 2017. doi:10.1093/mnras/stw2450.

J. H. Shiode, E. Quataert, and P. Arras. “The stability of massive main-sequence stars as a function of metallicity”. *MNRAS*, 423(4):3397–3404, July 2012. doi:10.1111/j.1365-2966.2012.21130.x.

N. Smith and W. D. Arnett. “Preparing for an Explosion: Hydrodynamic Instabilities and Turbulence in Presupernovae”. *ApJ*, 785(2):82, Apr. 2014. doi:10.1088/0004-637X/785/2/82.

N. Smith and R. Tombleson. “Luminous blue variables are antisocial: their isolation implies that they are kicked mass gainers in binary evolution”. *MNRAS*, 447(1):598–617, Feb. 2015. doi:10.1093/mnras/stu2430.

T. Sonoi and H. Umeda. “Vibrational instability of Population III very massive main-sequence stars due to the ?-mechanism”. *MNRAS*, 421(1):L34–L38, Mar. 2012. doi:10.1111/j.1745-3933.2011.01201.x.

M. Spera and M. Mapelli. “Very massive stars, pair-instability supernovae and intermediate-mass black holes with the sevn code”. *MNRAS*, 470(4):4739–4749, Oct. 2017. doi:10.1093/mnras/stx1576.

M. Spera, M. Mapelli, N. Giacobbo, A. A. Trani, A. Bressan, and G. Costa. “Merging black hole binaries with the SEVN code”. *MNRAS*, 485(1):889–907, May 2019. doi:10.1093/mnras/stz359.

A. Stacy, V. Bromm, and A. T. Lee. "Building up the Population III initial mass function from cosmological initial conditions". *MNRAS*, 462(2):1307–1328, Oct. 2016. doi:10.1093/mnras/stw1728.

R. Stothers and N. R. Simon. "On the Pulsational Stability of Blue Supergiants". *ApJ*, 152:233, Apr. 1968. doi:10.1086/149541.

R. B. Stothers. "Upper Limit to the Mass of Pulsationally Stable Stars with Uniform Chemical Composition". *ApJ*, 392:706, June 1992. doi:10.1086/171472.

R. B. Stothers. "Criterion for the dynamical stability of a non-adiabatic spherical self-gravitating body". *MNRAS*, 305(2):365–372, Apr. 1999. doi:10.1046/j.1365-8711.1999.02444.x.

Y. Suwa and K. Ioka. "Can Gamma-ray Burst Jets Break Out the First Stars?". *ApJ*, 726(2):107, Jan. 2011. doi:10.1088/0004-637X/726/2/107.

K. Takahashi. "The Low Detection Rate of Pair-instability Supernovae and the Effect of the Core Carbon Fraction". *ApJ*, 863(2):153, Aug. 2018. doi:10.3847/1538-4357/aad2d2.

K. Takahashi, T. Yoshida, and H. Umeda. "Stellar Yields of Rotating First Stars. II. Pair-instability Supernovae and Comparison with Observations". *ApJ*, 857(2):111, Apr. 2018. doi:10.3847/1538-4357/aab95f.

J. Talbot, Raymond J. "Nonlinear Pulsations of Unstable Massive Main-Sequence Stars. I. - Amplitude Tests of an Approximation Technique". *ApJ*, 163:17, Jan. 1971a. doi:10.1086/150743.

J. Talbot, Raymond J. "Nonlinear Pulsations of Unstable Massive Main-Sequence Stars. II. Finite-Amplitude Stability". *ApJ*, 165:121, Apr. 1971b. doi:10.1086/150881.

S. Talon and J. P. Zahn. "Anisotropic diffusion and shear instabilities.". *A&A*, 317: 749–751, Feb. 1997. doi:10.48550/arXiv.astro-ph/9609010.

J. Tang, A. Bressan, P. Rosenfield, A. Slemer, P. Marigo, L. Girardi, and L. Bianchi. "New PARSEC evolutionary tracks of massive stars at low metallicity: testing canonical stellar evolution in nearby star-forming dwarf galaxies". *MNRAS*, 445(4):4287–4305, Dec. 2014. doi:10.1093/mnras/stu2029.

A. Tanikawa, T. Kinugawa, T. Yoshida, K. Hijikawa, and H. Umeda. "Population III binary black holes: effects of convective overshooting on formation of GW190521". *MNRAS*, 505(2):2170–2176, Aug. 2021. doi:10.1093/mnras/stab1421.

F. X. Timmes and D. Arnett. "The Accuracy, Consistency, and Speed of Five Equations of State for Stellar Hydrodynamics". *ApJS*, 125(1):277–294, Nov. 1999. doi:10.1086/313271.

K. Toma, T. Sakamoto, and P. Mészáros. "Population III Gamma-ray Burst Afterglows: Constraints on Stellar Masses and External Medium Densities". *ApJ*, 731(2):127, Apr. 2011. doi:10.1088/0004-637X/731/2/127.

J. S. Vink. The True origin of Wolf-Rayet stars. In W.-R. Hamann, A. Sander, and H. Todt, editors, *Wolf-Rayet Stars*, pages 133–138, Jan. 2015.

J. S. Vink, A. de Koter, and H. J. G. L. M. Lamers. "New theoretical mass-loss rates of O and B stars". *A&A*, 362:295–309, Oct. 2000.

J. S. Vink, A. de Koter, and H. J. G. L. M. Lamers. "Mass-loss predictions for O and B stars as a function of metallicity". *A&A*, 369:574–588, Apr. 2001. doi:10.1051/0004-6361:20010127.

J. S. Vink, L. E. Muijres, B. Anthonisse, A. de Koter, G. Gräfener, and N. Langer. "Wind modelling of very massive stars up to 300 solar masses". *A&A*, 531:A132, July 2011. doi:10.1051/0004-6361/201116614.

J. S. Vink, E. R. Higgins, A. A. C. Sander, and G. N. Sabhahit. "Maximum black hole mass across cosmic time". *MNRAS*, 504(1):146–154, June 2021. doi:10.1093/mnras/stab842.

G. Volpato, P. Marigo, G. Costa, A. Bressan, M. Trabucchi, and L. Girardi. "A Study of Primordial Very Massive Star Evolution". *ApJ*, 944(1):40, Feb. 2023. doi:10.3847/1538-4357/acac91.

H. von Zeipel. "The radiative equilibrium of a slightly oblate rotating star". *MNRAS*, 84:684–701, June 1924a. doi:10.1093/mnras/84.9.684.

H. von Zeipel. "The radiative equilibrium of a rotating system of gaseous masses". *MNRAS*, 84:665–683, June 1924b. doi:10.1093/mnras/84.9.665.

R. Walder, D. Folini, and G. Meynet. "Magnetic Fields in Massive Stars, Their Winds, and Their Nebulae". *SSRv*, 166(1-4):145–185, May 2012. doi:10.1007/s11214-011-9771-2.

Y.-F. Wei and T. Liu. "Black Hole Hyperaccretion in Collapsars: A Review". *Universe*, 8(10):529, Oct. 2022. doi:10.3390/universe8100529.

S. Wellstein and N. Langer. "Implications of massive close binaries for black hole formation and supernovae". *A&A*, 350:148–162, Oct. 1999.

S. E. Woosley. "Gamma-Ray Bursts from Stellar Mass Accretion Disks around Black Holes". *ApJ*, 405:273, Mar. 1993. doi:10.1086/172359.

S. E. Woosley. "Pulsational Pair-instability Supernovae". *ApJ*, 836(2):244, Feb. 2017. doi:10.3847/1538-4357/836/2/244.

S. E. Woosley and A. Heger. "The Progenitor Stars of Gamma-Ray Bursts". *ApJ*, 637 (2):914–921, Feb. 2006. doi:10.1086/498500.

S. E. Woosley and A. Heger. "Long Gamma-Ray Transients from Collapsars". *ApJ*, 752 (1):32, June 2012. doi:10.1088/0004-637X/752/1/32.

S. E. Woosley and A. Heger. "The Pair-instability Mass Gap for Black Holes". *ApJL*, 912(2):L31, May 2021. doi:10.3847/2041-8213/abf2c4.

S. E. Woosley, N. Langer, and T. A. Weaver. "The Presupernova Evolution and Explosion of Helium Stars That Experience Mass Loss". *ApJ*, 448:315, July 1995. doi:10.1086/175963.

S. E. Woosley, A. Heger, and T. A. Weaver. "The evolution and explosion of massive stars". *Reviews of Modern Physics*, 74(4):1015–1071, Nov. 2002. doi:10.1103/RevModPhys.74.1015.

S. E. Woosley, S. Blinnikov, and A. Heger. "Pulsational pair instability as an explanation for the most luminous supernovae". *Nature*, 450(7168):390–392, Nov. 2007. doi:10.1038/nature06333.

A. P. Yadav, S. H. Kühnrich Biavatti, and W. Glatzel. "Strange mode instabilities and mass loss in evolved massive primordial stars". *MNRAS*, 475(4):4881–4890, Apr. 2018. doi:10.1093/mnras/sty092.

S. C. Yoon, N. Langer, and C. Norman. "Single star progenitors of long gamma-ray bursts. I. Model grids and redshift dependent GRB rate". *A&A*, 460(1):199–208, Dec. 2006. doi:10.1051/0004-6361:20065912.

S. C. Yoon, A. Dierks, and N. Langer. "Evolution of massive Population III stars with rotation and magnetic fields". *A&A*, 542:A113, June 2012. doi:10.1051/0004-6361/201117769.

S.-C. Yoon, J. Kang, and A. Kozyreva. "Can Very Massive Population III Stars Produce a Super-Collapsar?". *ApJ*, 802(1):16, Mar. 2015. doi:10.1088/0004-637X/802/1/16.

T. Yoshida, H. Umeda, K. Maeda, and T. Ishii. "Mass ejection by pulsational pair instability in very massive stars and implications for luminous supernovae". *MNRAS*, 457(1):351–361, Mar. 2016. doi:10.1093/mnras/stv3002.

N. Yusof, R. Hirschi, G. Meynet, P. A. Crowther, S. Ekström, U. Frischknecht, C. Georgy, H. Abu Kassim, and O. Schnurr. "Evolution and fate of very massive stars". *MNRAS*, 433(2):1114–1132, Aug. 2013. doi:10.1093/mnras/stt794.

E. Zackrisson, C.-E. Rydberg, D. Schaerer, G. Östlin, and M. Tuli. "The Spectral Evolution of the First Galaxies. I. James Webb Space Telescope Detection Limits and Color Criteria for Population III Galaxies". *ApJ*, 740(1):13, Oct. 2011. doi:10.1088/0004-637X/740/1/13.

J. P. Zahn. "Circulation and turbulence in rotating stars.". *A&A*, 265:115–132, Nov. 1992.

Y. B. Zel'dovich, S. I. Blinnikov, and N. I. Shakura. *Physical principles of structure and evolution of stars.* Moskva: MGU, 1981.

W. Zhang, S. E. Woosley, and A. Heger. "The Propagation and Eruption of Relativistic Jets from the Stellar Progenitors of Gamma-Ray Bursts". *ApJ*, 608(1):365–377, June 2004. doi:10.1086/386300.

S. Zhevakin. *Astron. Zhurnal*, 31:141, 1954.